UNIVERSIDAD CARLOS III DE MADRID

Departamento de Teoría de la Señal y Comunicaciones

DOCTORAL THESIS

ROTOR DETECTION IN ATRIAL FIBRILLATION

Author: GONZALO RICARDO RÍOS MUÑOZ

Supervised by: ANTONIO ARTÉS RODRÍGUEZ

ÁNGEL ARENAL MAÍZ

MULTIMEDIA AND COMMUNICATION

INTERUNIVERSITY PHD PROGRAM

Leganés, June 2018

Tesis Doctoral:	ROTOR DETECTION IN ATRIAL FIBRILLATION
Autor:	Gonzalo Ricardo Ríos Muñoz
Directores:	D. Antonio Artés Rodríguez D. Ángel Arenal Maíz
Fecha:	

Tribunal

Presidente:

Vocal:

Secretario:

Abstract

Atrial fibrillation (AF) is one of the most common arrhythmias in the clinical practice. Catheter ablation method was developed more than 20 years ago as an approach to terminate this rhythm disorder. Since its outbreak, this technique obtained international acceptance among the clinicians, and technological advances in this field increased its safety while reducing the procedure duration. However, there is no perfect AF treatment procedure described yet, since the understanding of the driving and sustaining AF mechanisms remains poor, with pulmonary vein isolation being the most common ablation strategy.

Several theories try to explain the initiating and maintenance mechanisms of the AF, ranging from multiple wavelets propagating at random in the atria to ectopic focus fired from the pulmonary veins. Alternatively, spatiotemporal stable sources (rotors) have been proposed as the maintenance mechanism of AF. The most representative characteristic of a rotor is the re-entry spiral-like propagation pattern that the electrical wavefront exhibits as it propagates. The assessment of its presence and posterior ablation of the sites where rotors anchor might improve the success of AF ablation.

Technical solutions emerged focusing on the rotor assessment problem. They base their methods on the reconstruction of the atrial activity using multi-electrode catheters and phase maps, in which they detect singularity points, the sites where rotors spin. The ablation of these sites showed promising results, but the difficulty to reproduce the results by other authors increased the controversy on this technique. In this Thesis we address the rotor detection problem in the time domain as opposed to current methods based on the phase domain of the signals.

We develop a new method to identify local activation times (LATs) in unipolar electrograms (EGMs) recorded with multi-electrode catheters. We propose a new filtering scheme to enhance the activation component of the EGM while considerably reducing the presence of noise in the signal. This signal processing method reflects the real activity of the tissue in contact with the electrode. It opposes the

Hilbert transform (HT) used to extract the phase component of the signal, that do not correlate well with the temporal activations. With the EGM LATs we perform a spatial interpolation translating the electrode positions of the catheter into a regular 2D grid. This way we generate isochronal maps revealing the electrical wavefronts in the atrium. What is more, this step guarantees compatibility with multi-electrode catheters, not restricting the method to specific models. With the isochronal maps, we develop a new rotor detection algorithm based on the optical flow of the wavefront dynamics, and a rotation pattern match. Additionally, we develop a new method based on Granger's causality to estimate the directionality of the wavefronts, that provides an additional indicator for rotational patterns. We validate the methods using *in silico* and real AF signals.

We implement these methods into a system that can assess the presence of rotational activation sites in the atrium. Our system is able to operate in real-time with multi-electrode catheters of different topologies in contact with the atrial wall. We integrate signal acquisition and processing in our system, allowing direct acquisition of the signals without requiring signal exportation from a recording device, which delays the clinical procedure. We address the computational time handicap by designing parallelizable signal processing steps. We employ multi-core processors and GPU based code to distribute the computations and minimize the processing times, achieving near real-time results.

The results presented in this Thesis provide a new technical solution to detect the presence of rotational activity (rotors) in AF patients in real-time. Although the presence of rotational activity is itself controversial, we individually validate each of the steps of the procedure and obtain evidence of the presence of rotational activity in AF patients. The system has been also found useful to characterize the atrial sites where rotational activity was found in terms of spatial and voltage distribution. The results of this Thesis provide a new alternative to existing methods based on phase analysis and open a new research line in the detection of the mechanisms sustaining AF.

Resumen

La fibrilación auricular (FA) es una de las arritmias más comunes en la práctica clínica. Para tratar de terminar esta fibrilación en pacientes se desarrolló el método de ablación con catéter hace ya más de 20 años. Desde su puesta en marchar esta técnica ha ido ganando aceptación internacional por parte de la comunidad médica, y los avances tecnológicos desarrollados en esta línea han aumentado la seguridad y disminuido la duración del procedimiento. Sin embargo todavía no existe un tratamiento perfecto para tratar la FA, debido en parte a que el conocimiento de los mecanismos que inician y sostienen la fibrilación son limitados. Como método de ablación el aislamiento de las venas pulmonares prevalece como el más empleado en la práctica, pero se hace necesario el desarrollo de nuevos métodos para hacer frente al problema de la FA.

Distintas teorías tratan de explicar los mecanismos de inicio y mantenimiento de la FA, desde unas basadas en la propagación de multiples frentes de onda aleatorios en las aurículas, hasta las que basan su hipótesis en focos ectópicos disparados principalmente desde las venas pulmonares, entre otras teorías. Recientemente, una de estas teorías basada en fuentes espacio-temporalmente estables (rotores) se propuso como mecanismo de mantenimiento de la FA. La característica más representativa de un rotor es su patrón de reentrada en forma de espiral que realiza el frente de onda eléctrico en el tejido auricular. La evaluación de la presencia de rotores y la posterior de los sitios en los que se encuentren puede mejorar el éxito de la ablación en pacientes con FA.

En vista de esta tendencia por la búsqueda de rotores se desarrollaron soluciones técnicas para la evaluación de zonas que alberguen actividad rotacional. Sus técnicas se basan en la reconstrucción de la actividad auricular empleando catéteres multi-electrodo y detectando puntos de singularidad en mapas de phase, esto es la posición en la aurícula en la que el rotor gira. La ablación de estos puntos mostró resultados prometedores, pero la dificultad por replicar los resultados por parte de otros autores incrementó la controversia con respecto a esta técnica.

En esta Tesis abordamos el problema de la detección de rotores en el dominio del tiempo, oponiéndonos a las técnicas actuales basadas en el dominio de la fase de las señales.

Para ello hemos desarrollado un nuevo para identificar tiempos de activación local en electrogramas unipolares registrados con catéteres multi-electrodo. Para ello proponemos un nuevo método de filtrado para realzar la activación del electrograma reduciendo considerablemente la presencia de ruido en la señal. Con este procesado de la señal extraemos y reflejamos la actividad real del tejido en contacto con el electrodo. Al mismo tiempo nos oponemos a la transformada de Hilbert empleada para calcular la componente de fase de la señal, que es sabido no tiene una buena correlación con las activaciones temporales. Con los electrogramas y los tiempos de activación locales aplicamos una interpolación espacial logrando trasladar la posición de los electrodos en el catéter a una rejilla regular en 2D. Mediante este paso generamos mapas isócronos que reconstruyen los frentes de onda eléctricos que se propagan en la aurícula. Además la interpolación nos permite garantizar una compatibilidad con otros catéteres multi-electrodos, no restringiendo el uso de nuestro método a modelos específicos. Con los mapas isócronos hemos desarrollado un nuevo algoritmo de detección de rotores basado en el flujo óptico de la dinámica del frente de onda que hacemos coincidir con un patrón de rotación. Adicionalmente hemos desarrollado un nuevo método basad en la causalidad propuesta por Granger para estimar la dirección de los frentes de propagación, que sirve como indicador adicional para encontrar patrones de activación rotacional. Hemos validado todos y cada uno de los métodos empleando señales *in silico* así como señales reales de pacientes con FA.

En la parte de aplicación, hemos implementado los métodos en un sistema que evalúa la presencia de actividad rotacional en la aurícula. Nuestro sistema opera en tiempo real siendo compatible con catéteres multi-electrodo de diferentes topologías asegurando contacto con la pared auricular. Para evitar sobreextender el procedimiento clínico, hemos integrado las partes de adquisición y procesado de señal conjuntamente, lo que nos permite un registro de las señales directo sin

necesidad de requerir un exportado adicional desde un sistema de registro. Para hacer frente al objetivo de presentar los resultados en tiempo real hemos diseñado todos los pasos de procesado de señal para que sean paralelizables. Para ello empleamos procesadores multinúcleo y código para ejecutar en tarjetas grágicas (GPUs) para distribuir las computaciones y minimizar el tiempo de procesado, logrando resultados en quasi tiempo real. Hemos empleado el sistema de detección de rotores para estudiar la distribución espacial y de voltaje de los sitios que muestran actividad rotacional en la aurícula. Aunque la presencia de actividad rotacional es en sí misma controvertida, hemos validad individualmente todos y cada uno de los pasos descritos obteniendo evidencia de la presencia de actividad rotacional en pacientes con FA.

Contents

List of Acronyms

ADC	analog to digital converter
AF	Atrial fibrillation
AP	action potential
APD	action potential duration
AR	autoregressive
ARMA	autoregressive moving average
AV	atrioventricular
bpm	beats per minute
CFAE	complex fractionated atrial electrogram
CPU	central processing unit
CT	computed tomography
DAQ	data acquisition
DF	dominant frequency
DWT	discrete wavelet transformation
EAM	electroanatomical mapping
ECG	electrocardiogram
EGM	electrogram
EMD	empirical model decomposition

EP	electrophysiology
FFT	fast Fourier transform
FH-N	FitzHugh-Nagumo
FIR	finite impulse response
FIRM	Focal Input and Rotor Modulation
GC	Granger's causality
GPU	graphical processing unit
HGUGM	Hospital General Universitario Gregorio Marañón
HT	Hilbert transform
ICA	independent component analysis
LAT	local activation time
LV	Left ventricle
MF	median filter
MRI	magnetic resonance imaging
PCA	principal component analysis
pEGM	pseudo-electrogram
PS	phase singularity
PVI	pulmonary vein isolation
RAP	repetitive activation pattern
RF	radio frequency
rRMSE	relative root mean square error

SNR	signal to noise ratio
SR	sinus rhythm
WCT	Wilson central terminal

1 Introduction

1.1 Relationship with Published Work

This thesis is based on and therefore partially coincides with the following published contributions:

- Chapters 3 and 4: Gonzalo R. Ríos-Muñoz, Ángel Arenal, and Antonio Artés-Rodríguez. Real-Time Rotational Activity Detection in Atrial Fibrillation. *Front. Physiol.*, 9:208, mar 2018. [102].
- Chapter 5: David Luengo, Gonzalo Ricardo Rios Munoz, Victor Elvira, Carlos Sanchez, and Antonio Artes-Rodriguez. Hierarchical Algorithms for Causality Retrieval in Atrial Fibrillation Intracavitary Electrograms. *IEEE J. Biomed. Heal. Informatics*, pages 1–1, 2018. [75].

The thesis is also related to conference publications [114, 104, 105, 113, 28, 74,

73]. We also issued a patent application as a result of the work developed in the thesis concerning the rotational activity detection system [103]. Additionally, the ongoing work derived from the thesis is expected to give continuity to this research line [33, 32, 99, 100, 101].

1.2 Problem Statement and Motivation

AF is one of the most frequently sustained arrhythmias in clinical practice [63]. Common AF symptoms are weakness, breath shortness, dizziness, heart palpitations or fatigue, although some patients may not experiment any symptoms at all making AF difficult to diagnose in these cases. While in itself AF is not fatal, it can result into serious life threatening complications in the long run, with AF being associated to increased morbidity and mortality [131].

In a healthy heart, the heart chambers contract sequentially in a synchronized order. First the upper chambers of the heart (the atria) receive blood from the body and contract, pumping blood into the lower chambers (the ventricles). After the atria contract, the ventricles expel the blood to the rest of the body by similar muscular contraction. This synchronized pumping mechanism is the normal activity of the heart, and its regular rhythm is called the sinus rhythm (SR). However in an AF episode this rhythm is disturbed, with the atria being irregularly and rapidly activated. This prevents the atria from fully contract, producing an irregular contraction of the ventricles, because the atrioventricular (AV) node connecting the chambers is still operative. Figure 1.1 exemplifies the difference between SR and AF in signals recording the heart activations in an electrocardiogram (ECG). The regular rhythm is disrupted, and its rate becomes irregular and often rapid.

The inability to effectively contract decreases the blood flow to the ventricles and increases the formation of a blood clot, and therefore the risk for stroke. A stroke is the major AF complication and occurs when there is a significant reduction or blockage of the blood flow delivered to the brain, causing permanent damage, severe disability or even death. Stroke is mostly caused by a blood clot, a clump of of blood that clusters changing into a semi-solid or gel-like state that

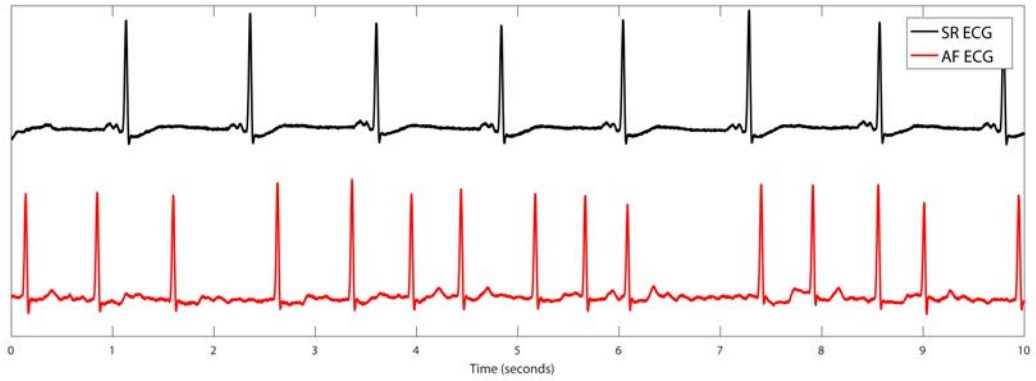

Figure 1.1: Examples of ECG recordings showing different rhythms. Top. Regular SR. Bottom. Irregular AF

can partially or totally block the delivery of blood to the body.

The underlying mechanisms initiating and sustaining AF are still under debate. During the past decades several theories on the initiation and maintenance mechanisms driving AF have been proposed: focal theory, multiple wavelet theory [50], reentries [38, 68], or even transmural endo-epicardial conduction [37]. This situation prevents electrophysiologists to cure the arrhythmia with surgical procedures and/or antiarrhythmic drugs, limiting the outcome of the treatments. All these theories and experimental findings are reviewed in Section 1.5.

1.3 Electrical Activity of the Heart

1.3.1 Heart Physiology

The heart is an organ allocated in the thoracic cage between the lungs, and it is mainly composed of muscular tissue (myocardium). The myocardium inner lining is called endocardium, and covers the heart chambers. The outer lining is the epicardium, and the pericardium, an external fibroserous sac, lines the whole heart. The later is filled with liquid to protect the whole heart from shocks and external threats. The heart is in charge of delivering blood to the rest of the body, and its structure can be equivalently seen as two parallel blood pumps, see Figure 1.2. Each pump (left and right) receive the blood in the atrium (upper

chamber), pushes it to the ventricle (lower chamber) and then expels it to the lungs and the rest of the body.

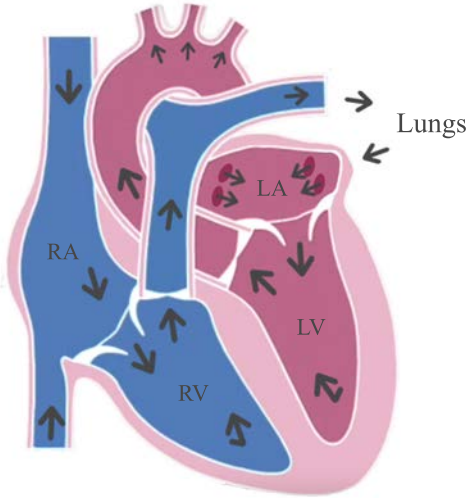

Figure 1.2: Anatomy of the heart chambers representing the right atrium (RA), left atrium (LA), right ventricle (RV), and left ventricle (LV). Pulmonary veins are also included as darker circles inside the left atrium. The blood flow of the heart is represented with arrows.

The normal flow starts by receiving non-oxygenated blood at the right atrium. The blood goes to the right ventricle through the tricuspid valve, and then it travels to the lungs, where the blood is oxygenated. After that, the oxygenated blood enters the left atrium, goes through the mitral valve into the left ventricle, and it is expelled to the rest of the body.

The periodic mechanical movements of the heart define the cardiac cycle. The diastole happens when the chamber is being filled with blood, and the systole refers to the blood ejection caused by the fast contraction of the cardiac muscle. During the filling event (diastole), the chambers are at their resting state, i.e., relaxed, allowing the blood to enter. The blood ejection (systole) pumps the blood out to the lungs and the body when the ventricles contract. The normal contraction-ejection flow can be simplified to: atria filling, atria contraction, ventricle filling, and ventricle contraction.

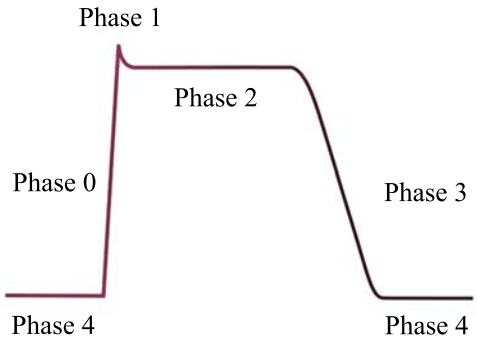

Figure 1.3: The cell cycle showing the different phases of the cardiac action potential (AP).

1.3.2 Cardiac Action Potential

The mechanical contraction of the heart is possible thanks to the ionic fluxes channels located in the cardiac cell membranes. The variation of the membrane electric potential enables the activation of the myocardial cells. The cells trigger an activation which propagates to the surrounding neighboring cells, and thus the electrical impulse advances through the whole heart causing the mechanical contraction. The different electrical stages of the cell, the AP, define the cell cycle, see Figure 1.3, and it is composed of:

- **Phase 0 :** When the cell is at rest, the influx of sodium ions increases the potential of the membrane. When the voltage value exceeds a threshold a rapid depolarization occurs, reflected in the AP as a sharp upstroke.
- **Phase 1:** The sodium channels start to close and the outward potassium channels create an early repolarization that tries to bring the cell to its resting state.
- **Phase 2:** The repolarization is slowed down by the flux of calcium ions, which compensates the outward potassium channels at Phase 1. Phase 2 also receives the name of Plateu phase.
- **Phase 3:** The final rapid repolarization returns the membrane potential to its resting state.

- **Phase 4:** At this stage the cell is at its resting level, with a membrane potential of $[-70, -80]$ mV.

After a refractory period the cell is available to be depolarized once again. This refractory characteristic prevents the cells to be depolarized too soon, which would interrupt the proper functioning of the heart. During the refractory period the cell is able to recover from the previous activation and gets ready for the next depolarization to occur.

1.3.3 Electrical Cardiac Propagation

The whole cardiac activity is ruled by electrical impulses generated by the natural peace makers of the heart. The electrical stimulus starts at the sinus node and propagates through the myocardium cardiac tissue, following a bundle network which carries the activation signal, see Figure 1.4. In a healthy individual the sinus node induces a normal heart rhythm, or SR, of $60 - 100$ beats per minute (bpm). As it propagates, the electrical impulse (signal) causes the contraction of the atrial chambers, delivering blood to the ventricles. The signal is delayed at the AV node, so there is enough time for the ventricles to be filled.

Once the electrical impulse leaves the AV node, the His bundle conducts the stimulus to the Purkinje fibers (fast conductive fibers), which manage a coordinated contraction of the ventricles, resulting in the ejection of blood out of the heart, and the end of the cardiac cycle.

1.4 Signals in Electrophysiology

Clinicians have access to a variety of tools to assist them in the diagnosis of cardiac arrhythmias based on the electrical activations of the heart. They perform electrical activity measurements to observe non-periodic rhythms, abnormal electrical conduction, or even to evaluate infarction and fibrosis scenarios. In this section we present the most common signals used for studying arrhythmias.

The measurement system used to register the heart activity varies with the

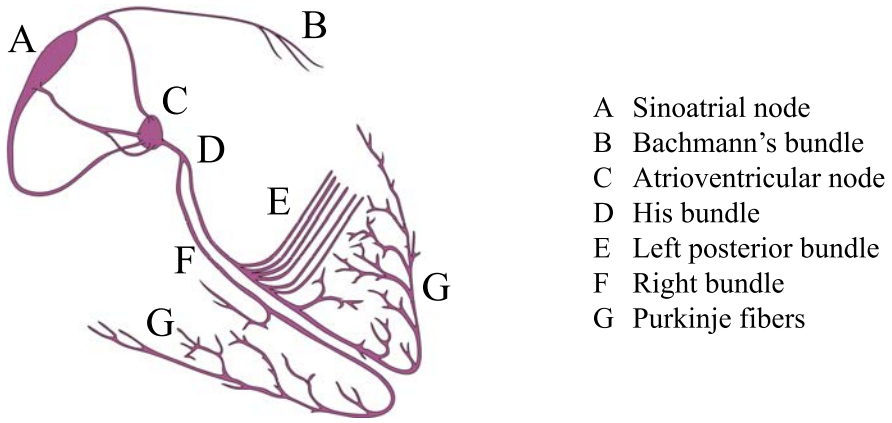

Figure 1.4: Electrical conduction system of the heart. Nodes and bundles propagate the electrical impulse across the heart to perform the contraction that delivers blood to the rest of the body.

observation scale. For instance, as a first diagnosis approach, the electrophysiologist may require to analyze the signals acquired with surface skin-electrodes, while a thorough study would involve the use of invasive catheters to record local intracardiac activity at specific regions of the heart.

1.4.1 Electrocardiograms

The ECG is the main diagnosis tool used in clinical practice. It records the electric cardiac activity with external electrodes placed on the skin of the patient. The electrodes register the electrical field generated by the heart as the electrical impulse propagates across the myocardium. The propagation of the electrical wavefronts through the surrounding tissue allows the electrical current to be measured with these electrodes, obtaining the ECG signals.

The resulting ECG signal exhibits differentiated morphology shapes. In Figure 1.5 we include the most characteristic representation of the ECG, comprising: the P wave, QRS complex and the T wave. This morphology segmentation corresponds to the path that the electrical impulse follows throughout the heart (top to bottom). The depolarization of both atria produces the P wave, and once it reaches the ventricles their depolarization generates the QRS complex. After the

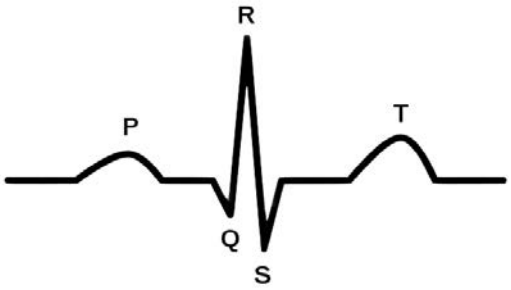

Figure 1.5: *I-lead* ECG wave.

ventricular depolarization, the T wave is the result of the repolarization of the ventricles. The return to the resting state allows the chambers to be filled with blood once again (diastole). It is important to bring attention to the absence of atrial repolarization contribution to the ECG. The reason is that the larger size of the ventricles makes the depolarization QRS complex to occlude the coexisting atrial repolarization, which is smaller in amplitude.

The most common employed electrode layout for ECG recording is the 12-lead ECG. The body surface electrodes are placed on the skin according to the positions displayed in Figure 1.6. The differential (bipolar) voltage of the electrodes results in a total of 12 ECG signals revealing the cardiac activity. These signals are filtered to enhance the ECGs and to remove any noisy contributions that may distortion or interfere with the signals. Finally, the 12 ECG signals can be displayed so the physicians can analyze them. In Figure 1.7 we show an illustrative example of the 12-lead ECG signals for the specific case of an AF patient.

1.4.2 Intracardiac Electrograms

One more useful diagnosis tool is the intracardiac EGM. In EGMs signals the recording electrode is in direct contact with the cardiac tissue. EGMs provide information concerning the local tissue surrounding the electrode. They record the ionic activity beneath the electrode, transforming the ionic activity of the cardiac cells into electrical currents that can be converted into readable voltage signals by electronic devices.

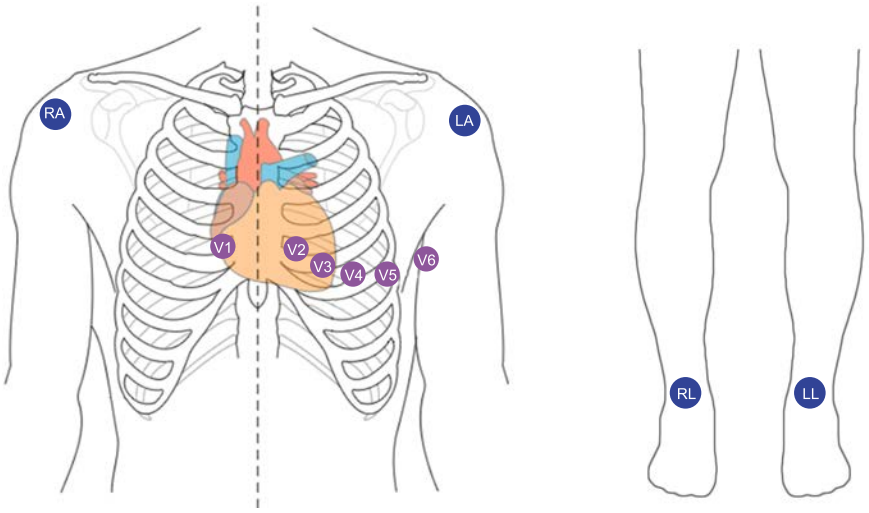

Figure 1.6: Electrode placement illustration for the 12-lead ECG visualization.

The recording electrodes are normally embedded in a catheter that is advanced intravenously into the heart chambers (atria or ventricles), veins or arteries. There is a wide variety of catheters in clinical practice, with different number of electrodes, geometry and size, see examples in Figure 1.8. The electrodes register low voltage signals, which require filtering and enhancement by electronic equipment, generally performed by an operational amplifier. These devices provide differential voltage measurements, i.e., the difference between one electrode (positive) and a reference signal (negative). In general when using an operational amplifier, the positive and the negative electrode are referred as anode and cathode respectively.

Besides intracardiac multi-electrode catheters other techniques like the voltage clamp can be employed to read the intracellular action potential of the cell membrane of a single cell, and also epicardial patches can be placed on the heart to read epicardial potentials. For simplicity and due to the scope of this thesis, we just mention these techniques to register EGM signals and we focus the attention on multi-electrode catheter acquisition.

Essentially, unipolar and bipolar configurations are used when using multi-electrode catheters. In Figure 1.9 and Figure 1.10 we include a representative example of the signals visualized during an ablation procedure using bipolar and unipolar configurations respectively. Unipolar EGMs are obtained using an elec-

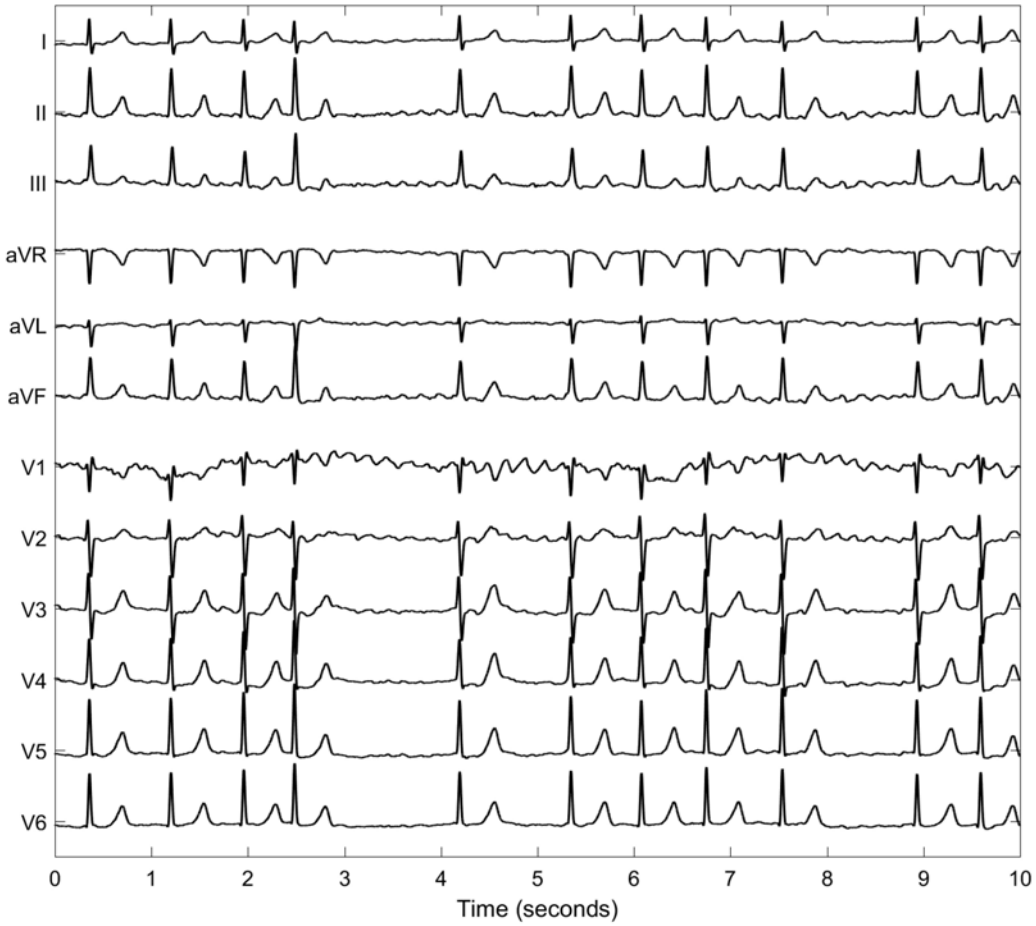

Figure 1.7: Illustration of the 12 lead ECG signals for a patient with AF.

trode in contact with the cardiac tissue as the positive input (anode), and a reference at infinity distance as the negative electrode (cathode). In practice, Wilson central terminal (WCT) is commonly used as the distant reference electrode. Bipolar EGMs involves computing the difference between two electrode signals, reflecting the local activity between the electrodes.

The main characteristics of the EGMs configurations are directionality, temporal resolution and spatial resolution, see Table 1.1.

Directionality is defined as the ability to give information about the direction of the wavefront, see illustration in Figure 1.11. In the bipolar case depending on the electrode orientation with respect to the incoming wavefront, the morphology of the bipolar signal gets modified, reaching the worst case scenario when

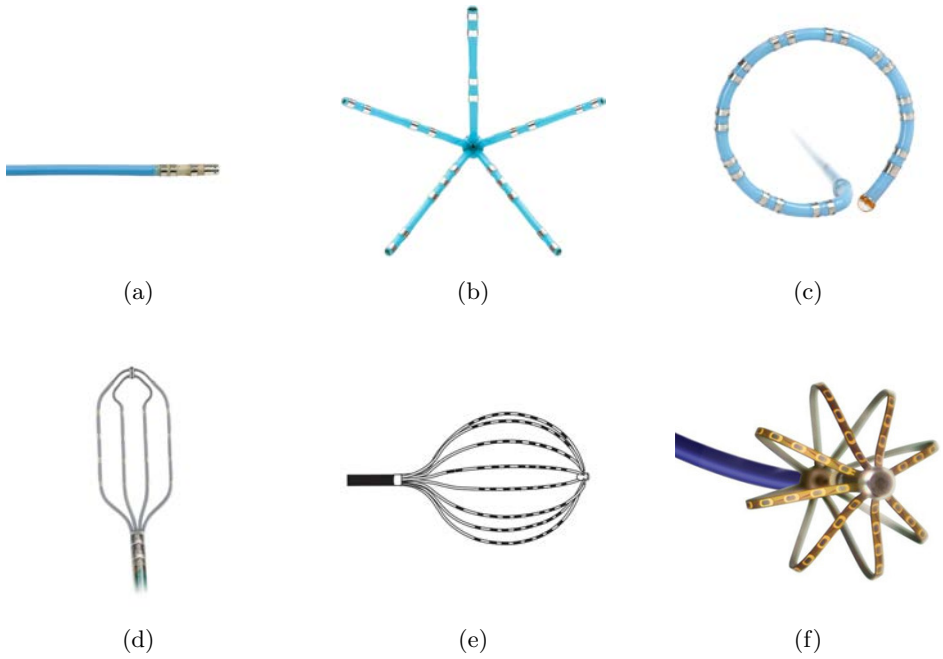

(a) (b) (c)

(d) (e) (f)

Figure 1.8: Intracardiac catheters. (a) Thermocool® (Biosense Webster, Diamond Bar, California, USA)mapping and ablation catheter. (b) PentaRay® (Biosense Webster, Diamond Bar, California, USA)mapping catheter. (c) Lasso® (Biosense Webster, Diamond Bar, California, USA)mapping catheter. (d) Advisor HD™ grid (Abbott, St. Jude Medical, St. Paul, Minnesota, USA)mapping catheter. (e) Constellation™ (Boston Scientific, Natick, MA, USA)mapping catheter. (f) Intellamap Orion™ (Boston Scientific, Natick, MA, USA)mapping catheter.

the propagation direction is perpendicular to the line connecting both electrodes, see Figure 1.11B. In this specific case, the two electrodes record almost identical activity, resulting in a flat bipolar signal containing no information, as seen in Figure 1.11B. The optimal bipolar case is achieved when the wavefront is parallel to the electrodes position, see Figure 1.11A. In this case the electrodes record different signals and the bipolar signal contains a voltage fluctuation between the unipolar activations.

Fortunately unipolar EGMs contain information about the direction of the wavefront regardless of the direction of the wavefront. When the wavefront approaches the electrode a positive deflection is recorded, and as the wavefront moves

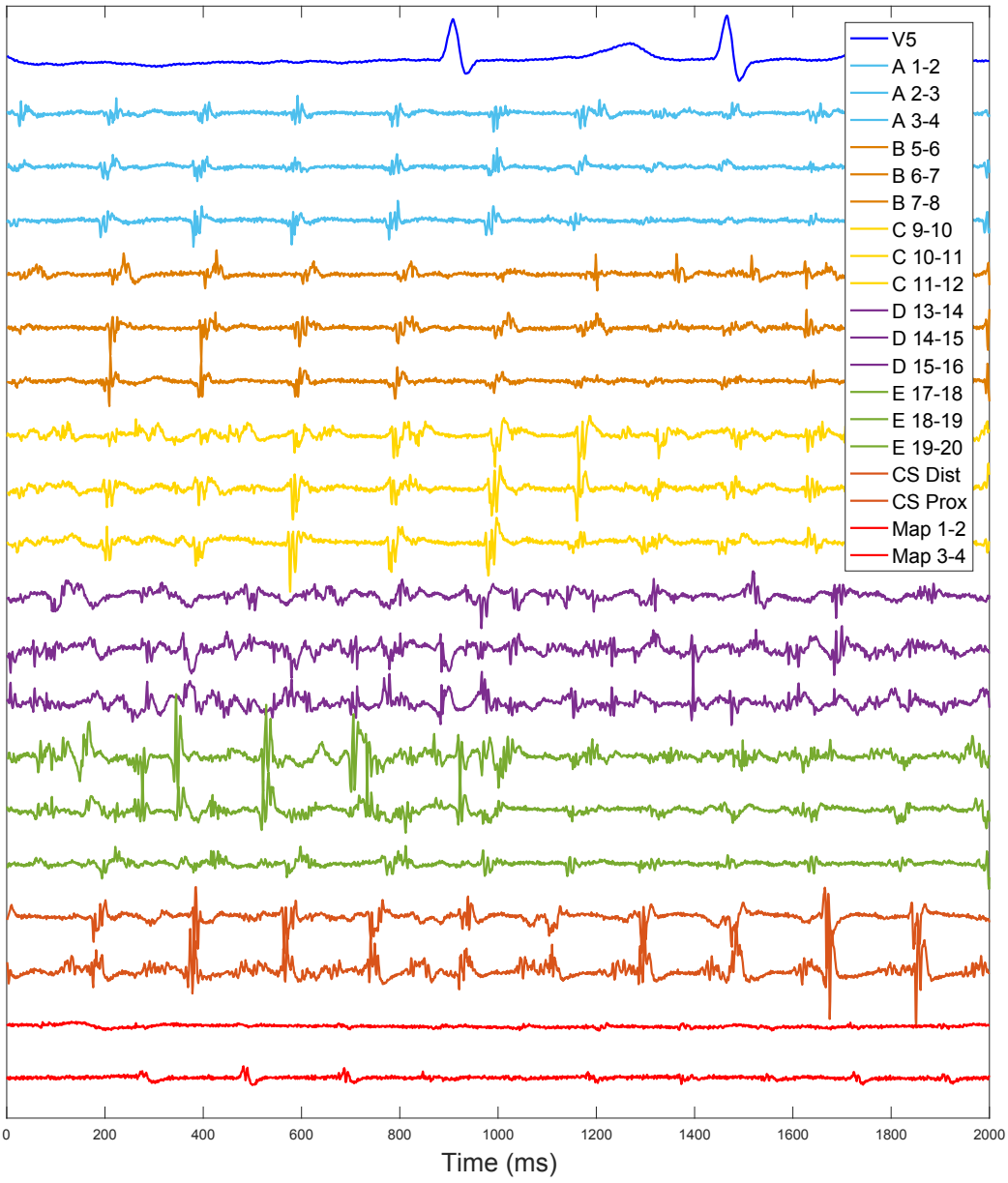

Figure 1.9: Commonly employed ECG and bipolar EGM signals in AF ablation procedures. In the example the bipolar measurements for all the branches (A-E) of a PentaRay®catheter are shown together with two tetrapolar catheters, one placed at the coronary sinus (SC Dist, SC Prox) and the other employed to map and ablate (Map 1-2, 3-4).

away a negative contribution appears, providing information about the directionality of the wavefront. Morphology in this case does not vary with the direction

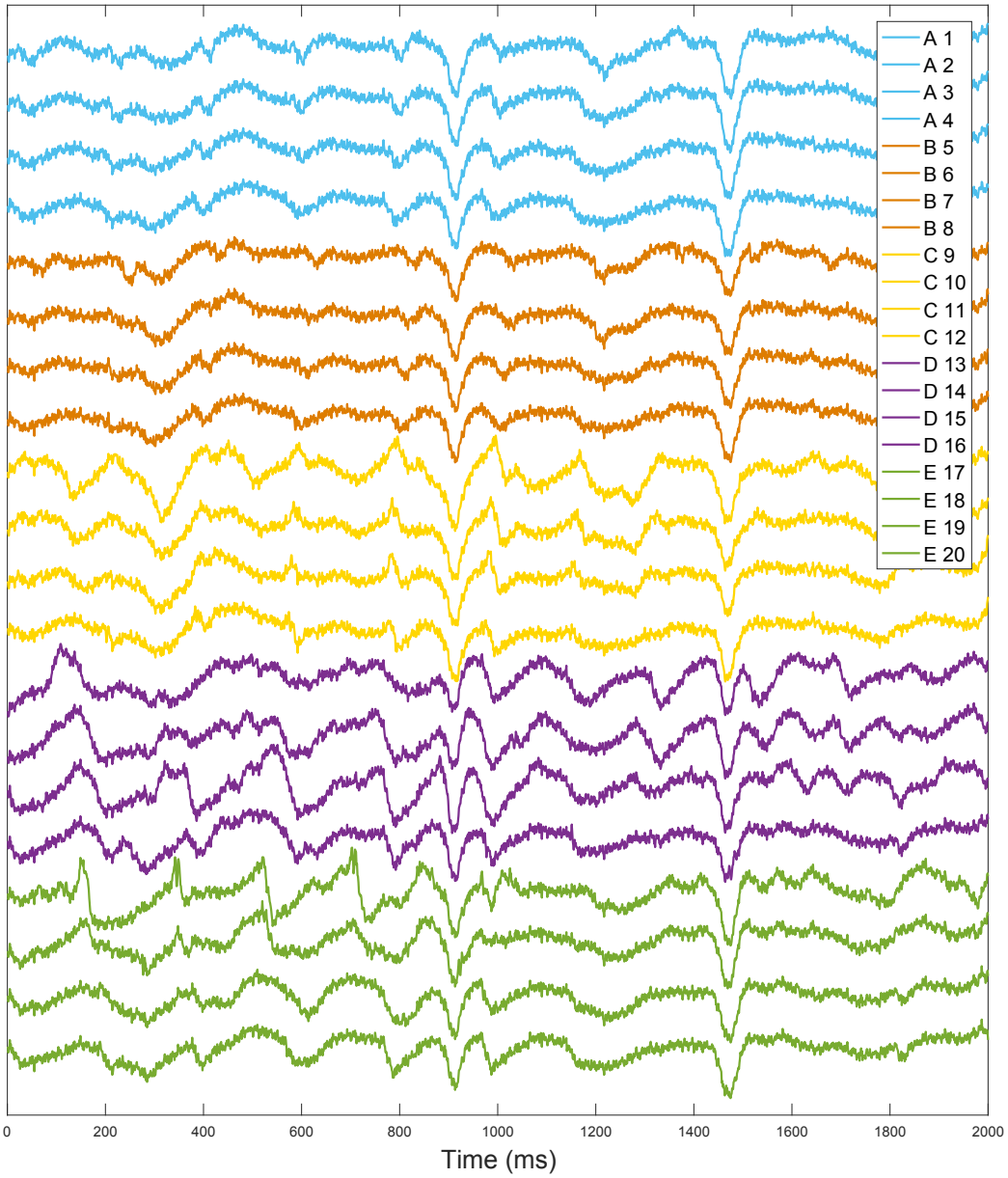

Figure 1.10: Unipolar signals obtained with the electrodes of a PentaRay catheter, with each branch labeled A-E containing 4 electrodes. The signals show the same recording temporal window as the bipolar ones in Figure 1.9

of the activation as it does in the bipolar recording. The only disadvantage is that unipolar EGMs suffer from far-field activity, but this undesired effect can be removed with filtering and cancellation techniques.

Temporal resolution is the ability to recognize the LAT when the wavefront

	Directionality
Unipolar	Can be extracted from morphology.
Bipolar	Wave direction alters the morphology.
	Temporal resolution
Unipolar	Accurate LAT identification.
Bipolar	Not well defined LAT identification.
	Spatial resolution
Unipolar	Good resolution but contains far-field activity.
Bipolar	Resolution depends on electrode distance. No far-field contribution.

Table 1.1: Summaray detailing the different unipolar and bipolar configuration characteristics.

arrives at a certain electrode, see Figure 1.12. In unipolar EGMs this happens when there is a sudden deflection in the signal. The time instant corresponding to the local activation matches the point of maximum negative slope, see signals U1 and U2 in Figure 1.12. Hence the first derivative of the signal $\frac{dV}{dt}$ can be used to identify LATs. However in the bipolar case this local detection becomes a problem, since there is no full agreement on the methods and approaches to identify the LATs. Signal B1-2 in Figure 1.12 exemplifies the irregular shape of the bipolar signal, where the LATs cannot be accurately identified. It is common to use the maximum voltage value of the EGM as the LAT, while other techniques detect the bipolar onset and offset interval to estimate the LAT [39]. Other authors use a library of manually labelled EGM activation times and compare the matching of these LAT templates with the bipolar EGM signals to identify the LAT [125]. Additionally, when facing complex EGMs most of these techniques fail to be robust.

Spatial resolution is the ability to establish the tissue area location which produces the recorded action potential, see Figure 1.13 for an illustrative example on this feature. Unipolar EGMs exhibit the local activity of the area surrounding the distal input (furthest electrode with respect to the operator). Due to being using a distant reference electrode, far-field activity is also recorded. This activity

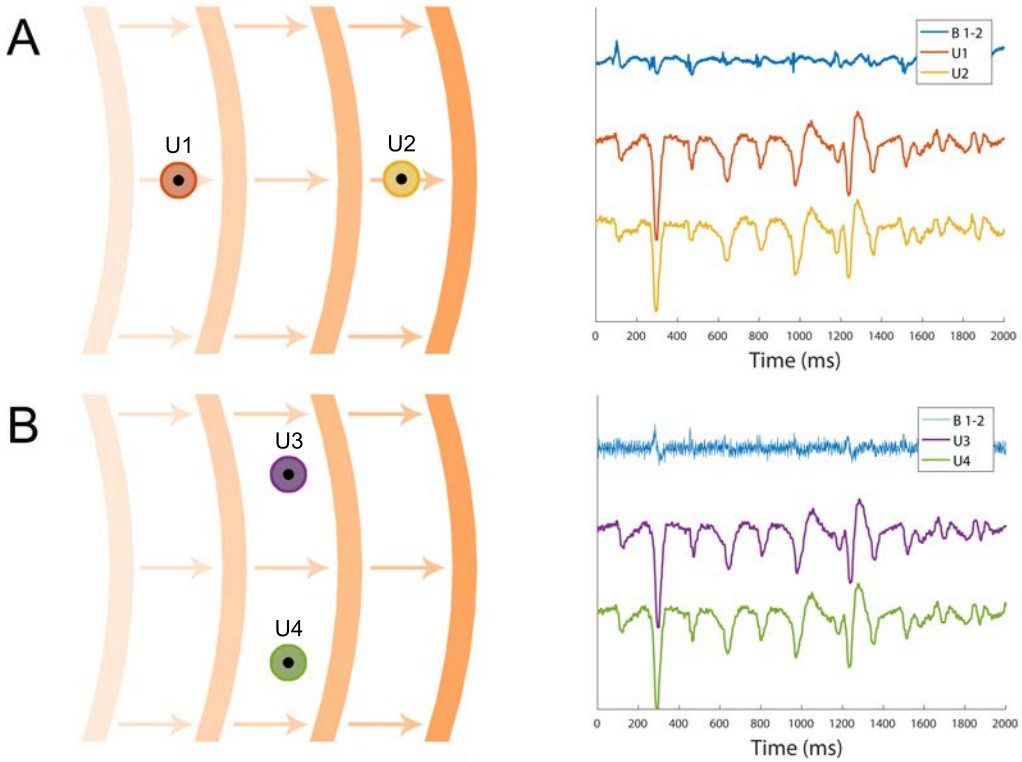

Figure 1.11: Directionality of unipolar and bipolar signals. **A.** Wavefront approaching parallel to the electrodes U1-U2 line, resulting in a bipolar signal with noticeable activations. **B.** Wavefront approaching perpendicular to the electrodes U3-U4 line, both electrodes record almost identical signal resulting in a bipolar signal reflecting poor local activations.

interferes with the EGM of the tissue in contact with the electrode, thus providing a poor signal to noise ratio (SNR). In the bipolar configuration this problem is solved because of the subtraction involved in the differential operation. When the source of the noise is far enough both electrodes record similar additive noise, then when the differential signal is calculated the noisy contributions are canceled out, improving the SNR. Moreover, bipolar EGMs reflect the local activity taking place around and between the electrodes gap, and the smaller this gap is the bigger the spatial resolution. This effect on the distance of the electrodes involved in the differential operation of the bipolar configuration is exemplified in Figure 1.13. In Figure 1.13A the electrodes U1 and U2 are close to each other if compared to the electrode pair U1-U3 in Figure 1.13B. The closer the electrodes are, the higher the

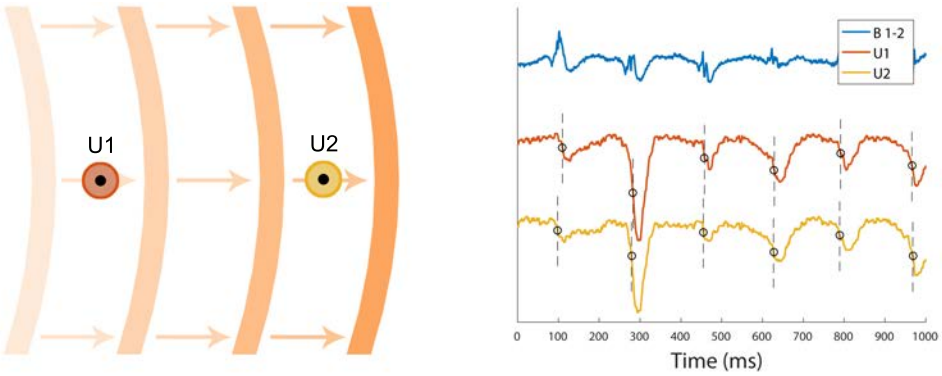

Figure 1.12: Temporal resolution of unipolar and bipolar signals. In the figure the LATs in the unipolar signals U1 and U2 are clearly defined by the time instant of the maximum negative value of $\frac{dV}{dt}$. However for the bipolar signal B1-2 the accurate LAT identification is not so well defined.

spatial resolution is, narrowing the electrical phenomenon happening between the electrodes. As the electrodes separate the shape of the bipolar signal losses spatial resolution, since the activations in the unipolar signals get delayed. In this case it is not so easy to characterize the concrete point in the space producing the signal.

1.4.3 Optical Mapping

The optical mapping systems provide direct imaging of the electrical activity of the heart. These techniques are based on the response provided by fluorescent dyes that are voltage sensitive to the electrical activity. The dye adheres to the cellular membrane of the cells emitting a light whose frequency directly depends on the membrane voltage variation. This way using high spatial and temporal resolution cameras, the cardiac action potential can be recorded at multiple sites simultaneously. With this technique a bidimensional image of the electric activity is obtained.

In the images each pixel represents the average action potential of the region in the field of view of the camera for that specific pixel. With the optical mapping systems the mechanisms of electrical propagation and cell level events can be studied. Optical mapping is usually employed in experimental studies with *in vivo*

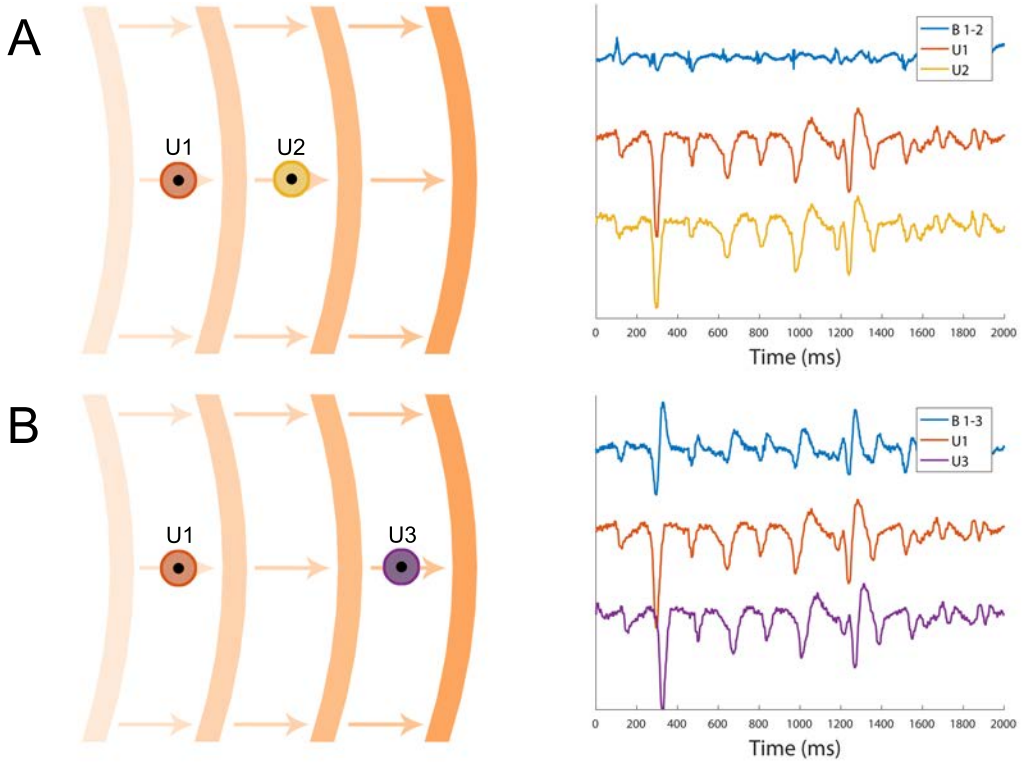

Figure 1.13: Spatial resolution of unipolar and bipolar signals. In the bipolar signals spatial resolution is lost as the distance between the electrodes involved in the differential operation increases. **A.** Electrodes are close and provide good spatial resolution. **B.** Electrodes are further away making the shape of the bipolar signal to be altered losing the ability to accurately define the activity of a local site.

hearts and cultivated monolayer cardiac cells.

1.5 Study of Atrial Fibrillation

1.5.1 Atrial Fibrillation Triggering and Maintenance Mechanisms

The first reference to AF dates back to 1909, when Thomas Lewis conceived experiments to better understand the *"auricular fibrillation"* [69]. His findings suggested reentry as an early theory mechanism behind the AF. Additionally, other studies had also considered the initial idea of random distributed sources in the atrium, *Winterberg 1907* [133], or close circuit propagation in the atria, *Mines 1913* [82],

as possible causes of AF. These were the most trusted hypothesis until 1948, when Scherf conducted a series of experiments to conclude that an ectopic focus such as a rapid stimulus of the atrial tissue could be the cause of AF [116]. One of his most remarkable discoveries was the observation of refractory islands of tissue formed as the impulse advanced into the atrium. These islands of refractory tissue resulted into reentry waves, which he did not considered to be the cause of AF but a concomitant feature accompanying the ectopic focus theory. Nowadays, the ectopic focus hypothesis triggering AF is one of the plausible AF theories due to the new findings and experiments performed in the last decades.

Besides the new findings on AF achieved by that time, this theory was eclipsed by the observations made by Moe [83]. In his experiments Moe confirmed the ideas of refractoriness stated by Scherf, and he concluded that strands or islets of refractory tissue generating reentry waves became fractionated into independent daughter wavelets, which could sub-divide again into more offsprings of the first wave. This was the basis of the multiple wavelet hypothesis, a new alternative to the previous proposed theories. In 1964 Moe proved that random propagation of waves in an non-homogeneous tissue might be the cause of AF using computational models [84]. At this point the AF was considered a self-sustained process. Moe considered that the major mechanism behind AF was due to reentry, but he also realized that the irregular atrial activation might possibly involve other factors like single/multiple fast discharging ectopic focus, or rapidly propagating circus movement.

For decades reentry was the leading theory mechanism for AF, until new technical advances became available. In 1985 using electrode based electrical recording technology, Allessie demonstrated that multiple waves could maintain AF [7]. The wavelet hypothesis stated that a minimum number of simultaneous wavelets would perpetuate AF. At least 4 to 6 wavefronts were necessary to sustain the fibrillatory process, while a smaller number of wavefronts would combine into a single one restoring the SR.

This theory could explain the maintenance mechanism of AF, however it did

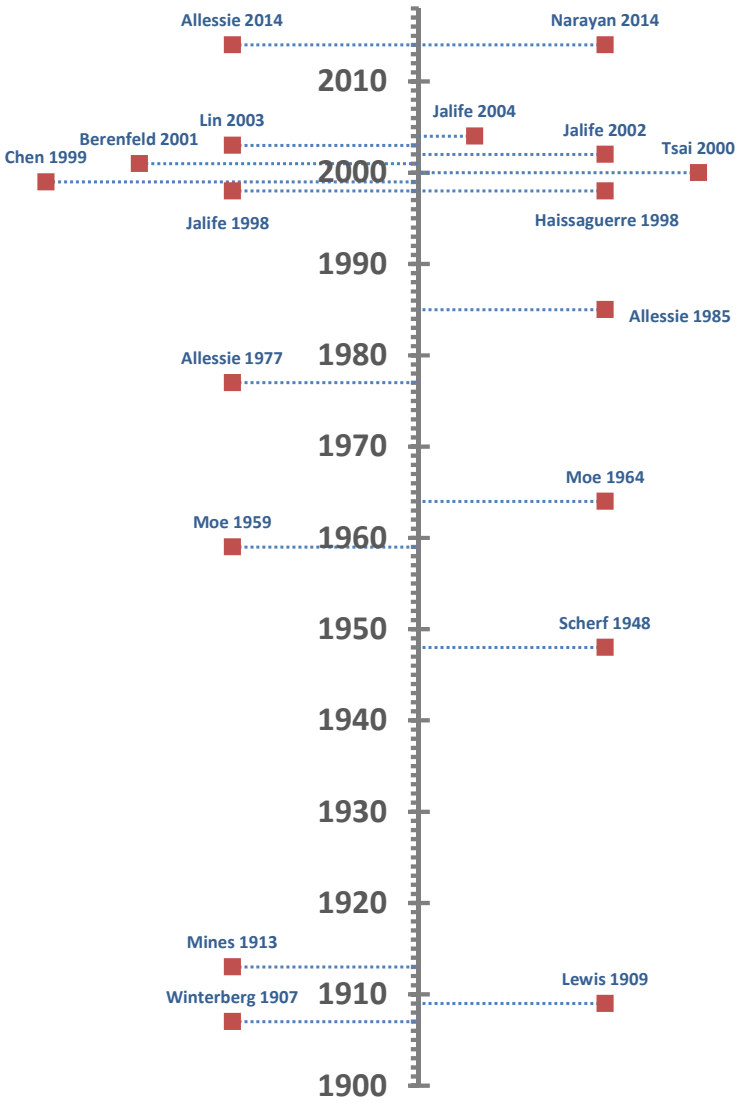

Figure 1.14: AF timeline.

not clarify the initiation of the arrhythmia. In 1998, new observations made by Haissaguerre brought back the attention on ectopic focus firing the AF [50]. He found fast activation foci to be triggering AF and that they were mostly distributed at the pulmonary veins. This region is characterized by the union of atrial and

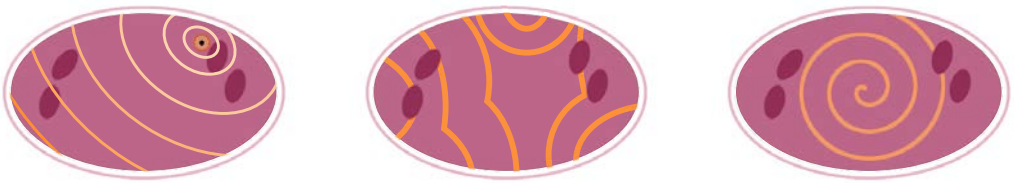

(a) (b) (c)

Figure 1.15: AF theories. **(a)** Focal theory. **(b)** Multiple wave theory. **(c)** Rotor theory.

vein tissue whose heterogeneous interconnection could explain the initiation of the arrhythmia. In the experiments he was able to prove that focal ectopic triggers could fire AF, and also promoted the endocardial catheter ablation as a treatment for AF patients.

At the same time, spatiotemporal stable sources (rotors) were proposed as the maintenance mechanism of AF, *Jalife 1998, 2002, 2004* [55, 57, 56], and *Berenfeld 2001* [18]. The theory of circle reentry had already been introduced by Lewis and then Allessie et al in the 19070s [5], but rotors proposed that the wavefront curvature could intensely bend and became the center of the reentry, with approximated zero conduction velocity at its centermost point. This way rotors are conceived as functional reentry, in opposition to anatomical reentries where the wavefront pivots around regions of non-excitable tissue. The higher activation rate of the rotors with respect to SR allows this kind of wavefronts to activate the surrounding tissue and dominate the activation of the atria over the SR. In *in silico* simulations and preclinical experiments rotors were formed and maintained when a wavefront interacts with obstacles, scars, or heterogeneous tissues with anisotropic conduction. The conduction of velocity and the refractoriness of the tissue became important features as they might be involved in the development and generation of rotors. Unfortunately, in the clinical practice the role of rotors as AF drivers is still controversial, with no confirmation nor acceptance of the rotor paradigm, *Narayan 2014* [86], *Allessie 2014* [8, 4].

After this brief historic introduction, all the theories can be condensed into three main groups:

Focal theory: those supporting the disorganized activity generated after the fractionation of the wavefronts triggered from a focal discharge in the atrium, see Figure 1.15A. With studies supporting pulmonary veins as the most likely regions to be the source of these rapid focal discharges, *Chen 1999* [30], and also contemplating other areas to be responsible for focal discharges, e.g. the coronary sinus, superior vena cava, left posterior wall, or crista terminalis, *Tsai 2000* [126], Lin 2003 [71].

Multiple wave theory: comprising the supporters of multiple wavelets propagating at random in the atrial tissue, see Figure 1.15B. They suggest that a minimum number of simultaneous wavelets would perpetuate AF. Although its maintenance possibly involves some form of reentry circuit caused by wavebreaks [121].

Rotor theory: those in favor of a self-sustained vortex of rotational activity, which can be stable and anchored at a specific region of the atria, or that may drift throughout the tissue, see Figure 1.15C. The rotor can sustain AF becoming the principal driver of the the arrhythmia due to the development of a functional reentry that enables the self-perpetuation of the rotational vortex.

1.5.2 Atrial Fibrillation Classification

As recommended by the European Society of Cardiology, the AF diagnosis requires a documentation of the rhythm with an ECG recording [63]. The signals must show the principal characteristics of the AF: irregular ventricle activations and the unperceptive vanished P-waves. In the event of AF, the P-wave corresponding to the depolarization of the atria is no longer present and it is replaced by fast fibrillatory waves. The fibrillatory period of the AF normally comprises 300 to 600 bpm, i.e., a frequency interval of $5 - 10$ Hz (beats per second). The first channel in Figure 1.7 corresponding to the *I-lead* exemplifies the absence of P-wave. If we compare it to the pattern in Figure 1.5 we can see how the P-wave disappears.

Besides the absence of P-wave in the ECG, AF is also characterized by the irregular activation of the ventricles. This is manifested in the variability of the

interval between R-peak activations in the ECG, see R-peak intervals in Figure 1.7.

As for the classification, AF can traditionally be divided into five types attaining to the duration, spontaneous termination and presentation of the AF episodes, see Table 1.2 [63]. There is no unique classification for AF, and other authors may include different classification criteria depending on the characteristics of the patient, or the suspected causes of the arrhythmia, e.g. focal AF triggered by ectopic activations, Left ventricle (LV) dysfunction, onset of AF after mayor surgery, patients with inherited cardiomyophaties, athletes, or gen carriers associated with AF.

AF pattern	**Definition**
First diagnosed	AF that has not been diagnosed before, irrespective of the duration of the arrhythmia or the presence and severity of AF-related symptoms.
Paroxysmal	Self-terminating, in most cases within 48 hours. Some AF paroxysms may continue for up to 7 days. Cardioverted episodes within 7 days should be considered paroxysmal.
Persistent	AF that lasts longer than 7 days, including episodes that are terminated by cardioversion, either with drugs or by direct current cardioversion, after 7 days or more.
Long-standing persistent	Continuous AF lasting for $\geq$ 1 year when it is decided to adopt a rhythm control strategy.
Permanent	AF that is accepted by the patient (and physician). Hence, rhythm control interventions are, by definition, not pursued in patients with permanent AF. Should a rhythm control strategy be adopted, the arrhythmia would be re-classified as 'long-standing persistent AF'.

Table 1.2: Traditional AF classification (adapted from [63]).

1.5.3 Therapies

The discrepancy on the mechanisms triggering and sustaining AF contributed to the support of different treatments to tackle the termination of this arrhythmia. To this end, the main approaches are surgical and pharmacological therapies, which are normally combined to improve the success. However, the effectiveness of the treatments for AF still remains suboptimal if compared to other common arrhytmias.

Antiarrhythmic drug therapy.

The administration of pharmacological drugs has different purposes, such as the anticoagulation of blood to reduce the generation of clots, the control of the cardiac frequency, the maintenance of the SR, chemical cardioversion, and the prevention of AF episodes from happening. The administration of pharmacological drugs can affect the excitability and conduction velocity of the cardiac tissue, increase the refractory period to prevent reentrant waves to prevail, or even extend the action potential duration (APD). Hence, the prescription of drugs depends on the patient and the ionic mechanisms which are affected by the treatment. Per contra, drug therapy does not only affect the atrial tissue but causes frequent side effects that may even increase the rate of mortality [89, 90].

Electrical cardioversion therapy.

An electric shock is delivered to restore SR, and dates back to 1962 [72]. The electrical discharge interrupts the the whole electric activity of the heart allowing the restitution of the natural heart rhythm. This is a common therapy which is normally employed when the drug therapy presents no success. After cardioversion drug administration is commonly used to prevent the arrhythmia to recur and to reduce blood clot formation.

Ablation therapy.

When drug therapy and electrical cardioversion present no effectiveness to prevent the AF from recurring, catheter based ablation is employed. This treatment delivers radiofrequency energy to the atrial tissue, heating the area in contact with the catheter tip generating a lesion. After the lesion heals it becomes a scar which presents no electrical conduction capability. Ablation can also be performed by cryoablation, an alternative that uses a refrigerant to freeze the tissue creating a lesion that also disables its conductivity properties.

Ablation allows electrophysiologist to remodel the electrical behavior of the heart. Following evidences on ectopic foci triggering AF near the pulmonary veins [50], pulmonary vein isolation (PVI) became one of the most common clinical procedures based on the ablation principle. Since the pulmonary veins are believed to be responsible for ectopic discharges that may initiate and maintain AF, the PVI technique creates a linear lesion around the pulmonary veins to disconnect them from the rest of the atrial tissue. This way if any spontaneous activation initiated at the pulmonary veins tries to propagate it will be block by the linear lesions, preventing it to trigger or sustain the arrhythmia. Additional ablation lines can be also created to isolate other regions related to ectopic activations, e.g. the cava veins or the atrial appendages. The effectiveness of this technique in patients differs depending on the AF development state, with higher success in patients with paroxysmal AF than those with persistent AF [29].

In order to improve the success rate new ablation guided procedures were developed based on different perpetuating mechanisms. One of the first was based on the identification and later ablation of atrial regions exhibiting complex fractionated atrial electrograms (CFAEs). The CFAEs are EGMs which become fractionated due to slow conductivity regions, focal micro-reentries, pivot/anchor points or by the multiple wavefront collission [6]. They were believed to be responsible for AF maintenance, as their existence possibly allowed the harboring of AF drivers. However, clinical studies based on this technique provided no significant success, setting aside this approach at the moment in favor of other methods [96].

Other studies based their approach on the activation frequency of the atrial regions, with higher frequencies assumed to be driving AF. The sequential analysis of the dominant frequency (DF) performed on the registered EGMs generates the frequency gradient of the atria. The DF provides a frequency measurement in hertz (Hz) of the fundamental frequency of the signal. The DF involves signal preprocessing and calculating the maximum peak in the frequency spectrum of the signal. The studies on DF guided ablation showed comparable success to the PVI procedure, but still presented no promising results for persistent AF [12, 13]. Furthermore, there exist different opinions on the stability of the detected pattern activity in time, since normally signals during AF are not perdiodic or present repetitive patterns [58].

Other AF methods based on the identification of focal and rotational drivers were proposed to guide the ablation [85]. By analyzing the EGMs recorded by basket catheters they aim to locate the position of the AF drivers, but their success remains controversy [17].

1.5.4 Electrophysiology Laboratory Equipment

With the emergence of catheter ablation procedures the electrophysiologists just required a fluoroscopy system to guide the catheter into the heart and the position to deliver the radiofrequency energy, plus a recording system to display the EGMs measured by the electrodes in the catheter. See Figure 1.16 for a fluoroscopy image example.

The main disadvantage of the fluoroscopy based ablation is the vast radiation time that is delivered to the patient. With the goal of reducing the radiation exposure new non-fluoroscopy systems were developed. The basis of these systems, also known as electroanatomical mapping (EAM) systems, resides in their capability to spatially locate the catheter without fluoroscopy visual confirmation. This technological advantage reduces the radiation exposure time drastically.

The EAM systems locate the catheter electrodes using magnetic or impedance measurements. They work in a similar way, but depending on the commercial

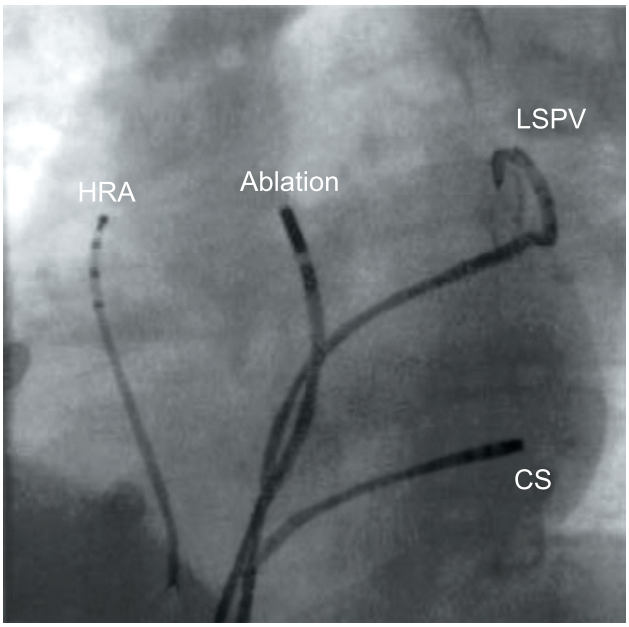

Figure 1.16: Fluoroscopy image example during a clinical procedure. Catheters can be visualized and their position inside the heart chambers can be verified. Figure adapted from [11].

system they measure the magnetic field strength or the impedance variation of the electrodes with respect to reference patches. These patches are placed near the patient or in direct contact with the skin of the patient. With the reference patches the EAM systems can triangulate the position of the electrode. The most known commercial EAM systems are the CARTO® 3 (Biosense Webster, Diamond Bar, California, USA), EnSite™ NavX™ (Abbott, St. Jude Medical, St. Paul, Minnesota, USA), and RHYTHMIA HDx™ (Boston Scientific, Natick, MA, USA). In Figure 1.17 we include screen shots of the different EAM systems during different atrial volume reconstructions.

EAM systems can perform a volume reconstruction of the veins, arteries and heart chambers as the catheter moves. They also display the EGM and provide the information recorded by the electrodes of the catheter. They can relate the information of the acquired signals with their position in the reconstructed volume. This way they generate 3D maps characterizing the cardiac tissue, e.g. unipolar-bipolar voltage, activation times, or impedance values. This information is useful

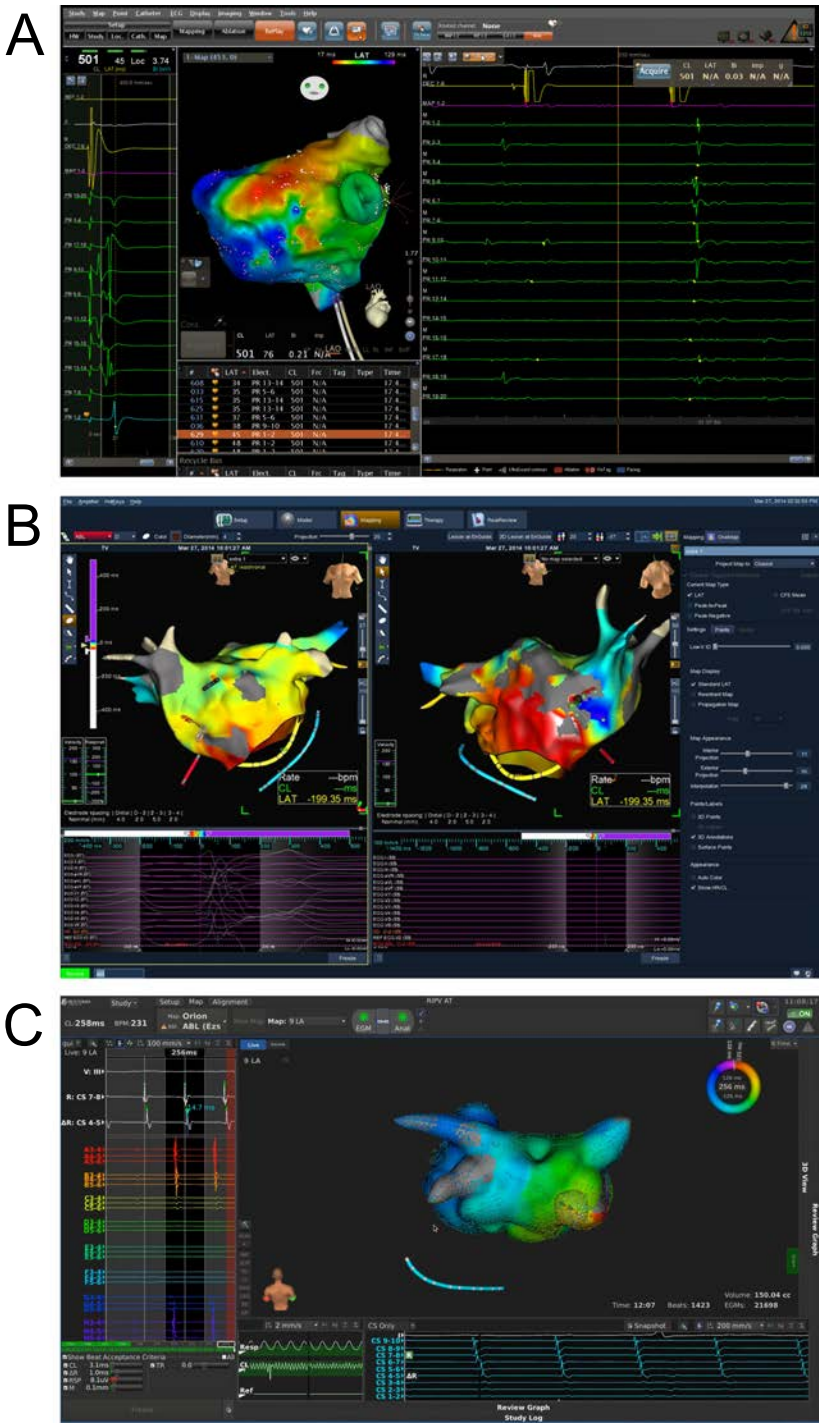

Figure 1.17: Most common EAM systems in the clinical practice. **A.** CARTO® 3 (Biosense Webster, Diamond Bar, California, USA). **B.** EnSite™ NavX™ (Abbott, St. Jude Medical, St. Paul, Minnesota, USA). **C.** RHYTHMIA HDx™ (Boston Scientific, Natick, MA, USA).

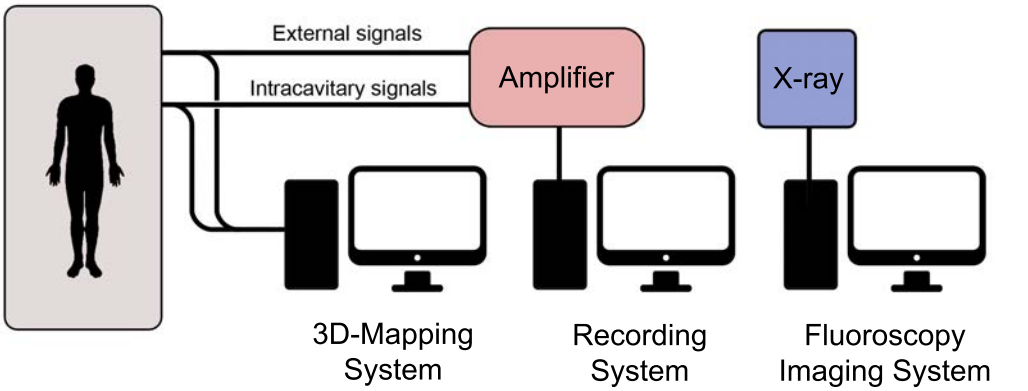

Figure 1.18: Electrophysiology equipments in AF ablation procedures. From left to right, we have a 3D EAM system for anatomic reconstruction and clinical guidance, a recording system that registers and keeps track of all intracavitary and external signals, and the fluoroscopy imaging system that provides live x-ray image to check the catheter position within the heart and to guide the transeptal puncture.

for studying the arrhythmia mechanisms driving or sustaining the fibrillation.

They also offer compatibility to integrate computed tomography (CT) or magnetic resonance imaging (MRI) scans into the systems. The reconstructed 3D EAM volume can be merged with the previously generated scans to confirm their similarity, and to check specific heart characteristics that can complement the EAM shell, e.g. fibrotic tissue, infarcted areas, unusual morphology, or veins distribution. Since the EAM system provides catheter navigation as the electrophysiologist operates and advances the catheter, tags can be placed on the 3D maps to highlight interest points.

An example of the common equipment setup employed in an electrophysiology laboratory is shown in Figure 1.18. The signals recorded by the catheter or skin-electrodes are split and fed to the different systems. The setup usually contains 3D EAM for anatomic reconstruction and clinical guidance. Simultaneously, signals are filtered, enhanced, and stored using an operational amplifier and a recording system, and a fluoroscopy imaging system is used to verify the catheter position and to guide the transeptal puncture.

1.5.5 Clinical Solutions

PVI remains the most employed ablation procedure tackling AF termination. Based on the ectopic firing at the pulmonary veins, it tries to electrically isolate the veins from the rest of the left atrium. To help in the procedure, electrophysiologists use EAM and fluoroscopy systems to assist them while advancing the catheter and in the radio-frequency energy delivery to create the tissue lesion. Other studies based on CFAEs, or those creating additional ablation lines with or without PVI lines also employ the same equipment.

Alternatively to PVI, in recent years new solutions (equipments) have been developed to study the existence of rotors and their relationship with AF termination. The temporal stability characteristic of a rotor and its spiral wave pattern, compared to the multiple wavelet irregular propagation, facilitates the development of new algorithms that could detect and confirm the role of rotors as AF drivers. These works detect and characterize drivers using imaging of complex activation patterns. Specific examples are the invasive systems RhythmView™ (Abbott, Topera Medical, San Diego, CA, USA)[88], CARTOFINDER™ (Biosense Webster, Diamond Bar, California, USA)[35], AcQMap® (Acutus Medical, Carlsbad, CA, USA)[47, 78], and non-invasive CardioInsight™ (Medtronic, Minneapolis, MN, USA)[134].

The RhythmView™system, one of the leading technologies in clinical practice, was developed as part of the Focal Input and Rotor Modulation (FIRM) method [88]. For the detection of rotors, the method requires two basket catheters deployed in both atria, exporting the data to perform offline signal processing, and one trained operator to determine the presence of the rotors. The method is based on the detection of electrode local activation to construct isochronal maps. Then, it performs phase analysis by directly applying the Hilbert transform to unipolar EGMs to detect phase singularity points where the tip of the rotor spins [49].

Despite of its promising preliminary results, the above described method presents several limitations: The phase mapping correlates poorly with temporal activation maps [130]. The method needs two basket catheters, which is intrusive for the pa-

tient. The catheter topology presents no efficient deployment and electrode contact [67]. The low spatial resolution mapping of the atria, is prone to false detections [111]. The solution requires signal exportation plus post-processing, which extends the duration of the clinical procedure and prevents reproducibility of results [25, 17].

Similar to RhythmView™, the novel CARTOFINDER™ software was developed to detect and characterize drivers in AF [35], with recent studies confirming rotational activations [26]. This solution also employs a basket catheter to acquire the signals and identify rotational repetitive activation patterns (RAPs). The main difference with respect to RhythmView™ resides in the identification of the unipolar activation in a determined time window defined by the bipolar information of the electrode pairs. The detection of RAPs is based upon visual inspection. The compatibility with the CARTO® 3 3D electroanatomical system allows CARTOFINDER™ to project the activations onto the electroanatomical 3D map, instead of unfolding the atrium into a 2D grid for visualization. However, as it requires the use of basket catheters, CARTOFINDER™ presents the same limitations in terms of electrode deployment and atrial contact as RhythmView™.

The AcQMap® system employs a basket catheter with 48 electrodes and 48 ultrasound transducers to perform non-contact 3D electroanatomical reconstruction and signal acquisition. The ultrasound technology generates maps faster than by using traditional mapping catheters. The electrical activations are calculated with algorithms applied to intracardiac voltage signals and represented as unipolar voltage and Dipole Density™ maps. This system has the advantage of embedding the generated activation maps in the 3D anatomical model for visualization. Nevertheless, the non-contact feature is sensitive to the distance of the electrode to the atrial wall and catheter positioning.

Equally important, non-invasive methods (body invasion and skin cut is prevented) aim to characterize AF prior to the surgical procedure. One example is the CardioInsight™, based on a multi-electrode vest recording body surface ECGs which are combined with CT scan data. While the system is able to display 3D

cardiac epicardial activation maps, it has potential limitations compared to invasive approaches which map endocardial tissue. The assessment of drivers is limited in some particular regions like the septal area, and some tissues between the body surface and the epicardium may affect the signals. Finally, the signal to noise ratio of the system limits its accuracy in the detection for short and small amplitude drivers, and it may not correlate with reentries identified by other systems, although important advances focusing on demonstating this correspondance have been done [108].

1.6 Objectives

The main goal of this thesis is to provide new tools and methods for real-time rotational activation assessment in AF ablation procedures. We want to make use of current available technologies, using using EGMs signals recorded with multi-electrode catheters that provide electrical information of the tissue in direct contact with the electrodes. We want to assess rotational activity detection with new original alternatives to identify electrode LATs and new methods capable of detecting rotational activity, see Figure 1.19. We want to study if reentries can be explained by micro-rotors (which are too small to be mapped with other catheter models or missed by phase analysis approaches). This way we want to help electrophysiologists to further investigate the AF initiation and maintenance mechanisms, which still remain poor and controversial.

One of our objectives is to deliver results in real-time to minimize the procedure duration and to ease the electrophysiologists work. What is more, we want to offer compatibility to different existing catheter topologies, not being restricted to use one model in particular as other solutions do. Additionally, we also want to unveil the directionality of the electrical wavefronts registered in the EGMs by multi-electrode catheters. By knowing the propagation relationships between electrode pairs anomalous wavefront activity can be detected.

Finally, we want to integrate all the new signal processing methodology elaborated for the thesis into a clinical solution to transfer the theoretical methods into

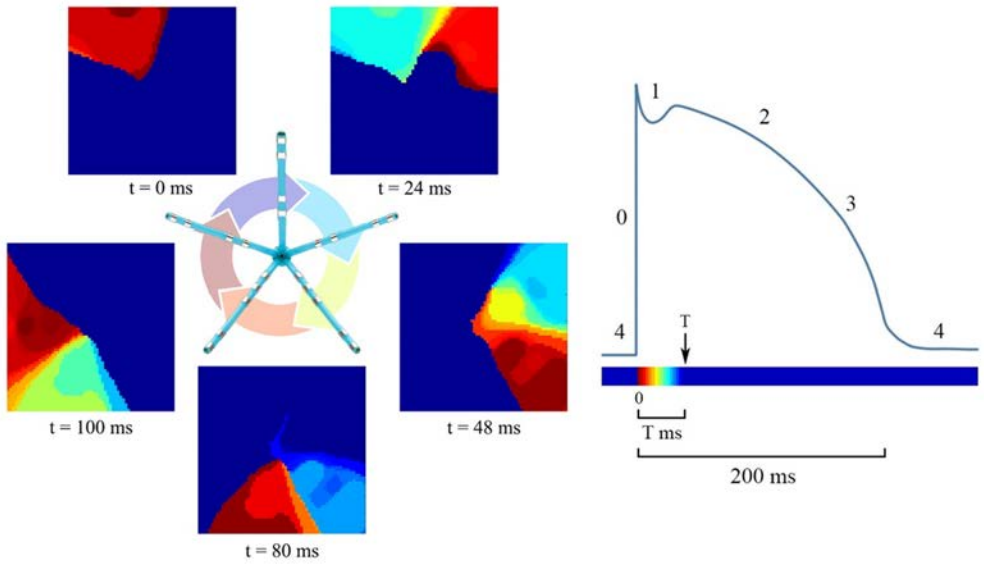

Figure 1.19: Assessment of rotational activation detection based on theactivation times registered with multi-electrode catheters.

practice. We expect the new methods to be of assistance in new and undergoing clinical studies with the final objective of terminating AF.

1.7 Organization and Contributions

This thesis is organized as follows.

Chapter 2 Estimation of Local Activation Times in Unipolar Electrograms. We devote this chapter to the detection of LATs in unipolar EGMs. The methodology is based on the research presented in [102]. From raw EGMs acquired with multi-electrode catheters during AF ablation procedures, we filter the signals and obtain a surrogate of the slope component of the signal. Then, we detect the LAT instants for each individual EGM recording. The methods were validated using *in silico* simulation scenarios and compared to other existing approaches to assess its performance and validity.

In silico simulations are powerful tools for the understanding and managing of AF, since they mimic the behavior of the human physiology. They provide realistic ground truth data which become useful to validate new algorithms and

methods. We generated the signals in a controlled environment, which grants the reproducibility of the results. And what is more important, variations in the simulation parameters can be performed at inexpensive cost.

Chapter 3 Rotational Activity Detection. This chapter is devoted to the detection of rotational activity in real-time from LAT maps. We address rotational detection in the time domain as an alternative to other methods based on phase mapping. We perform a 2D interpolation of the signals with respect to the position of the electrodes in the catheter, and we build the LAT maps. We employ optical flow techniques to extract the dynamics of the wavefronts. We detect rotational activity based on a pattern match approach. The methodology comprising this chapter is presented in [102]. The method was validated using *in silico* scenarios and applied to real AF signals to assess its efficacy.

Chapter 4. Causality Retrieval in Atrial Fibrillation. We analyze the causal relationship between EGMs signals. The methodology of this chapter was presented in [73, 74, 75]. We propose a hierarchical discovery algorithm to estimate the propagation of the wavefront flow based on Granger's causality surrogate measurements. We developed and studied new causality-related indices based on the causal strength of the signals to discover the activation interrelationships in signals recorded by multi-electrode catheters. This way we obtain a graph based representation of the atrial activity, where rotational activation can be distinguished if the graph presents circular distribution. We validated the method using *in silico* and real signals, and we compared it against other existing methods based on Granger's causality.

Chapter 5 Clinical Applications. We cover the clinical application of the methods, including the implementation of the rotational activity detection system operating in real-time. To that end, we took advantage of the parallel processing capabilities of the graphical processing units (GPUs) technology and multicore central processing units (CPUs), and we designed all the methods to be mostly parallelizable. We extended the study on rotational activations with the combination of the rotational detection feature of our system and the electroanatomical

maps of the heart. This way we studied the spatial distribution in the atrium of rotational activation sites. We also characterized the rotor sites in terms of their voltage with measurements registered with the EAM systems. For these studies we developed new tools to analyze and review all the data, i.e., EGMs and 3D electroanatomical maps. The applications in this chapter were included in [28, 102, 104, 105, 113, 114], and a patent application regarding the whole rotational activity system [103].

Chapter 6 Conclusions. Finally, we summarize the main contributions of this thesis and highlight potential research lines to be considered as future work.

The thesis contributions have been published in international journals [102, 75], and conference publications [114, 104, 105, 113, 28, 74, 73]. We also issued a patent application as a result of the work developed in the thesis concerning the rotational activity detection system [103], Additionally, the ongoing work derived from the thesis is expected to give continuity to this research line [33, 32, 99, 100, 101].

2

Estimation of Local Activation Times in Unipolar Electrograms

2.1 Introduction

The local activation time (LAT) detection problem in intracavitary electrograms (EGMs) consists in identifying the precise time instant in which the electrical activation wavefront is right beneath the electrode recording the heart tissue. An accurate estimation of the activity in all the electrodes allows us to unveil the heart activity and this way study the arrhythmia. From the electrode activation patterns we can analyze features such as the directionality of the wavefront, detect anomalous-related patterns possibly associated to the maintenance mechanisms that perpetuate the arrhythmia, or even reconstruct the wavefronts with a visual representation to understand the behavior of the fibrillatory process.

In the literature the LAT detection problem depends on the configuration of the EGM acquisition, i.e., unipolar or bipolar. Bipolar signals offer higher spatial information, since the recording shows the local activity of the tissue comprising the gap between the electrodes contributing to the differential measurement. Although the bipolar configuration is preferred in terms of noise reduction, the accuracy in LAT detection is ambiguous due to the shape of the signal, see Figure 2.1, with different LAT definition methods proposed in the literature [19]. On the other hand, unipolar signals offer higher temporal resolution when detecting the LATs of the wavefronts if compared to bipolar signals, which obscure the morphology of the atrial waveform. In the unipolar case, the LAT can be easily related to the time instant of maximum negative slope [19], i.e., the local minimum values of the first derivative $\frac{dV}{dt}$. What is more, the signal obtained with the unipolar electrode recording the extracellular tissue voltage and its LAT was demonstrated to be related to the cellular action potential (AP) voltage (V_m) [123], where the maximum upstroke of the AP defined by $\frac{dV_m}{dt}$ corresponds to the maximum $-\frac{dV}{dt}$ value of the extracellular voltage [27].

However, unipolar EGM acquisitions are exposed to far-field components. They record the combined contribution of both atrial and ventricular activations. This is a widely known disadvantage, since the bigger size of the ventricle makes the ventricular activation to become the dominant contribution of the EGM, overlaying the atrial component. Fortunately there exist methods to overcome this problem based on the estimation of the ventricle contribution and its subtraction from the unipolar recording. Literature usually refer to them as ventricle cancellation methods.

In the event of noisy and complex fractionated EGMs the LAT identification can be challenging. This originated the development of alternative methods to detect LATs, including the analysis of the frequency domain [58, 59], and the reconstruction of the instantaneous phase of unipolar EGMs using the Hilbert transform (HT) [22, 110, 65]. The HT is a linear operator employed to obtain the instantaneous phase and frequency of a signal, namely $s(t)$. The transformation

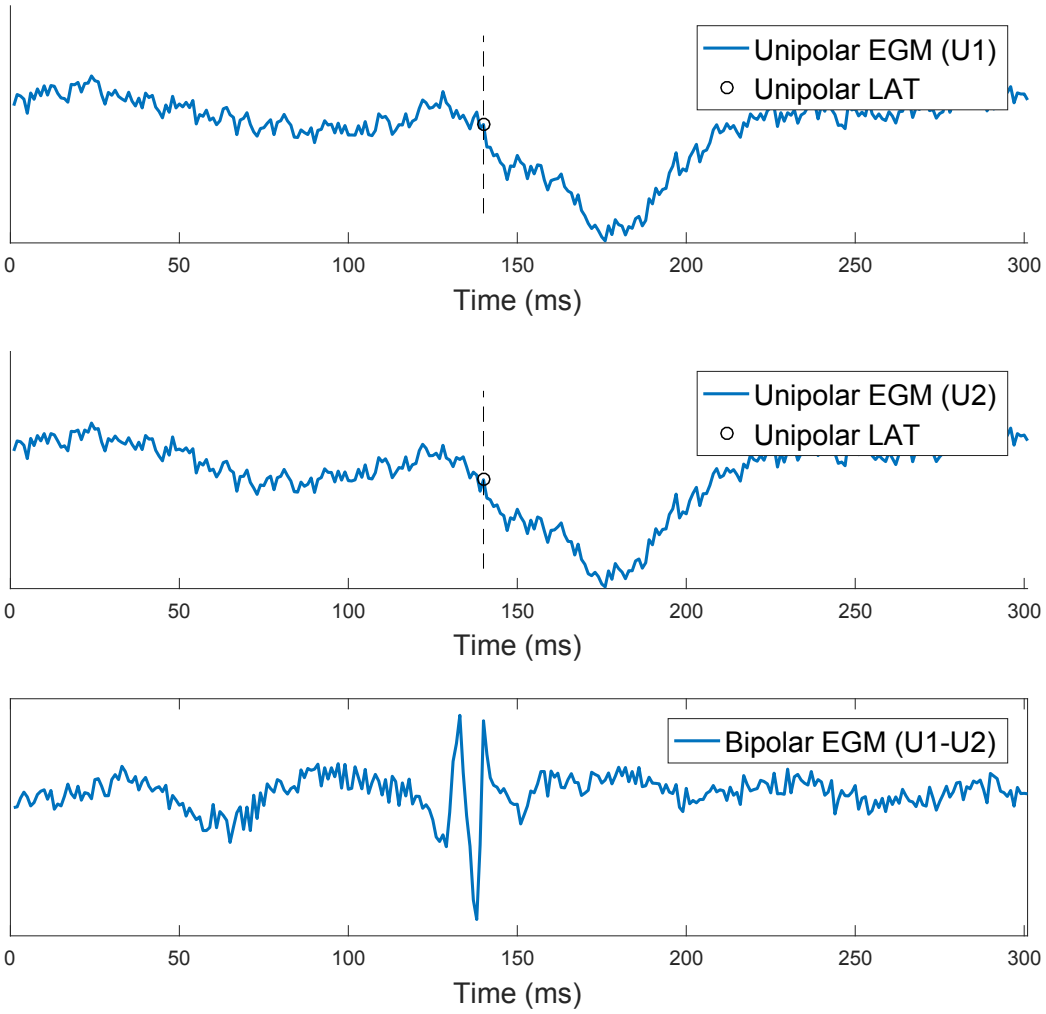

Figure 2.1: Unipolar and bipolar EGM comparison. Top to bottom first unipolar channel (U1), second unipolar channel (U2), and finally the bipolar channel obtain by the differential subtraction of $U1 - U2$. The LAT of both unipolar segments can be defined at the point of maximum $-\frac{dV}{dt}$, whereas the bipolar LAT cannot be so easily defined.

involves the calculation of the function

$$HT(s(t)) = \frac{1}{\pi} P \int_{-\infty}^{\infty} \frac{s(t)}{s(t-\tau)}, \tag{2.1}$$

where variable P stands for the Cauchy principal value of the integral, and τ is the time-embedding lag. A signal and its HT are mathematically orthogonal over the infinite interval, thus a plot of $s(t)$ versus $H(s(t))$ yields to rotations in the phase plane. From the pair of signals the phase can be extracted as the angle defined between them. There exist several alternatives for the formulation of the phase $\theta(t)$, this is one of them [65]

$$\theta(t) = \arctan\left(\frac{-(s(t) - s^*)}{HT(s(t)) - s^*}\right), \tag{2.2}$$

where s^* is the phase plane origin that serves as reference to calculate the phase, which is defined in the interval $\theta \in [-\pi, \pi]$ radians. This one is a modified version from the standard formulation that can be found in diverse toolboxes by setting $s^* = 0$.

The phase information is commonly employed to see the fluctuation in time of the signals, and also to see its repetitive patterns. Although the activity in the signal can be visualized using its phase information, the exact LAT of the EGM cannot be accurately defined, since there is no direct correspondence between the depolarization instant in the EGM and the phase of the signal. For example a value of $\theta(t) = \pi$ radians corresponds to a peak in phase, but it does not imply a direct correspondence with a LAT in the EGM, that can happen at any phase value depending on the signal.

One of the problems when calculating the phase component is the selection of τ, which affects the outcome of the HT. During Atrial fibrillation (AF) the activations happen irregularly in time and their morphology changes, so the selection of τ is not unique as the signal evolves with time. Solutions for this problem have been proposed in the literature, with methods taking into account the fibrillatory scenario applying signal preprocessing detrending or wavelet transformation among other solutions [22, 65].

Additionally, noisy signals can distortion the instantaneous phase, since a small amplitude variation can be analyzed as a phase transition. After all and due to the intrinsic nature of the HT, a time domain activation method is recommended to be used in parallel to avoid false or missing activations [130].

In this chapter, we use unipolar EGMs as input signals to perform LAT detection in the time domain. First, in Section 2.2.1 we correct the baseline wandering of the unipolar EGM and electrocardiogram (ECG) signals, an undesired low frequency component introduced by the respiratory movement of the patient and instrument motion. Secondly, we apply an algorithm to cancel the ventricle contribution based on [122]. This way we obtain EGMs containing the isolated local atrial contribution only, while disposing the far-field effect.

In Section 2.2.2, we introduce a new filtering method for unipolar signals, which enhances the slope of the voltage deflections related to the depolarization of the tissue beneath the electrode. Our method estimates the slope of the signal, while filtering out the contribution of noisy sources, obtaining a signal in which the LATs can be identified. The final LAT detection step is based on an exponential thresholding algorithm [16], with modifications to suit the enhanced signal. The method adapts continuously to variations in the amplitude of the slope, mainly produced by the displacement of the electrode due to the activity of the heart.

2.2 Local Activation Time Identification

2.2.1 Signal Pre-processing and Ventricle Cancellation

Unipolar signals suffer from baseline drift, also called baseline wandering, a low-frequency artifice that appears in ECG signals in the $0.05 - 1$ Hz frequency band [1]. It is caused by the respiration of the patient when the thoracic cage spans and shrinks, producing a small displacement in the position of the surface electrodes placed on the chest of the patient, and also in the intracavitary catheter electrodes. This small distortion makes the baseline voltage of the signals to fluctuate in time, (see Figure 2.4A). The motion and manipulation of certain instruments inside the

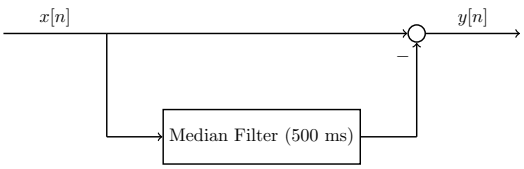

Figure 2.2: Baseline wander removal system using a median filter (MF).

operating room also interfere with the signals, and spikes of great amplitude may appear in the acquisition registers. What is more, additional noisy sources may contribute to the baseline drift, such as power supply noise at $50Hz$ (or $60Hz$), but this is commonly removed with a Notch filter at the specified working frequencies.

For removing the baseline wandering, we estimate the DC signal component applying a causal median filter of 500 ms window length [36], and subtract it from the unipolar signal eliminating the drift effect (Figure 2.4B). The equivalent system representation is shown in Figure 2.2. It contains a MF to extract the baseline contribution, which is latter subtracted from the input signal. We choose the median filter approach rather than other methods in the literature, such as finite impulse response (FIR) filter [136], beat-to-beat mean [122], moving average based filters [60, 34], independent component analysis (ICA) [51], empirical model decomposition (EMD) [20], or discrete wavelet transformation (DWT) [70]. MF offers simplicity, we only need to calculate the median of N past samples to obtain the filter output, while other methods involve more complex and time consuming implementations. Any of these methods would interfere with our objective to deliver real-time results.

The MF acts as a low-pass filter, and it preserves signal structures, such as deflection or edges. If the median filter is applied recurrently to the same signal, it will converge into a signal invariant to additional filtering. In the literature this is called *root signal*, but a similar signal can be obtained using a single filter of a high enough size. In our case, we identify the baseline wander as the root signal contained in the ECG or EGM signal. We contemplated median filters in cascade configuration as in [36], but authors lacked to include scientific reasoning of the signal processing foundation supporting this method. To extract the root

signal, we use a single median filter following the block diagram in Figure 2.2, instead of implementing the multiple cascade configuration. Empirically, bigger filters converge faster to the root signal [10], although shorter filters provide better resolution, as a result of including smaller structures from the input signal that are maintained in the output. However, baseline wander exhibits slow amplitude variation with time, so the inclusion of small structures during the filtering process, like the cascade configuration proposes, is not advantageous for estimating the baseline signal.

With the purpose of validating this assumption, we evaluated the performance of a two stage median filter with sizes $N_1 = 200$ ms and $N_2 = 600$ ms, as proposed in [36], with a single median filter of size $N = 500$ ms. We tested both methods on ECG and unipolar EGM signals. By looking at Figures 2.3A and 2.3B, we see that both implementations behave similarly, and implementing the single median option is computationally cheaper and faster than the dual ensemble. This evidence supports our single MF approach.

Unipolar recordings are also affected by far-field signal contributions. The stronger ventricle signal overlays the atrial activity which has a lower amplitude, occluding atrial activations in the EGMs recordings (see Figure 2.4B). To cancel the ventricle contribution and recover the hidden atrial activations, we calculate the ventricle unipolar pattern affecting each electrode signal. This is done similarly to the average beat subtraction method described in the literature [122], and current EP mapping solutions [35]. We calculate independent patterns for each channel as the electrodes record different atrial positions. To this end, the catheter is assumed to be stationary during the signal acquisition.

A reference ECG signal identifies the scope of the ventricular contribution in the unipolar signals. The ventricle onset and offset are associated in the ECG to the Q-peak and to the T-wave end time instants respectively, as Figure 2.5A shows. The number of beats included for analysis varies depending on the heart rate of the patient and the duration of the acquisition. For this reason we set the minimum signal acquisition time to be at least 10 seconds, i.e., 10 beats for a 60 beats per

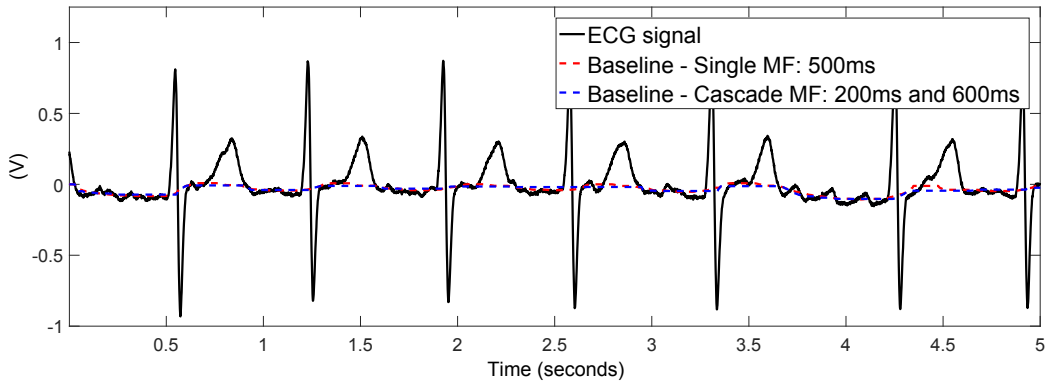

(a)

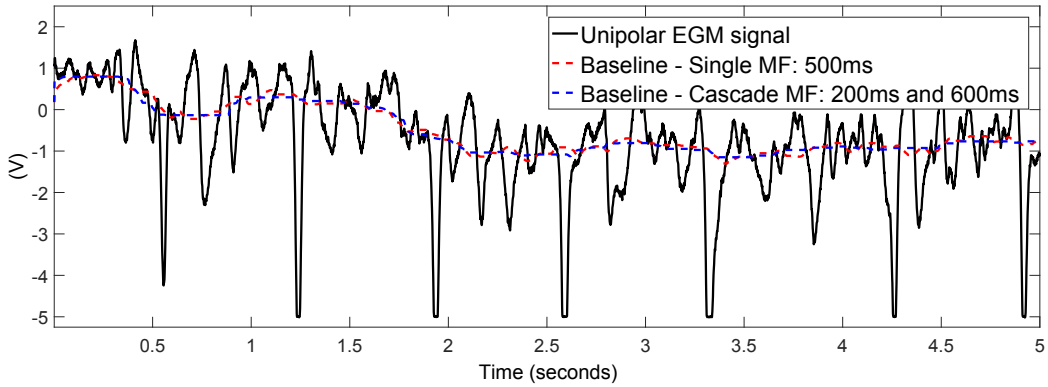

(b)

Figure 2.3: Baseline wandering examples in ECG and EGM signals. The figure exemplifies the comparison of one single median filter of size $N = 500$ ms versus two cascade MFs of sizes $N_1 = 200$ ms and $N_2 = 600$ ms. **(a)** ECG signal and its baseline wander. **(b)** Unipolar EGM signal ans its baseline wander for the same acquisition interval as the ECG in (a). Both figures show in red the baseline component obtained with one filter and in blue when using the cascade system.

minute (bpm) rhythm. We guarantee at least 5 consecutive QRST complexes for a minimum heart rate of 30 bpm. Having 5 QRST complexes is enough to perform ventricle cancellation as demonstrated in other studies [67]. The 2^{nd} DWT scale of the ECG signal, using Daubechies DB4 wavelet, detects the R-peaks locations $R_j^{(i)}$ [31]. Superscript $i = 1, \ldots, N$ corresponds to the *i-th* channel, and subscript $j = 1, \ldots, J$ refers to the *j-th* ventricle activation in the ECG signal containing a total of J activations. This scale corresponds to the $0 - 125$ Hz frequency band of

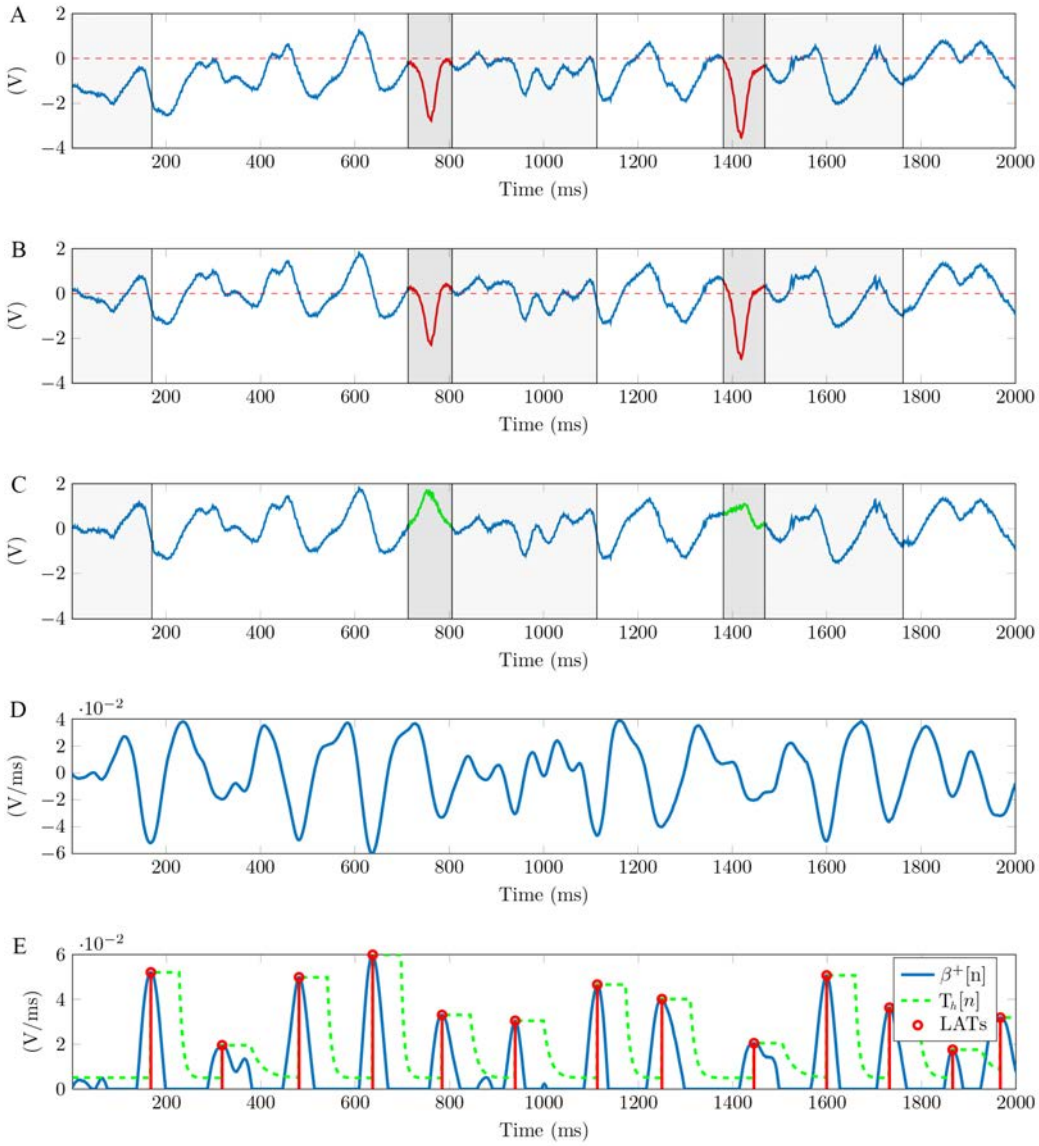

Figure 2.4: Signal processing for LAT detection in unipolar EGMs. **A.** Raw unipolar EGM with ventricle contribution overlaying atrial activations delimited in dark and light gray for the QRS and ST intervals respectively. Level zero DC in dashed red shows the wandering DC offset affecting the signal. **B.** Signal after baseline wandering correction. **C.** Signal after ventricle cancellation, recovering occluded atrial activations shown in green. **D.** Linear pattern approximation of the unipolar slope $\beta[n]$ ($M = 30$ ms in the example). **E.** Unipolar LATs in red detected from $\beta^+[n]$ in blue using an exponential decaying threshold, $T_h[n]$ in dashed green line.

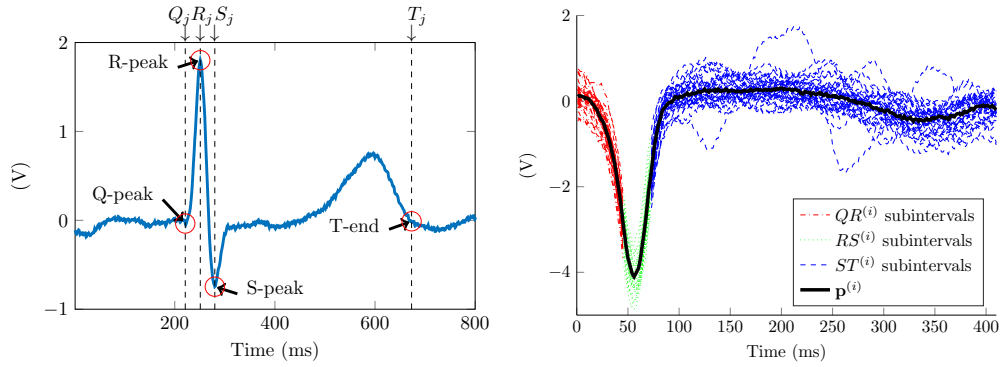

(a) (b)

Figure 2.5: Ventricle cancellation in unipolar EGMs. **(a)** AF ECG with the reference points highlighted in red used for calculating the ventricle pattern. We can see the absence of a P wave, characteristic of AF since the atrium is not properly depolarized. **(b)** Averaged ventricle pattern in black calculated using 36 segments of unipolar channel i. Segments corresponding to the QR, RS and ST subintervals are represented in red, green and blue respectively.

the signal for a sampling frequency $f_s = 1$ KHz. This frequency band covers the typical $0.05 - 100$ Hz processing bandwidth for diagnostic ECG signals [129].

We threshold the signal and detect the R-peaks. A local search (± 20 ms) corrects the $R_j^{(i)}$ time shifts when the DWT peak is converted back to the original scale. Once $R_j^{(i)}$ is found, a local search to the left of R-Peaks obtains the Q-Peaks in the ECG signal. The minimum in the $[R_j^{(i)} - 50 \text{ ms}, R_j^{(i)} - 10 \text{ ms}]$ interval corresponds to the $Q_j^{(i)}$ locations. Following the same searching procedure, the S-Peak is the minimum located within the $[R_j^{(i)} + 5 \text{ ms}, R_j^{(i)} + 50 \text{ ms}]$ temporal window. An algorithm designed for positive T-waves detects the T-wave ends [136]. From all the external ECG leads the method needs one exhibiting T-wave concave morphology, i.e., lead I, V3, V4, or V5. The area under the curve is calculated using a 32 ms length overlapping sliding window with a one sample shift in an interval containing the T-wave. The time instant maximizing the area value gives the $T_j^{(i)}$ location.

Then, for each i-th channel we align all the unipolar segments in the range

$[Q_j^{(i)}, T_j^{(i)}]$ and obtain the ventricle pattern as the median of the channel segments (Figure 2.5B). The T-wave contribution to the unipolar signal is smaller than the QRS complex, for this reason we represent the QS and ST sub-intervals overlaying the atrial signal in dark and light gray respectively in Figure 2.4A-C. To cancel every ventricle contribution, the pattern and each segment are aligned before subtraction. The time shift is given by the maximum correlation time instant between the two signals. Finally, the pattern subtraction removes the ventricle contribution from the unipolar segment (Figure 2.4C).

2.2.2 Detection of Local Activation Times

Depolarizations are characterized by an abrupt deflection of the action potential recorded by the catheter. Depending on different factors (i.e., conduction speed, atrium area, antiarrhythmic drugs) the downward slope duration of an atrial activation varies. Figure 2.6 shows this variation with falls lasting 23, 29, 26, 25, and 33 ms. We propose a new method to identify local activation times (LATs) in EGMs by searching a pattern exhibiting a linear deflection.

We approximate the EGM signal $x[n]$ by the linear function in the interval defined by a $2M+1$ samples window centered at time instant n_0, expressed as

$$\hat{x}\,[n] = \beta[n_0](n - n_0), \quad \text{for } n \in [n_0 - M, n_0 + M], \tag{2.3}$$

where $\beta[n_0]$ represents the function slope value at time n_0. We estimate $\beta[n_0]$ by minimizing the Mean Square Error (MSE) of the error function $\zeta[n_0]$ defined as

$$\zeta\,[n_0] = \sum_{n=-M}^{M} |x[n_0+n] - \hat{x}[n]|^2 = \sum_{n=-M}^{M} |x[n_0+n] - \beta[n_0]\cdot n|^2. \tag{2.4}$$

We include the $\hat{\beta}_{MSE}[n_0]$ derivation. We calculate the first derivative of $\zeta[n_0]$ with respect to $\beta[n_0]$, and set it to zero,

$$\frac{\partial \zeta\,[n_0]}{\partial \beta[n_0]} = \frac{\partial}{\partial \beta[n_0]} \left\{ \sum_{n=-M}^{M} |x[n_0+n] - \beta[n_0]\cdot n|^2 \right\} \tag{2.5}$$

$$= \sum_{n=-M}^{M} \left\{ -2n\cdot x[n_0+n] + 2n^2 \cdot \beta[n_0] \right\} \tag{2.6}$$

$$= 0. \tag{2.7}$$

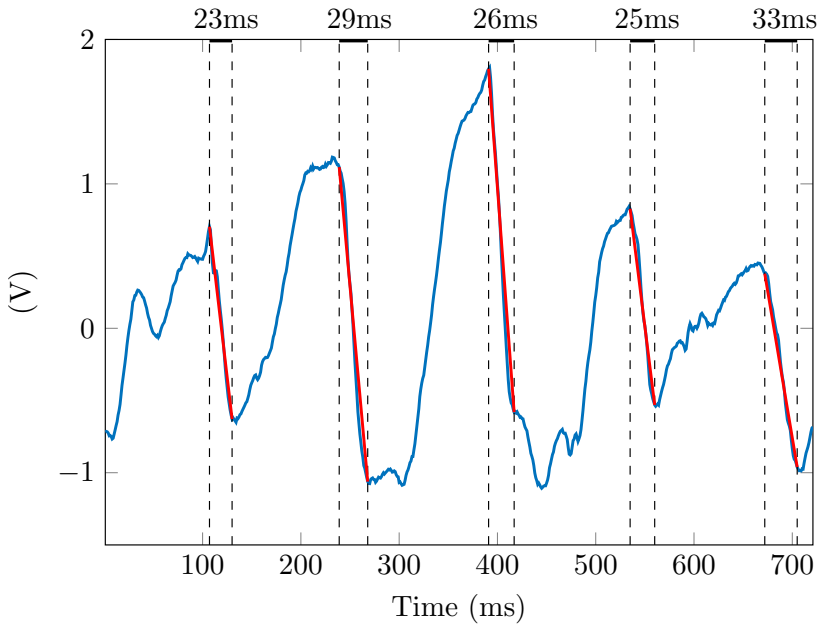

Figure 2.6: Unipolar recording after ventricle cancellation with depolarizations in red and their durations annotated between dashed lines in black.

Solving for $\beta[n_0]$ in Equation (2.5), we obtain the value of $\beta[n_0]$ minimizing the MSE,

$$\hat{\beta}_{MSE}[n_0] = \frac{\sum_{n=-M}^{M} n \cdot x[n_0 + n]}{\sum_{n=-M}^{M} n^2}. \tag{2.8}$$

The denominator of Equation (2.8) is a constant that depends on the window length M which simplifies the expression to

$$\hat{\beta}_{MSE}[n_0] = \mathcal{M} \cdot \sum_{n=-M}^{M} n \cdot x[n_0 + n], \tag{2.9}$$

where $\mathcal{M} = \left(\sum_{n=-M}^{M} n^2 \right)^{-1}$.

Additionally, we characterize the linear pattern approximation, which applied to EGMs resembles the outcome of a first derivative operator multiplied by the constant that depends on the window size M. The expression in Equation (2.9)

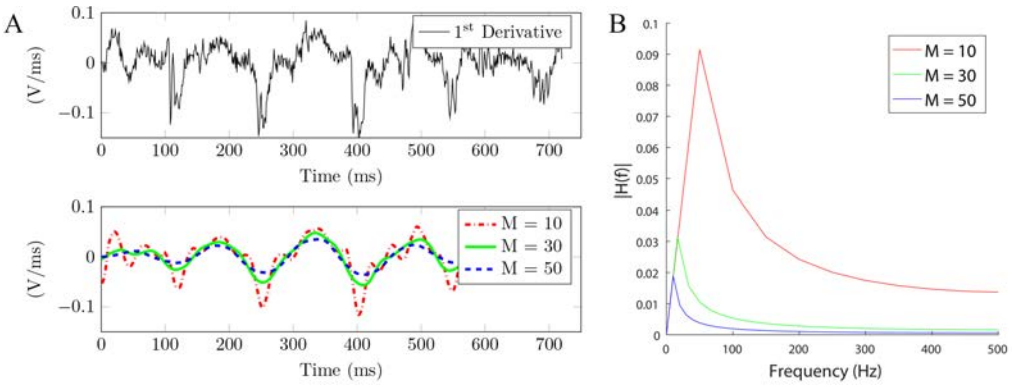

Figure 2.7: Signal slope characterization. **A.** Top. Unipolar signal first derivative. Bottom. Unipolar signal slope approximation for different window length values, M in ms. **B.** Frequency response of the equivalent filter $h[n]$ in Equation (2.10) for different M values.

can be seen as a filter with impulse response

$$h[n] = \mathcal{M} \cdot \sum_{\tau=-M}^{M} \tau \cdot \delta[n-\tau], \tag{2.10}$$

and frequency response $H(f)$ (Figure 2.7B), equivalent to a discrete-time low pass differentiator. In section 2.3 Results, we analyze the effects of selecting the window length M on the amplitude and frequency components of the signal.

In the following, and since there is no ambiguity, we shall drop the subindex in the n_0 and simply refer to it as n. The signal $\beta[n]$ (Figure 2.4D) is inverted and rectified obtaining a new signal $\beta^+[n]$ (Figure 2.4E). The inversion pairs deflections with positive peaks of the signal, and the rectification discards the atrial components with positive slope. Then, the position of the positive peaks are assumed to correspond to the LATs.

The amplitude of the $\beta^+[n]$ peaks varies from activation to activation. These deviations are a consequence of the constant heart activity that prevents the electrodes from having a uniform atrial contact, resulting in amplitude changes. An exponentially decaying threshold after a peak detection is implemented to search for the local activation times [16]. The threshold $T_h[n]$ is updated at each time

instant as

$$T_h[n] = \begin{cases} (M_i - \sigma)e^{-\frac{M_i-\sigma}{\tau}(n-(n_i+b))} + \sigma, & \text{if } n > n_i + b, \\ M_i, & \text{if } n_i < n \leq n_i + b. \end{cases} \tag{2.11}$$

Variables M_i and n_i are the amplitude and time instant of the last detected peak. Time variable τ defines the decay rate of the exponential function. The constant σ specifies a lower limit for the threshold, filtering out small interferences or weak far-field contributions. The threshold is initialized to $M_0 = \sigma$. Close depolarizations are physiologically improbable due to the refractory period of the tissue. To avoid false positives in this period, the threshold maintains its value for a blank period b before detecting a new peak. The algorithm detects a local activation time when a peak of the signal is above the threshold value, as Figure 2.4E shows. A local search for possible undetected peaks in a window of length b around each detected peak prevents false local maxima to be considered as activation instants.

2.3 Results

We evaluated the LATs detection in real AF and computer model EGMs. We validated our method by direct look at the EGMs and LATs outcomes with expert knowledge from electrophysiologists and fine adjustment of the parameters taking into account noise reduction, electrode adjacency to maximize the detection of activations (for both real and simulated signals). We considered a range of $20 - 40$ ms as the span of a depolarization, which corroborates previous results [135, 87].

We used the unipolar signal in Figure 2.6 to analyze the filtering effect of parameter M comparing it with the unipolar signal first derivative used by other authors to identify LATs. Our method provides a smoother and less noisy signal than the one obtained with the first derivative, see Figure 2.7A. This makes it easier to identify the LATs, where our method presents high $\hat{\beta}_{MSE}[n]$ values when the pattern matches a deflection.

In terms of frequency effects, small values of M produce a higher cut-off frequency, whereas big values of M present a more restrictive low pass characteristic

which filters more noise, see Figure 2.7B. This is helpful in noisy EGMs, where small residual peaks appear, and complementary, the exponential decaying threshold demonstrated to recover from false high peaks. The steep threshold drop avoids LAT error propagation that would lead to miss the next atrial activations. Value τ was set empirically to $\tau = 3.5 \cdot 10^{-3}$ by reviewing atrial activations. We also found threshold parameter b crucial in the event of fragmented EGMs, by adjusting the blank period to several ms (60 ms) the fragmented activity can be detected and taken into account in the reconstructed wavefront. This value was selected to be above the classical dominant frequency (DF) range of $4 - 9$ Hz shown by most studies [112]. On the other hand, higher values would not allow the threshold to decay fast enough for the next activation to be detected, missing LATs. The value of $b = 60$ ms was also proposed according to the closeness of consecutive atrial activations and the recovery time for the exponential threshold to reach its minimum value σ. When the next activation exhibited smaller peak amplitude, values greater than 60 ms incurred in missing atrial activations, since the threshold was not fast enough to decay and identify the $\beta^+[n]$ positive peak. We tried different values for b and finally selected $b = 60$ ms.

In terms of amplitude, the window selection has a direct effect on the amplitude of the filtered signal. From Figure 2.7A (bottom) we can see this behavior as the value of the window M is increased. The signal becomes softened at the expense of reducing its amplitude. The same interpretation is derived from the frequency response analysis in Figure 2.7B, where the amplitude of the frequency spectrum becomes reduced as M increases.

After analyzing the effect on the window length selection, we can conclude that employing an over-sized window length would lead the peaks to be less well defined because the signal becomes flatter, but as an advantage unipolar noise is greatly reduced. On the other hand, having a window too narrow (small M) would produce sharper transitions but would be more sensitive to small deflections that might be miss-detected as LATs.

Furthermore, we want to compare our LAT detection method versus the phase

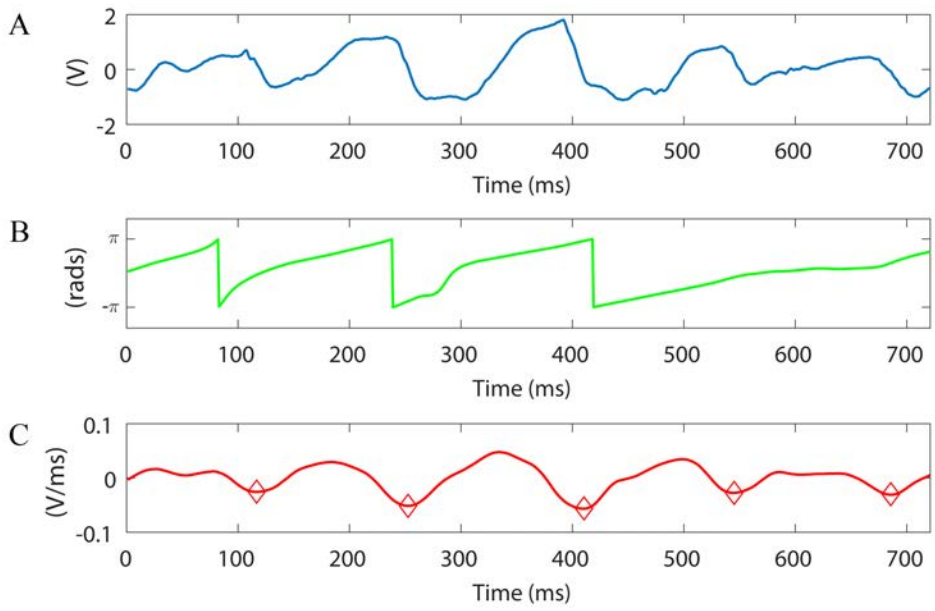

Figure 2.8: Signal slope and Hilbert transform phase comparison. **A.** Unipolar signal. Bottom. Unipolar signal slope approximation for different window length values, M in ms. **B.** Hilbert transform phase applied to the signal in A. **C.** Unipolar slope approximation applied to the signal in A, $M = 30$ ms. Red circles denote the LATs calculated with our method

signal obtained with the Hilbert transform [66]. One representative example comparing both methods is shown in Figure 2.8A-C, using the same unipolar signal as in Figure 2.6. In the example, our method is able to capture all the activation time instants, denoted as diamonds Figure 2.8C. We can clearly identify the missing phase transition at the 4th and 5th atrial activations. In this situation the Hilbert transform is not reliable, confirming previous results on weak correlation between phase and activation maps [130]. Moreover, the Hilbert transform requires an estimation of the signal period, calculated as the dominant frequency of the segment which can vary in time. Additionally in Figure 2.8B we can see how the first phase transition drops from π to $-\pi$ radians preceding the first two activations (34 ms and 13 ms respectively), and after them it gets delayed (10 ms) in the third activation. This is a meaningful variation that may lead to a potential

misinterpretation of the atrial activity. Since our method relies on beat to beat detection it does not shift the LATs from activation to activation.

2.4 Conclusions

We identify that LAT information in unipolar EGMs can be of potential value as an alternative to phase mapping analysis. More particularly, our EGM filtering and LAT detection approach emerges as an alternative for EGM signal processing, being extendable to other kind of biological signals, e.g. electroencephalograms, electromyograms, or galvanic skin response.

3

Rotational Activity Detection

3.1 Introduction

Rotors and their associated re-entry spiral waves are suggested to play an important role in the mechanism perpetruating Atrial fibrillation (AF) [92]. By definition, re-entrant waves rotate around a singularity phase point, and its detection is normally assessed by the identification of the center of rotation.

In the late eighties the analysis of the phase concerning the study of cardiac fibrillation was first introduced by Winfree [132]. By defining a time delay τ, he plotted the state variable $V(t)$ versus a delayed version at time instant $t-\tau$ $V(t+\tau)$, obtaining a phase-space trajectory which encompassed a fixed origin, see Figure 3.1(A-C). In the AF context, intracardiac electrograms (EGMs) or voltage values generated by an excitable-propagation models play the role of the state variable, defined as $V(t)$, with $V(t+\tau)$ being its delayed value.

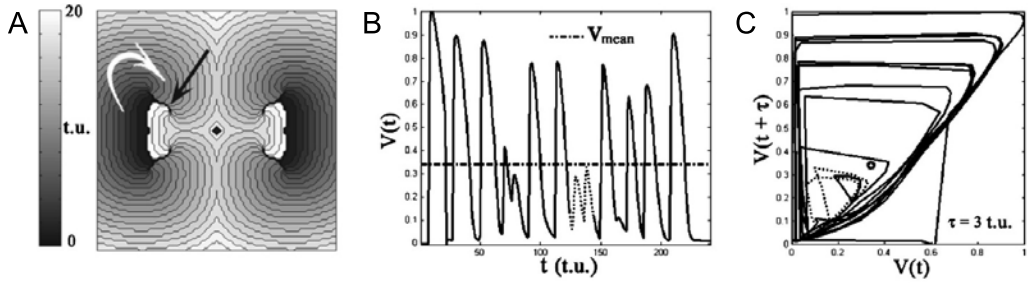

Figure 3.1: Figure extracted from [22]. **A.** Isochronal map for a computer simulated scenario. **B.** Measured transmembrane signal $V(t)$. **C.** Phase excursion of the signal in (B) with $\tau = 3$.

To guarantee linear independence between $V(t)$ and $V(t+\tau)$, their correlation function is calculated and τ is normally chosen as the first zero crossing [2]. Finally, the spatial phase map can be calculated for all coordinates (x, y) of a spatial 2D grid as

$$\theta(x, y, t) = arctan\left[\frac{V(x, y, t+\tau) - V_{mean}(x, y)}{V(x, y, t) - V_{mean}(x, y)}\right], \tag{3.1}$$

where $V_{mean}(x, y)$ is the mean voltage value at location (x, y) and $\theta \in [-\pi, \pi]$ radians.

The main drawback of this practice lies in the errors associated to a poor choice of τ, and the fact that the resultant phase-space trajectories may not encircle the origin reference. Analytically, a small value of τ is equivalent to a high correlation of the variables, hence the signal $V(t)$ can be approximated to $V(t) \approx V(t+\tau)$. In this case, the phase points will lie in the diagonal of the phase-space. On the other hand, setting a large of τ value may lead to high uncorrelated data deforming and stretching the trajectory. Additionally, rotors may drift and suffer morphology changes, so the optimal τ may differ along time.

To better visualize all the information isochronal maps are normally employed. They spatially represent the value of a variable, e.g. voltage or phase component, in a color-coded image like the one displayed in Figure 3.1A. These maps are commonly used when representing the cardiac electrical wavefronts and the voltage values in electroanatomical mapping (EAM) systems.

For the detection of rotors current solutions base their assessment in the iden-

tification of phase singularities (PSs) contained in the isochronal phase maps of the mapped atrial tissue. By definition, *"A spatial phase singularity is a site in an excitable medium at which the phase of the site is arbitrary; the neighbouring elements exhibit a continuous progression of phase that is equal to $\pm 2\pi$ around this site"* [49].

PSs represent points whose surrounding neighbors follow the complete $[-\pi, \pi]$ interval [49, 21]. In the event of a re-entrant spiral wave, the tip of the rotor is surrounded by points ranging all the stages of the action potential (activation-recovery) cycle, defining a PS at that location. Therefore the analysis of the phase descriptor in these locations becomes of great interest to detect rotational activity.

The PS is described in terms of topologic charge n_t [46, 81] [1],

$$n_t \equiv \frac{1}{2\pi} \oint_c \nabla\theta \Delta\vec{dl}, \tag{3.2}$$

where the line integral is calculated over the path described by $\vec{l}$ on a closed curve c around the topological point and $\theta(\vec{r})$ stands for the local phase. As n_t is an integer value its sign reflects the clockwise/counterclockwise rotation.

If we apply the gradient of the phase to a wave vector field, $\vec{k}(\vec{r}, t) \equiv \theta(\vec{r}, t)$, evaluating n_t for a closed path in the limit as the area goes to zero, we see that n_t is proportional to the curl of the wave vector

$$\nabla \times \vec{k} = \begin{vmatrix} \vec{\mathbf{x}} & \vec{\mathbf{y}} & \vec{\mathbf{z}} \\ \frac{\partial}{\partial x} & \frac{\partial}{\partial y} & \frac{\partial}{\partial z} \\ k_x & k_y & k_z \end{vmatrix} = \left(\frac{\partial k_x}{\partial y} - \frac{\partial k_y}{\partial z}\right)\vec{\mathbf{x}} + \left(\frac{\partial k_z}{\partial x} - \frac{\partial k_x}{\partial z}\right)\vec{\mathbf{y}} + \left(\frac{\partial k_y}{\partial x} - \frac{\partial k_x}{\partial y}\right)\vec{\mathbf{z}}. \tag{3.3}$$

At a location $[m, n, p]$ the integral can be rewritten as

$$\oint_c \nabla\theta \Delta\vec{dl} \propto \nabla_x \otimes k_y + \nabla_y \otimes k_x, \tag{3.4}$$

where $\otimes$ is a convolution operator, ∇_x and ∇_y are the convolution kernels

$$\nabla_x = \begin{bmatrix} +1 & -1 \\ 0 & 0 \end{bmatrix} \qquad \nabla_y = \begin{bmatrix} -1 & 0 \\ 1 & 0 \end{bmatrix}. \tag{3.5}$$

[1] Also used in [21, 23, 137]

As explained before, the choice of τ becomes a limitation when calculating phase-maps, Bray et al [22] developed a procedure for detecting PS points regardless of τ. In this algorithm, already mentioned in Chapter 2, they alleviate this disadvantage by subtracting the average mean of the signal and employing the Hilbert transform (HT).

The HT is a robust approach to calculate instantaneous phase [22, 128, 94, 127]. When assuming stationarity and linearity, autoregressive moving average (ARMA), principal component analysis (PCA) or independent component analysis (ICA) are frequently used to decompose the signal. Similarly, fast Fourier transform (FFT) is of great help as it describes the frequency spectrum of the signal, where the main limitation is satisfying Nyquist's criterion. Problem arises when signal is nonstationary, nonlinear and noisy, as it happens with intracavitary signals during AF. Under these circumstances, HT is preferred because it expresses frequency as a rate of change in phase, allowing changes in the frequency along time, while contributing with high temporal resolution of rapid changes in the state variables for phase, amplitude and frequency.

Taking as analytic signal $V(t)$ with real and imaginary parts $V_r(t)$ and $V_i(t)$ respectively,

$$HT(V(t)) = \frac{1}{\pi} P \int_{\infty}^{-\infty} \frac{V(t')}{(t-t')} dt', \tag{3.6}$$

where P is the Cauchy Principal Value. This expression gives a point in the complex plane for every signal sample. Following these points in time, a circular trajectory is obtained reflecting the rotation of the tip of a vector, see Figure 3.1C. The amplitude $A(t)$ and phase $\theta(t)$ of the vector can be computed as

$$A(t) = \sqrt{v^2(t) + u^2(t)} \qquad \theta(t) = \arctan\left(\frac{V_i(t)}{V_r(t)}\right) \tag{3.7}$$

Literature on tracking rotors relies on the trajectory described by the tip of a re-entrant wave [128]. By plotting the PS in time, the path described by a drifting rotor can be followed, also called filament. The path described by the tip of the rotor is also called filament. In our problem we need to represent the

individual electrode signals into an isochronal representation to track the rotational activity of the wavefronts. To achieve such task, in Section 3.2.1 we perform spatial interpolation to reconstruct the wavefront and this way visualize the atrial activity. Data interpolation is used to improve the spatial resolution of the acquired signals, easing the spatial analysis of the fibrillation process. The interpolation method obtains a 2D grid combining the spatial information of the electrode positions, and the enhanced signal obtained from the unipolar recordings, prior to the activation detection step. The electrode locations are fixed to represent the catheter when it is fully spread, but that also means the method is compatible with other catheters with different electrode layout distributions.

After the interpolation, in Section 3.2.2 we calculate the local activation times (LATs) for every node in the interpolated grid applying the LAT detection method introduced in Chapter 2. Once the LAT step is done, in Section 3.2.3 we apply a novel algorithm based on the optical flow of correlative isochronal maps containing the LAT information of the grid. We capture the wavefront dynamics with a pattern match approach and a double threshold detector, which is able to identify the rotational activity present in isochronal maps.

3.2 Rotational Activity Detection

3.2.1 Interpolation

In the atrium, depolarization flanks propagate locally as a consequence of the ionic sodium currents firing the cardiac cells through neighboring atrial tissue. We use signal spatial interpolation to represent the atrial activity in the area covered by the catheter. The subsequent processing thus becomes independent of the electrode topology employed. We have several potential magnitude candidates for interpolation: unipolar signals, local activations, and unipolar slopes. From the interpolation candidates, unipolar signals after ventricle cancellation produce noisy and ambiguous maps. The noise component inherent in the unipolar signal affects the LATs outcome, therefore performing an interpolation with noisy data

is not recommended and should be avoided. Local activation times using binary signals (value 1 for LATs and 0 otherwise) offer poor discontinuous representation when recovering wavefronts. This interpolation does not preserve the dynamics of the wavefront since the nodes are only active one time instant corresponding to the LAT of the electrode associated to the grid node. To overcome these potential issues we choose to interpolate the signal $\beta[n]$. It provides a continuous transition, noise reduction, and contains information about the activation measures, coherent with the depolarization propagation basis in the atrium.

For the interpolation, we use a 2 dimensional (2D) squared grid consisting of $J \times J$ nodes, namely $n_{j,k}$ with $j, k \in [1, J]$, representing the atrial tissue covered by the catheter. The grid size is also related to the spatial resolution, e.g. for a PentaRay® (Biosense Webster, Diamond Bar, California, USA)catheter range of 32 mm and $J = 32$ each node represents 1 mm^2. In the grid, each $\beta^{(i)}[n]$ signal is mapped to the fixed spatial coordinate proportional to their location in the physical catheter, referring to these information nodes as $n^{(i)}$. All these nodes belong to the set $\mathcal{N}$. Grid nodes containing no signal are filled by means of interpolation using Shepard's method [120]. This interpolation technique uses inverse distance weighting to find an interpolated value based on the signals $\beta^{(i)}[n]$ for $i = 1, \ldots, N$, and their node positions in the grid $n^{(i)}$. The function for obtaining the interpolated signal $\beta_{(j,k)}[n]$ is defined as

$$\beta_{(j,k)}[n] = \begin{cases} \beta^{(i)}[n], & \text{if } n_{(j,k)} \in \mathcal{N}, \\ \frac{\sum_{i=1}^{N} w^{(i)}(n_{(j,k)}) \cdot \beta^{(i)}[n]}{\sum_{i=1}^{N} w^{(i)}(n_{(j,k)})}, & \text{otherwise,} \end{cases} \tag{3.8}$$

where

$$w^{(i)}(n_{(j,k)}) = \frac{1}{d(n_{(j,k)}, n^{(i)})^p}, \tag{3.9}$$

being $d(\cdot, \cdot)$ any distance metric operator and p a positive real number power parameter. We use the Euclidean distance between the node positions since we employ two dimensional coordinates. In presence of 2D data, choosing $p \leq 2$ causes the interpolated data to be dominated by far away points, so choosing $p = 3$ or 4 provides a better interpretation of local region information. After the

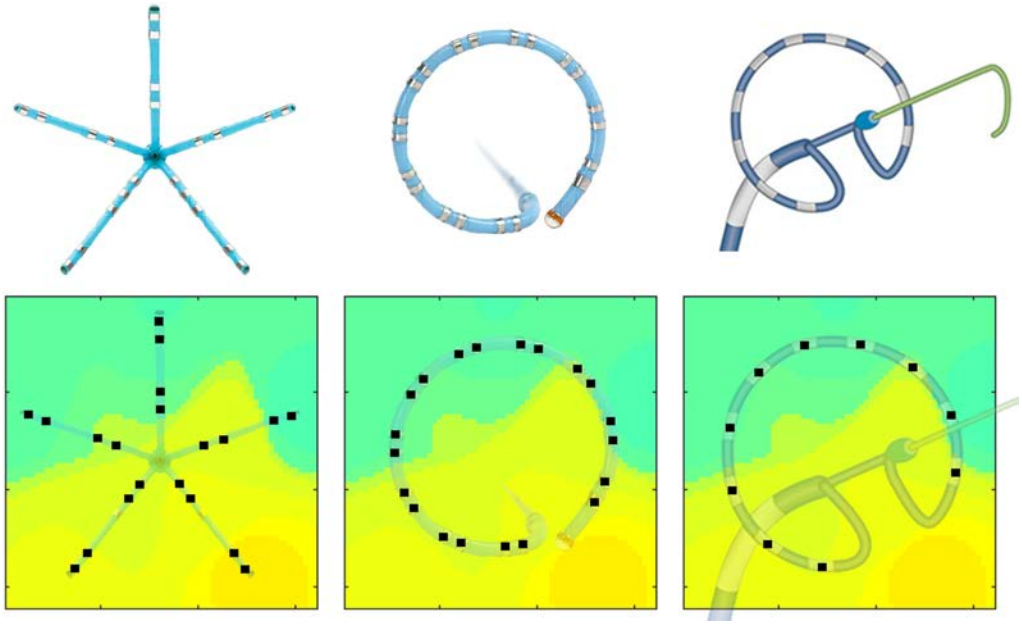

Figure 3.2: Spatial interpolation with different catheter layouts. A: Pentameric catheter with 20 electrodes. B: Circular catheter with 20 electrodes. C: Circular catheter with 10 equally spaced electrodes.

interpolation, we apply LATs detection to all the grid nodes. While electrode positions are assumed to be not known in our method, Eq. (3.8) and Eq. (3.9) can be easily adapted to reflect variable electrode position dependency in time and update the grid positions accordingly, see Figure 3.2.

The interpolation method necessarily needs reliable ground truth data to prove its efficacy. For this reason we validated the spatial interpolation using *in silico* signals generated from a realistic atrial 3D model developed at the Karlsruhe Institute of Technology [117]. The model implements fiber orientation, spatial heterogeneities, and anisotropy conduction for both conduction velocity and ionic currents. Simulations were performed as in a previous study [115], with the AF-remodeled version of the cellular model by [77]. Simulations were run with the software Elvira [52], and unipolar pseudo-electrogram (pEGM) were calculated at each of these electrodes [14]. The integration time step for the 3D atria simulations was 0.04 ms to properly generate the fast upstrokes of the action potential. The output voltages were post-processed every 1 ms to match the real AF signal

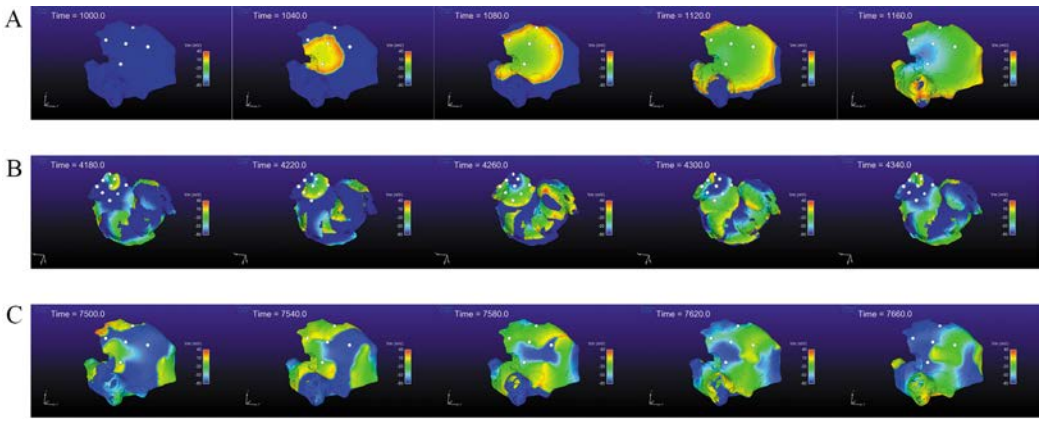

Figure 3.3: *In silico* simulation scenarios. A: Sinus rhythm, 500 ms period. B: Rotor. C: Chaotic wavefront collisions.

acquired at a sampling frequency of $f_s = 1$ KHz.

In the *in silico* simulations (Figure 3.3), we considered different activity scenarios: sinus rhythm, rotor, and chaotic wavefront collisions exhibiting different propagation directions. The stimulation protocol applied a periodic stimuli for the sinus rhythm case, and forced extra-stimuli to generate reentries and fibrillatory behavior for the other cases. The recording positions in the atrium were manually chosen for the three scenarios. We deployed a squared 16x16 node grid, emulating 256 different electrodes recording the pEGM and action potential (AP) signals. The grid was seized to fit the same area as the one covered with a PentaRay®catheter. We simulated 10 seconds at a sampling frequency $f_s = 1$ KHz.

3.2.2 Isochronal Activation Maps

From the LATs, we represent the activations on the grid using isochronal maps [54]. We employ a visualization similar to other authors [9, 88, 15]. The map takes value 0 when the node is active and linearly decrements its value until next activation occurs. For this purpose, we introduce a new variable $a[n]$ expressing the elapsed time since the last activation occurred. We use a simple linear function that decrements its value every time instant when there is no new activation, see

Figure 3.4 (Bottom). This new variable can be formally specified as

$$a[n] = \begin{cases} 0, & \text{if } \beta^+[n] \text{ is a maximum,} \\ a[n-1] - 1, & \text{otherwise.} \end{cases} \tag{3.10}$$

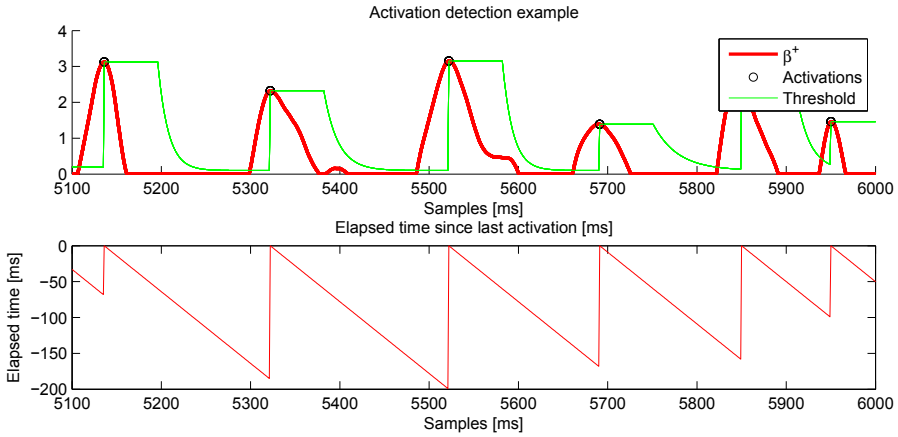

Figure 3.4: Activation detection example. **Top.** A segment of $\beta^+[n]$ is shown in red together with its threshold value in green (amplitude values have been amplified). **Bottom.** Linear function representing the time since the last detected activation.

For visual representation, the last P previous time instants of the signal are displayed (e.g. $P = 40$ ms), with smaller intervals producing narrower wavefronts. The most recent activated node will take a hotter color (red) and will cool down as time passes (blue) until a new activation occurs. Figure 3.5 provides an example of isochronal maps for $P = 50$ ms, one acquired during sinus rhythm (SR) and the other in the event of a rotational atrial activation.

3.2.3 Optical Flow

We propose to detect the presence of rotational activity on the isochronal maps estimating their optical flow [91]. Given two consecutive images (Figure 3.6A-B), it returns the velocity vectors $\vec{u}$ and $\vec{v}$ based on the difference of the two images, providing the propagation direction of the atrial wavefronts at each grid node, as Figure 3.6C shows.

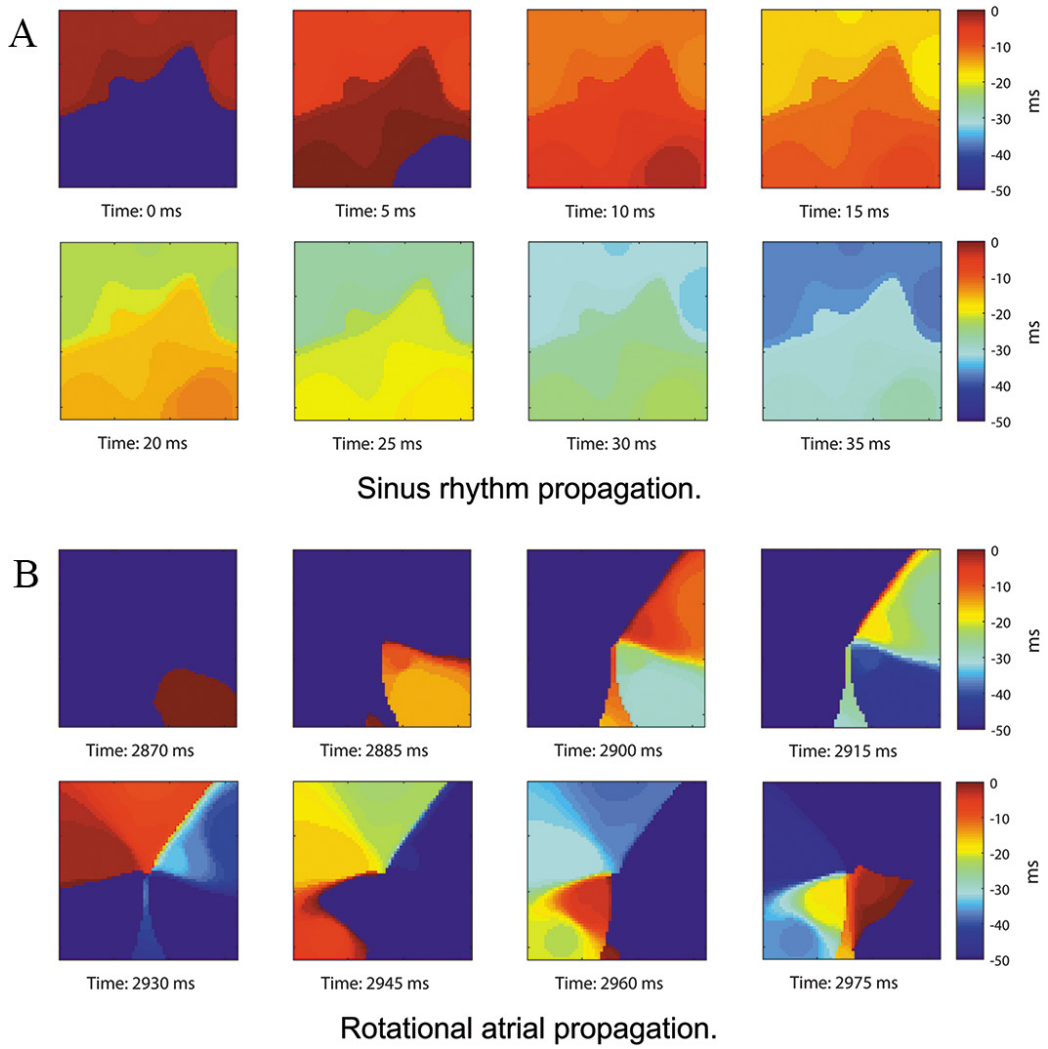

Figure 3.5: Real data propagation. Signals acquired with a PentaRay®catheter at 8 different time instants showing the thresholded grid in the $[-P, 0]$ ms range when a wavefront propagates, $P = 50$ ms. **A.** Sinus rhythm activity propagating from top to bottom. **B.** Propagation exhibiting counterclockwise rotational activity.

Defining image intensity $I(\vec{x}, t)$ as a function of time t and space $\vec{x} = [x, y]^T$, the intensity translation can be expressed as

$$I(\vec{x}, t) = I(\vec{x} + \vec{r}, t + 1), \tag{3.11}$$

where $\vec{r} = [u, v]^T$ is the 2D velocity vector. In our case, $I(\vec{x}, t)$ corresponds to the elapsed time since an activation occurred at node $n_{j,k}$. Although many estimation

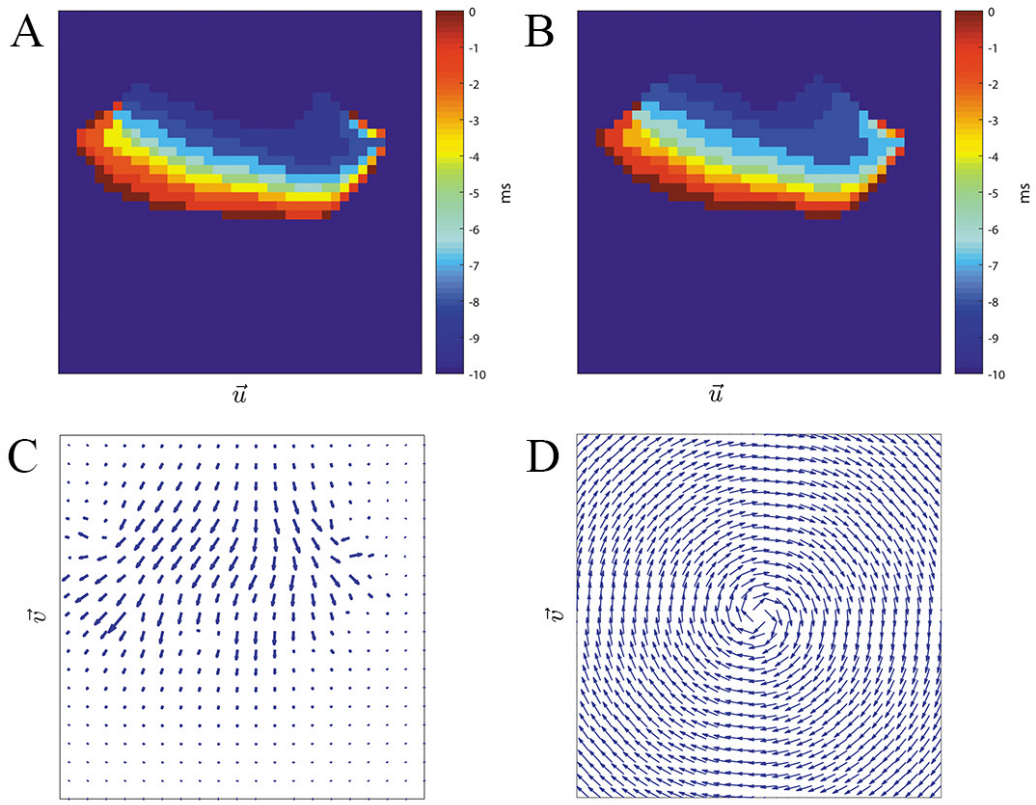

Figure 3.6: Optical flow. Horn-Schunck method on two consecutive images [53]. A: Isochronal frame at $t-1$. B: Isochronal frame at t. C: Velocity vectors applying Horn-Schunck method to the frames. D: Clockwise rotation mask, grid size $J = 32$ nodes.

approaches exist in the literature [43], an early method proposed by Horn and Schunck is used, based on non-parametric motion models and assuming smoothness in the whole image flow [53]. They proposed an energy functional for the flow

$$E(\vec{r}) = \iint ((\nabla I \cdot \vec{r} + I_t)^2 + \lambda(\|\nabla u\|^2) + \|\nabla v\|^2))dxdy. \tag{3.12}$$

The solution to this equation can be iteratively computed for u and v, the two components of the velocity vector $\vec{r}$. It obtains the partial derivatives f_x, f_y, and f_t by 2D-convolution of the images I_t and I_{t-1} with respect to the convolution

kernels K_x, K_y and K_t, namely

$$f_x = I_t * K_x + I_{t-1} * K_x, \tag{3.13}$$

$$f_y = I_t * K_y + I_{t-1} * K_y, \tag{3.14}$$

$$f_t = I_t * K_t - I_{t-1} * K_t, \tag{3.15}$$

where the convolution kernels are

$$K_x = \frac{1}{4}\begin{bmatrix} -1 & 1 \\ -1 & 1 \end{bmatrix}, \tag{3.16}$$

$$K_y = \frac{1}{4}\begin{bmatrix} -1 & -1 \\ 1 & 1 \end{bmatrix}, \text{ and} \tag{3.17}$$

$$K_t = \frac{1}{4}\begin{bmatrix} 1 & 1 \\ 1 & 1 \end{bmatrix}. \tag{3.18}$$

Values u and v are approximated by iteratively calculating N times the solutions for

$$u^n = \bar{u}^n - \frac{f_x[(f_x \cdot \bar{u}^n) + (f_y \cdot \bar{v}^n) + f_t]}{\alpha^2 + f_x^2 + f_y^2}, \tag{3.19}$$

$$v^n = \bar{v}^n - \frac{f_y[(f_x \cdot \bar{u}^n) + (f_y \cdot \bar{v}^n) + f_t]}{\alpha^2 + f_x^2 + f_y^2}, \tag{3.20}$$

for $n = 1, \ldots, N$ and $u^0 = 0$, $v^0 = 0$, where α is the smoothing factor and the local averages $\bar{u}^n$ and $\bar{v}^n$ are calculated as

$$\bar{u}^n = u^{n-1} * \bar{K}, \tag{3.21}$$

$$\bar{v}^n = v^{n-1} * \bar{K}, \tag{3.22}$$

with the averaging kernel

$$\bar{K} = \begin{bmatrix} \frac{1}{12} & \frac{1}{6} & \frac{1}{12} \\ \frac{1}{6} & 0 & \frac{1}{6} \\ \frac{1}{12} & \frac{1}{6} & \frac{1}{12} \end{bmatrix}. \tag{3.23}$$

This method to approximate the integration and derivatives allows a large system of linear equations to be solved by iterative computation. We found $N = 25$ iterations to be enough to approximate the derivatives, since larger values produced

almost identical results. The regularization parameter α provides global smoothing on the grid. For the computations, we selected a value $\alpha = 1$ which makes the propagation of information over far distant points in the image possible.

We apply the HS method to the reconstructed wavefront images at each time instant, obtaining a two element vector $\vec{r}_{j,k} = [u_{j,k}, v_{j,k}]^T$ for each node. Vectors are normalized so $|\vec{r}_{j,k}| = 1$, and $\vec{r}_{j,k} = [0, 0]^T$ if there is no propagation.

We introduce a circular pattern, see Figure 3.6D, consisting of unitary vectors $\vec{c}_{j,k} = [d_{j,k}, e_{j,k}]^T$ arranged in a spiral-like layout satisfying

$$\vec{c}_{j,k} = \begin{cases} d_{j,k} = sin(\alpha_{j,k} + \frac{\pi}{2}), & \text{for} \quad j,k \in [1,J], \\ e_{j,k} = cos(\alpha_{j,k} + \frac{\pi}{2}), & \text{for} \quad j,k \in [1,J], \end{cases} \tag{3.24}$$

where $\alpha_{j,k}$ is the angle defined by each node $n_{j,k}$ and the pattern center located at n_{j^*,k^*} calculated as

$$\alpha_{j,k} = atan2\left(\frac{d(j,j^*)}{dist(k,k^*)}\right), \tag{3.25}$$

where in this case the distance operator $d(A,B)$ (introduced in Eq. 3.9) stands for the euclidean distance between two points A and B.

This layout serves as comparison mask to quantify the rotation level. Vector velocity components of the wavefront and the reference mask are split into matrices $[\mathbf{U}, \mathbf{V}]$ and $[\hat{\mathbf{U}}, \hat{\mathbf{V}}]$ respectively. We apply element-wise scalar product at each time instant n to calculate the rotational intensity, normalized with respect to the number of nodes constituting the J-squared grid, as

$$T[n] \quad = \quad \frac{1}{J^2} \sum_{i=1}^{J} \sum_{j=1}^{J} u_{j,k}[n] d_{j,k}[n] + v_{j,k}[n] e_{j,k}[n]. \tag{3.26}$$

The following step performs time integration of $T[n]$ in a range of γ samples. Only values contained in the time interval $[n-\gamma, n]$ are included to capture the wavefront dynamics, obtaining the expression for our new indicator

$$\Gamma[n] = \sum_{\tau=n-\gamma}^{n} T[\tau]. \tag{3.27}$$

We detect rotational activity when $\Gamma[n]$ exhibits high or low values above or below a double decision threshold $\pm\Gamma_{th}$, see Figure 3.7A-C and Figure 3.8A-C. The sign

determines the circular direction of the wavefront, clockwise or counterclockwise. Depending on the chosen spin turn of the reference mask, i.e., if clockwise, positive $\Gamma[n]$ peaks correspond to clockwise rotations and negative values to counterclockwise gyres.

3.3 Results

3.3.1 Signal Interpolation Results

We used *in silico* signals to validate the wavefront reconstruction. From the 256 pEGM signals, we chose 20 signals according to the spatial position of the PentaRay®electrodes in the grid. We obtained their slope information $\beta[n]$, performed the interpolation and the LATs detection to obtain the reconstructed wavefronts. To evaluate the outcome of the interpolation method, we also processed the whole 256 pEGMs grid to obtain the isochronal propagation so we could compare both interpolations.

We evaluated the interpolation reconstruction for different M, p and σ parameter values. We quantified the interpolation performance by measuring the LATs relative root mean square error (rRMSE) between the interpolated and full grid versions for all the parameter combinations. The rRMSE is defined as:

$$rRMSE = \frac{\sqrt{\frac{1}{N}\sum_{n=1}^{N}\sum_{i=1}^{J}\sum_{j=1}^{J}\left(L_{i,j}[n]-\hat{L}_{i,j}[n]\right)^2}}{\sqrt{\frac{1}{N}\sum_{n=1}^{N}\sum_{i=1}^{J}\sum_{j=1}^{J}\left(L_{i,j}[n]\right)^2}}, \tag{3.28}$$

where $L_{i,j}[n]$ and $\hat{L}_{i,j}[n]$ are the full grid and interpolated LAT signals at node $n_{i,j}$ and time instant $n \in [1, N]$ samples. The $L_{i,j}[n]$ and $\hat{L}_{i,j}[n]$ take value 0 when a LAT is detected and linearly decrease their values until a new activation occurs. We used value ranges $M = 2, 3, 4, \ldots, 20$, $p = 1, 2, 4$ and $\sigma = 0.05, 0.06, \ldots, 0.29, 0.30$.

Best error results were achieved for $p = 4$ in all cases. Figure 3.9 shows the rRMSE values for the M and σ combinations for $p = 4$. For the rotor case (Figure 3.9A) the value minimizing the reconstruction error was $rRMSE = 0.314$

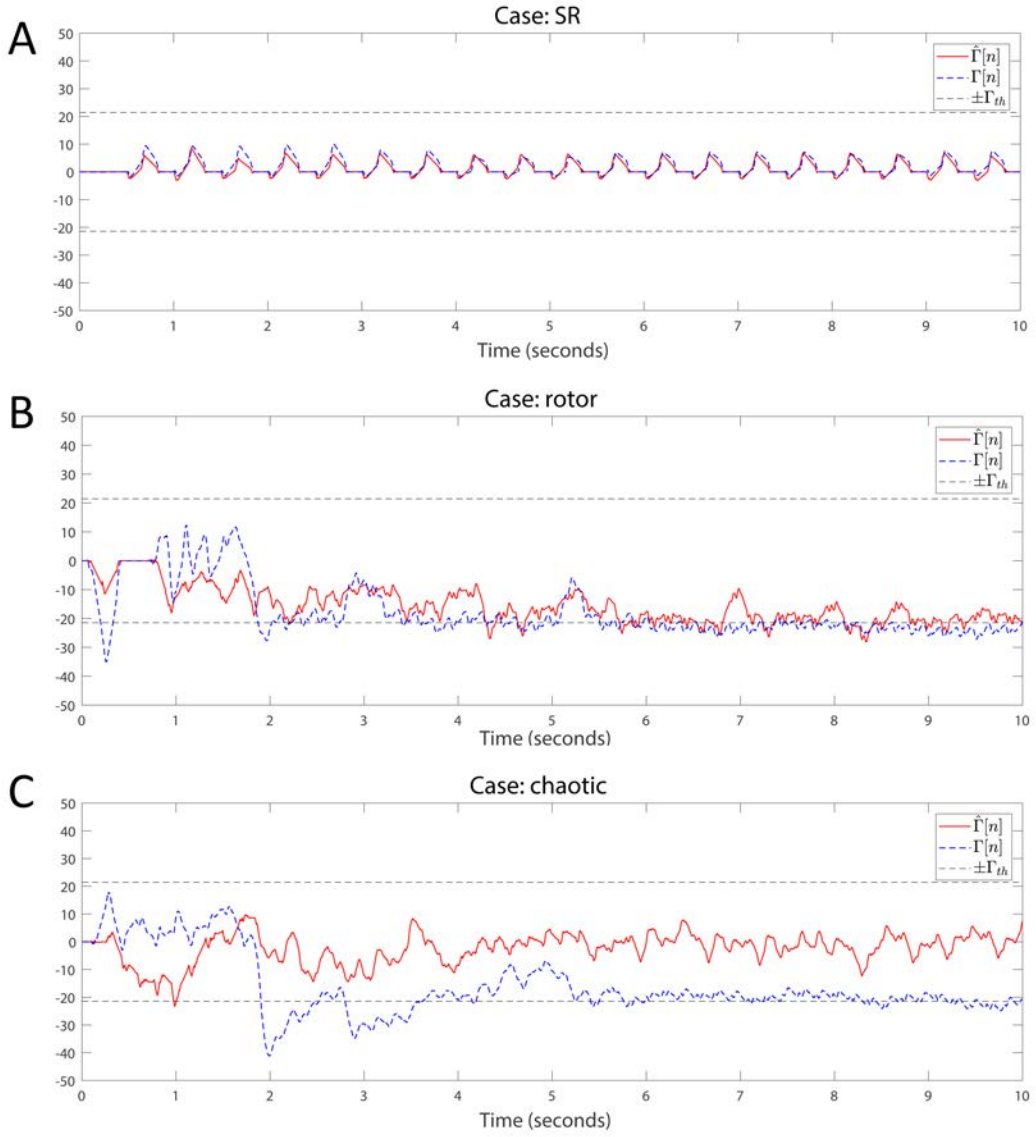

Figure 3.7: Rotational activity detector in *in silico* signals. Detection performed on the three simulation scenarios. The method detects rotational activation if the value of $\Gamma[n]$ exceeds the upper threshold $+\Gamma_{th}$ or falls below the lower threshold $-\Gamma_{th}$. The sign of $\Gamma[n]$ reflects the rotational gyre direction, being positive if the gyre matches the rotation mask spin (clockwise/counterclockwise depending on the chosen pattern), or negative if the propagation rotates in the opposite mask direction. For the simulation cases we applied the detection on the full $\Gamma[n]$ and the interpolated $\hat{\Gamma}[n]$ grids to compare both outcomes. Signals from top to bottom: **A.** Sinus rhythm. **B.** Rotor. **C.** Chaotic wavefront collision. Parameters were $\gamma = 150$ samples and $\Gamma_{th} = \gamma/7$.

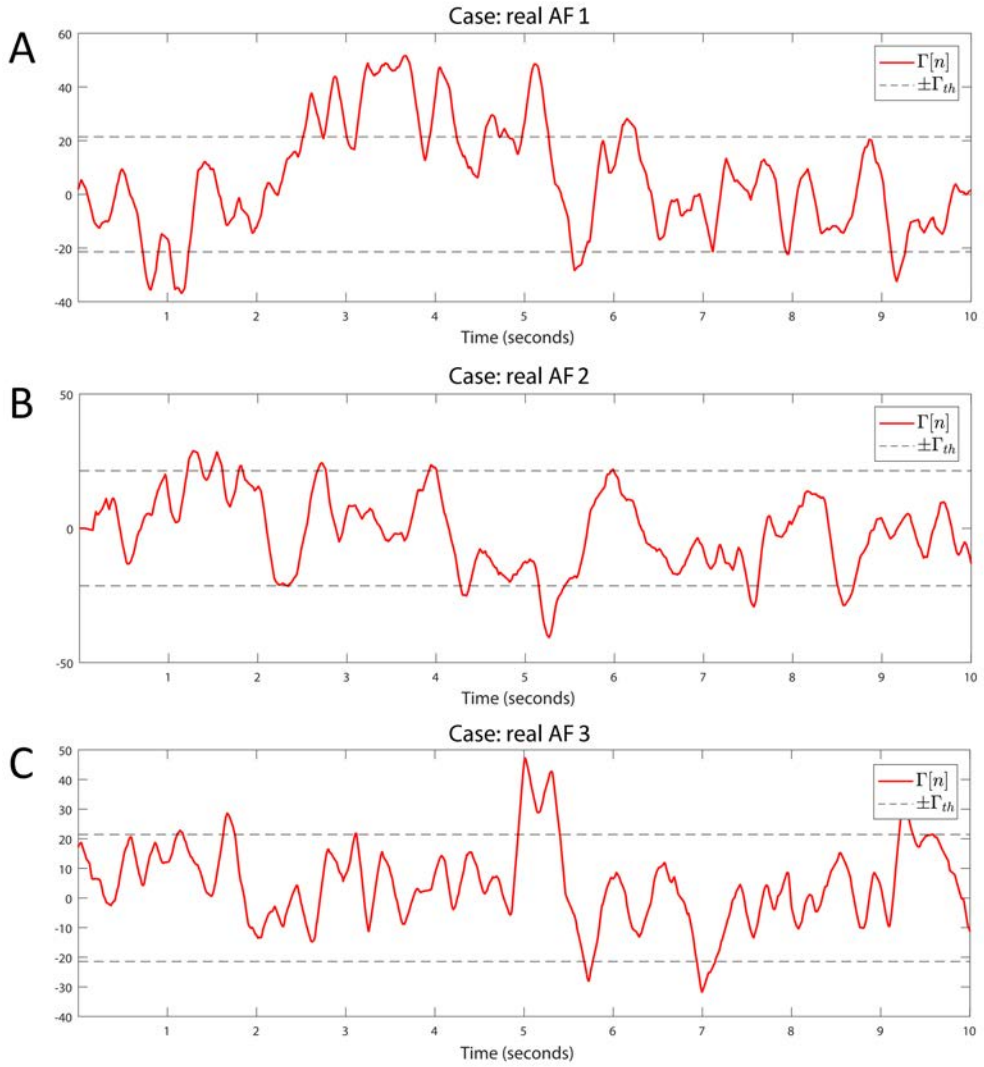

Figure 3.8: Rotational activity detector in real AF signals. Detection performed on the three real AF signals from three different patients. Same methods and parameters are applied as in Figure 3.7. **A.** Sustained multiple rotational activation example. **B.** Non-sustained multiple gyre rotations. **C.** Another example of rotation detection.

(rRMSE mean ± std, 0.348 ± 0.025) achieved for $p = 4$, $M = 20$ and $\sigma = 0.14$. Sinus rhythm (Figure 3.9B) scored $rRMSE = 0.121$ (0.131 ± 0.011) for $p = 4$, $M = 2$ and $\sigma = 0.05$, and the wave collision case (Figure 3.9C) $rRMSE = 0.337$ (0.357 ± 0.019) for $p = 4$, $M = 20$ and $\sigma = 0.12$.

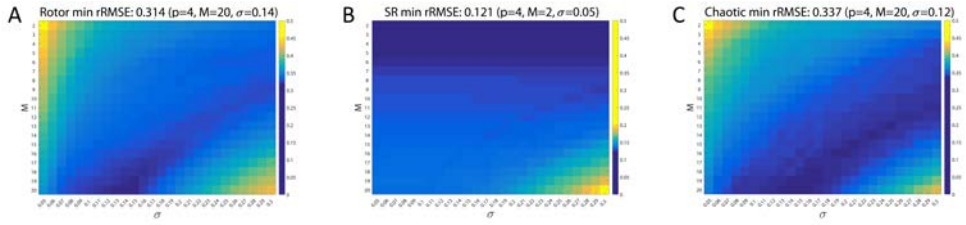

Figure 3.9: Shepard's interpolation method performance. The rRMSE is represented for each case for $p = 4$. **A.** Rotor. $rRMSE = 0.314$ for $p = 4$, $M = 20$ and $\sigma = 0.14$. **B.** Sinus rhythm. $rRMSE = 0.121$ for $p = 4$, $M = 2$ and $\sigma = 0.05$. **C.** Chaotic. $rRMSE = 0.337$ for $p = 4$, $M = 20$ and $\sigma = 0.12$.

The interpolation using Shepard's method was compared against bilinear interpolation. Statistical significance analysis was perform, comparing the rRMSE group means and standard deviations using the Kruskal-Wallist test. Significance was considered for a two-sided p-value (p) of less than 0.01. The minimum rRMSE for rotor case was $rRMSE = 0.328$ (0.375 ± 0.026) for $M = 20$ and $\sigma = 0.14$ (same parameters as the Shepard's approach). The SR case achieved $rRMSE = 0.120$ (0.126 ± 0.012) for $M = 6$ and $\sigma = 0.28$, and the chaotic case $rRMSE = 0.362$ (0.401 ± 0.026) for parameters $M = 16$ and $\sigma = 0.21$. In the rotor and chaotic cases the bilinear interpolation offered significant worse minimum error than the one obtained with the Shepard's interpolation method ($p = 7.6 \times 10^{-59}$ and $p = 4.6 \times 10^{-110}$ respectively). Only in the sinus rhythm case the bilinear interpolation was significantly better than the Shepard's method, $rRMSE = 0.120$ and $rRMSE = 0.121$ respectively ($p = 4.6 \times 10^{-43}$). Since the system is expected to operate when patients are in AF, Shepard's interpolation method provides better performance. We include the Figure 3.10 for the three *in silico* scenarios rRMSE, analogous to Figure 3.9.

We now study the effect on the interpolation performance when a catheter

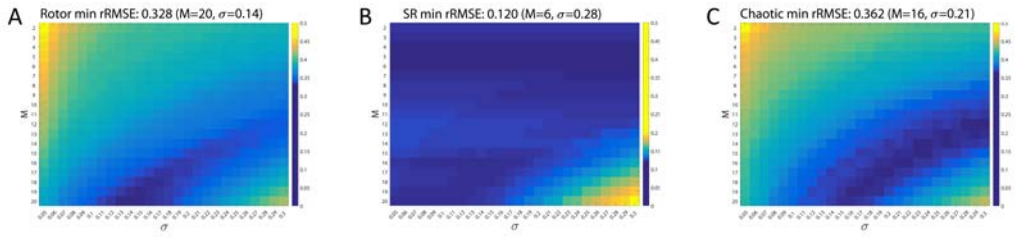

Figure 3.10: Bilinear interpolation method performance. The figure shows the rRMSE for the bilinear interpolation applied to the three *in silico* scenarios, and serves as direct performance comparison to the Shepard's interpolation method in Figure 3.9. **A.** Rotor. $rRMSE = 0.328$ for $M = 20$ and $\sigma = 0.14$. **B.** Sinus rhythm. $rRMSE = 0.120$ for $M = 6$ and $\sigma = 0.28$. **C.** Chaotic. $rRMSE = 0.362$ for $M = 16$ and $\sigma = 0.21$.

branch differs from the fixed position in the grid for the three *in silico* cases. To characterize this behavior, we rotated the positions of one of the branches of the catheter, i.e., the PentaRay®model, from its predefined position. We rotated the 4 electrodes in the branch covering a rotation range $[-\theta, \theta]$, with $\theta = \frac{2\pi}{5}$ radians (or 72°), establishing as rotation limits the angle where the branch overlaps its two neighboring branches. At the rotated electrode positions we took the signals from the full simulated grid and used them to perform the interpolation on the fixed interpolation positions. This way the interpolation maintains the fixed electrode layout but the information signals come from shifted positions emulating the behavior of the catheter when a branch does not match the predefined layout. We iterated in steps of $\frac{\theta}{20}$ and calculated the rRMSE for all the rotated interpolations. We include the results in the Figure 3.11. The figure shows the interpolation rRMSE for the three cases in the $[-\theta, \theta]$ in radians and also with respect the length of the arc of the rotation angle. The arc length is calculated from the circumference of radius 32 mm determined by the most distant PentaRay®electrode with respect to the center of the catheter. The rRMSE remains almost the same for a rotation of $\frac{\pi}{50}$ radians (± 2 mm) and worsens as the rotation angle moves away from the reference fixed position.

The interpolated reconstructions for the parameters minimizing the rRMSE criterion in the three *in silico* cases were presented to the electrophysiologists for

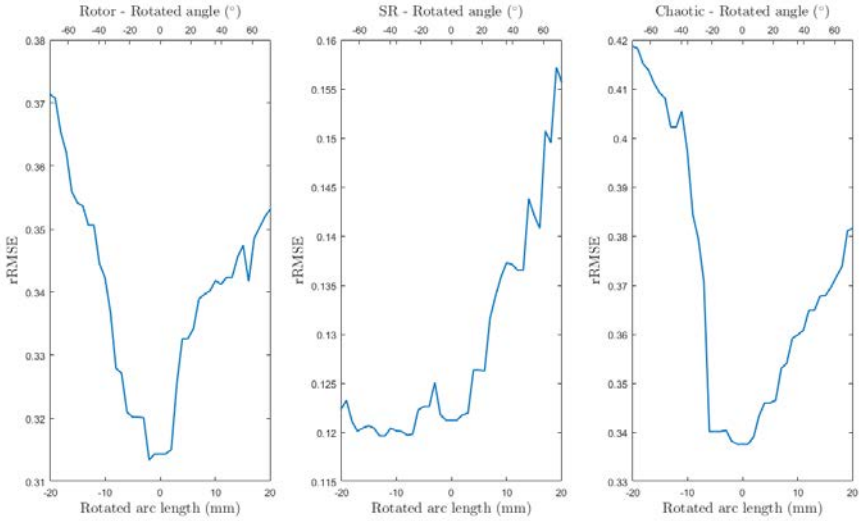

Figure 3.11: Rotated electrode performance. The figure shows the rRMSE when the electrodes in a catheter branch are rotated an angle θ from the predefined interpolation position. The top x-axis covers the $[-\theta, \theta]$ angle range for $\theta = \frac{2\pi}{5}$ radians (or 72°). The bottom x-axis is in linear units and represents the length of the rotated arc of the 32 mm circumference containing the most distal electrode of the PentaRay®catheter. The figure displays the three *in silico* cases: rotor, SR and chaotic wavefronts. The rRMSE error remains almost identical for a shift of ±2 mm.

final validation. They agreed that the sinus rhythm and the rotor cases presented almost identical representation compared to the simulated ground truth. The wave collisions case also exhibited good results in the presence of chaotic behavior. In all the cases the interpolation managed to recover all the activations present in the pEGM grid, and the wavefront morphologies also matched the original ones. This evaluation supports the effectiveness of the proposed interpolation method, and discards any interpolation effect that may introduce uncertainty in the rotational activity detection system.

3.3.2 Rotational Activity Detection Results

The lack of available rotor signals, not even being a consensus about their existence, presents a challenge when evaluating the system's ability to detect rotors. For this reason scientists resort to *in silico* simulated environments to test their

methods. We applied the detection on the three *in silico* scenarios for the full and interpolated grids, with $\gamma = 150$ (150 ms window for $f_s = 1$ KHz), obtaining signals $\Gamma[n]$ and $\hat{\Gamma}[n]$ respectively. As shown in Figure 3.7 A-C, the interpolated and the full versions behave similarly when we capture their dynamics with the rotation mask. We set the same threshold $\Gamma_{th} = \pm\gamma/7$ for the three cases, which succeeded to completely detect the rotor simulation during the whole interval the spiral is active, Figure 3.7B. In the sinus rhythm case, 3.7A, no rotational activity is detected, as expected from its homogeneous propagation. The chaotic wavefront collisions, Figure 3.7C triggers the detector at some points in the full grid $\Gamma[n]$ signal. The randomness of the activation makes the wavefront to partially rotate around the grid center, but since the rotation is not sustained in time nor exhibits a complete turn it does not yield a false detection positive.

The results using the *in silico* simulations allowed us to adjust the system parameters to automatically detect rotational activity in real-time in patients. We acquired signals from 28 AF patients using the PentaRay®catheter mapping different atrial areas per patient. We created a database with more than 600 registers containing EGM and electrocardiogram (ECG) signals. We analyzed the EGMs and reconstructed wavefronts, and conclude that the *in silico* simulations threshold value of $\Gamma_{th} = \gamma/7$ exhibited great detection performance for rotational activity in real AF signals. As detection examples, we include the $\Gamma[n]$ signal of a rotational activation detected in three of the patients, Figure 3.8A-C. We acquired the signal at $f_s = 1$ KHz and used $\gamma = 150$ to match the same integration interval as the computer simulations.

In the first example, Figure 3.8A, $\Gamma[n]$ captures the atrial activity as it performs multiple continuous gyres around the center in the 2-5 seconds interval. The method also captures activations that exhibit single or incomplete gyres. A couple of not maintained rotations are also captured at the beginning and end of the acquisition, 0-1 seconds and 9-10 seconds intervals respectively. This is important since the gyre incompleteness can be related to areas in which the activation experiments a change of direction that may explain AF maintenance, or

can be even related to meandering rotational activation. In the second example, Figure 3.8B, the wavefronts describe a multiple gyre between 1.2-1.8 seconds that evolves into some incomplete gyres, around 4.3, and 8.7 seconds. The incomplete gyre at 4.3 seconds precedes a complete gyre at 5.3 seconds. In the third example, Figure 3.8C, we show another case of multiple gyre detection at the 4.7-5.4 seconds interval which evolves into a incomplete gyre at time instant 5.74 seconds. The activity triggers again the detector at 7 seconds, and again detects a multiple gyre around the end of the acquisition, interval 9.2-9.5 seconds. With these examples we show the capability of the system to detect rotational activation concerning incomplete, complete and multiple gyres. The latter, exceeds the threshold for a more prolonged duration in time, which is useful to differentiate the complexity of the gyre.

Additionally, the method is robust against non-centered rotational activations. We tested the rotational activity detection robustness against non-centered rotational activations. Figure 3.12 shows the scalar product $T[n]$ (Eq.(3.26)) between the reference mask and its shifted version in the $\vec{u}$ and $\vec{v}$ axis, emulating a rotation whose center moves away from the origin. With no shift, the pattern overlaps itself and the scalar product is maximum. If the center of rotation moves further, $\bar{T}$ decreases its value. For a distance of $0.3J$ nodes, the scalar product scores 70% of the centered pattern value, i.e., 10 nodes with $J = 32$ or 19 nodes with $J = 64$, capturing the rotational activity. The approximate J correspondence in mm attaining the PentaRay®catheter coverage when it is fully deployed is 32 mm. That means that for a rotational activity mask shifted $0.3J$ we capture at least 70% of its dynamics at 9.6 mm, which extends the operative physical range of the detector.

3.4 Conclusions

We present a new signal processing method to assess rotational activity in isochronal maps generated from AF EGMs. By analyzing the time domain, our approach opposes the classical detection performed on phase maps, which are known to exhibit

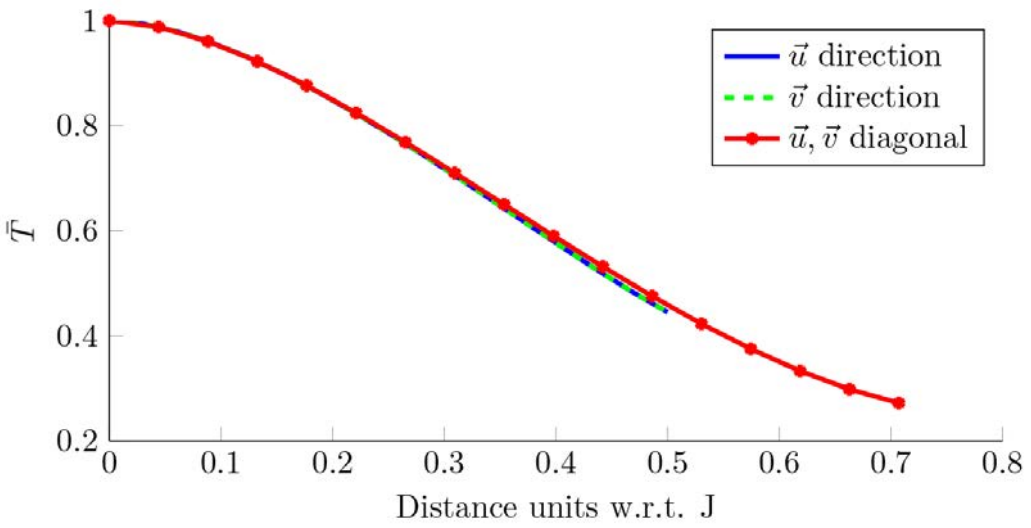

Figure 3.12: Detection robustness. Scalar product for the rotation mask in Figure 3.6D, when it is compared with its shifted version in the $\vec{u}$ axis (blue), $\vec{v}$ axis (green) and the $\vec{u} - \vec{v}$ diagonal (red). The shift is expressed in J units (nodes).

bad correlation with temporal activations. We have validated and analyzed the performance of our methods using both *in silico* and real AF signals, giving additional support to our findings.

In silico simulations need to be part of any new method development, as they provide validation tools, reproducibility and variety in controlled scenarios. The *in silico* signal simulations have been proven useful to validate the interpolation of the signals as prior step to reconstruct the propagation grid. This provided us with a framework to study how the selection of the different parameters affect the signal processing steps. Using a value of σ which is too large prevents the detection of LATs, while a large value of M also limits the LAT detection because the signal is low-pass filtered and attenuated. With the study of different parameter combinations, we reached a compromise between the noise reduction and the LAT detection, which succeeded to minimize the error committed when interpolating the signals.

The unavailability of the electroanatomical 3D system to provide the real-time position of the electrodes forces our method to rely on a fixed layout. This con-

straint requires the electrophysiologist to operate the catheter and align it to the fixed electrode layout. But on the other hand, this ensures the electrode contact against the atrial wall, and helps to better interpret the behavior of local atrial areas complementary to other methods based on basket catheters. We analyzed the effect of a branch drift with respect to the reference layout, concluding that a shift of ± 2 mm produces almost identical results as the correctly placed electrodes, Figure 3.11. We note that some areas of the left atrium cannot be so easily mapped, since deployment of catheters sometimes presents a challenge even for experienced electrophysiologists. But this goes in parallel with basket catheters, whose geometry does not allow to access and map certain areas due to limited coverage and deformations of the catheter. Further studies on tissue characterization could relate atrial areas of restricted access with measurable indices, e.g. bipolar voltage or impedance values.

4

Causality Retrieval in Atrial Fibrillation

4.1 Introduction

Atrial fibrillation (AF) is a cardiac pathology characterized by a rapid and unsynchronized contraction of the atria. The lack of satisfactory performance of RF ablation strategies for some patients is our main motivation. We believe that there is an urgent need of more advanced signal processing and machine learning methods that can assist cardiologists during RF ablation therapies. These techniques should focus on determining the direction of information transfer in the multiple electrograms (EGMs) recorded in the electrophysiology laboratory. This information will help both to better understand the propagation of the action potential (AP) inside the atria of AF patients and to identify candidate sites for radio frequency (RF) ablation. With these goals in mind, Granger causality (G-causality or GC) is a well established methodology to infer causal relations

among multiple time series [24]. Several authors have investigated the inference of causality relationships among different biomedical signals [42, 64]. In particular, causality discovery tools have been extensively used in neurology [24], and Granger's causality (GC) has been used to investigate the relationship between several physiological time series (heart period, arterial pressure and respiration variability) [41, 95]. The use of partial directed coherence to investigate propagation patterns in intra-cardiac signals was considered in [98, 97], whereas GC maps have been built in [106, 109, 107]. However, all of these approaches are based on the standard approach to causality discovery, i.e., computing the pairwise or full-conditional G-causality as described in Section 4.2. More recently, [3] proposed alternative multi-variate causality measures that involve the computation of GC conditioned only on neighbor nodes.

In this chapter, a hierarchical framework for causality retrieval in EGMs is described. The first stage of the proposed methodology consists of finding the EGM having the "strongest" GC links with other EGMs and selecting it as the root node. The remaining nodes are then processed sequentially, starting from the set of candidate children of the root node. Two alternative algorithms are proposed for this purpose: global search causal retrieval (GS-CaRe) and local search causal retrieval (LS-CaRe). GS-CaRe processes the candidate children of the current node sequentially according to their causal strength, accepting them as true children if their GC is statistically significant conditioned on all the previously accepted children. LS-CaRe also processes the candidate children sequentially, but only takes into account the neighbor nodes, thus avoiding many false alarms. An exhaustive evaluation of the proposed algorithms has been performed, using both synthetic signals and annotated real-world signals from AF patients acquired at the electrophysiology laboratory of Hospital General Universitario Gregorio Marañón (HGUGM). Note that the GS-CaRe algorithm was already described in [73, 74]. With respect to [73, 74], a completely novel algorithm (LS-CaRe) is proposed, and an exhaustive set of simulations (using synthetic and real data) are performed to validate both algorithms.

The rest of the chapter is organized as follows. Firstly, Section 4.2 provides an introduction to Granger causality, describing both pairwise and conditional causality. The notation used throughout the text is also summarized here in Table 4.1. Then, Section 4.3 describes the two hierarchical causality discovery algorithms proposed: GS-CaRe and LS-CaRe. This is followed by Section 4.4, where numerical experiments (using both synthetic and real data) are used to validate the developed algorithms. Finally, the chapter is closed in Section 4.5 with a discussion that includes potential future lines.

4.2 Granger Causality

4.2.1 Pairwise Causality

Let us assume that we have N samples of a multi-variate time series composed of Q interrelated signals, $x_q[n]$ for $q = 1,\ \ldots,\ Q$ and $n = 0,\ 1,\ \ldots,\ N-1$. Granger causality measures the increase in predictability on the future outcome of a signal, $x_q[n]$, given the past values of another signal, $x_\ell[n]$ with $\ell \neq q$, with respect to the predictability achieved by taking into account only past values of $x_q[n]$ [24, 48]. In brief, G-causality determines whether past values of $x_\ell[n]$ can be useful to forecast future values of $x_q[n]$ or not.

To provide a rigorous formulation of GC, let us define the linear autoregressive (AR) predictor for $x_q[n]$ given its past samples (i.e., the q-th *self-predictor*) as

$$\hat{x}_q[n] = \hat{x}_{q\to q}[n] = \sum_{m=1}^{M} \alpha_{qq}[m] x_q[n-m] = \boldsymbol{\alpha}_{qq}^\top \vec{x}_q[n], \tag{4.1}$$

where M is the order of the predictor, obtained typically using some penalization for model complexity to avoid overfitting [124]; $\alpha_{qq}[m]$ are the coefficients of the model; $\boldsymbol{\alpha}_{qq} = [\alpha_{qq}[1],\ \ldots,\ \alpha_{qq}[M]]^\top$ and $\boldsymbol{\alpha}_{qq}^\top$ denotes the transpose of $\boldsymbol{\alpha}_{qq}$; and $\vec{x}_q[n] = [x_q[n-1],\ \ldots,\ x_q[n-M]]^\top$. Similarly, let us define the linear autoregressive (AR) predictor for $x_q[n]$ given the past samples of both $x_q[n]$ and $x_\ell[n]$ (i.e., the *cross-predictor* from the ℓ-th signal to the q-th signal) as

$$\hat{x}_{\ell\to q}[n] = \boldsymbol{\alpha}_{qq}^\top \vec{x}_q[n] + \boldsymbol{\alpha}_{\ell q}^\top \vec{x}_\ell[n] = \hat{x}_q[n] + \boldsymbol{\alpha}_{\ell q}^\top \vec{x}_\ell[n], \tag{4.2}$$

Variable	Description
$x_q[n]$	Observed signals ($1 \leq q \leq Q$, $0 \leq n \leq N-1$).
$M_{\ell q}$	Maximum delay in the prediction from the ℓ-th to the q-th signal. Can be user-defined or determined automatically.
$\vec{x}_\ell[n]$	Vector containing all the previous $M_{\ell q}$ samples of $x_\ell[n]$: $\vec{x}_\ell[n] = [x_\ell[n-1],\ \ldots,\ x_\ell[n-M_{\ell q}]]^\top$.
$\alpha_{\ell q}[n]$	Coefficients of the linear predictor from the ℓ-th to the q-th signal.
$\boldsymbol{\alpha}_{\ell q}$	Vector containing all the coefficients of the linear predictor from the ℓ-th to the q-th signal: $\boldsymbol{\alpha}_{\ell q} = [\alpha_{\ell q}[1],\ \ldots,\ \alpha_{\ell q}[M_{\ell q}]]^\top$.
$G_{\ell \to q}$	Pairwise G-causality strength from the ℓ-th signal to the q-th signal.
$\vec{G}$	Pairwise G-causality strength matrix s.t. $\vec{G}_{\ell,q} = G_{\ell \to q}$ for $1 \leq \ell, q \leq Q$.
$C_{\ell q}$	Pairwise G-causality connectivity from the ℓ-th signal to the q-th signal, $C_{\ell q} = \chi_p(G_{\ell \to q})$.
$\vec{C}$	Pairwise G-causality connection matrix s.t. $\vec{C}_{\ell,q} = [\![\chi(G_{\ell \to q}) \geq \gamma_p]\!]$, i.e., $\vec{C}_{\ell,q} = 1$ if $\chi(G_{\ell \to q}) \geq \gamma_p$ and $\vec{C}_{\ell,q} = 0$ otherwise.
γ_p	Threshold used to determine whether a causal link exists or not. It is a function of the user-defined p-value.
$G_{\ell \to q \mid \mathcal{I}}$	Conditional G-causality strength from the ℓ-th signal to the q-th signal given the set of nodes in $\mathcal{I}$.
$\vec{G}_{\mathcal{I}}$	Conditional G-causality strength matrix s.t. $\vec{G}_{\mathcal{I}}(\ell, q) = G_{\ell \to q \mid \mathcal{I}}$.
$C_{\ell \to q \mid \mathcal{I}}$	Conditional G-causality connectivity from the ℓ-th signal to the q-th signal given the set of nodes in $\mathcal{I}$.
$\vec{C}_{\mathcal{I}}$	Conditional G-causality connection matrix s.t. $\vec{C}_{\mathcal{I}}(\ell, q) = [\![\chi\left(G_{\ell \to q \mid \mathcal{I}}\right) \geq \gamma_p]\!]$.
$\mathcal{C}_q = \mathrm{cand}\{i_q\}$	Set of candidate sons of the q-th node ($1 \leq q \leq Q$).
$\mathcal{S}_q = \mathrm{son}\{i_q\}$	Set of sons of the q-th node ($1 \leq q \leq Q$).
$\mathcal{P}_q = \mathrm{pa}\{i_q\}$	Set of parents of the q-th node ($1 \leq q \leq Q$).

Table 4.1: Summary of the main notation used in the definition of the hierarchical Granger causality algorithm.

where $\boldsymbol{\alpha}_{\ell q} = [\alpha_{\ell q}[1],\ \ldots,\ \alpha_{\ell q}[M]]^\top$; $\vec{x}_\ell[n] = [x_\ell[n-1],\ \ldots,\ x_\ell[n-M]]^\top$; and $\hat{x}_q[n]$ is given by (4.1).

The *residual errors* of these two predictors in (4.1) and (4.2) can now be defined as $\varepsilon_q[n] = x_q[n] - \hat{x}_q[n]$ and $\varepsilon_{\ell \to q}[n] = x_q[n] - \hat{x}_{\ell \to q}[n]$, respectively. The *pairwise G-causality* strength is then measured by the logarithm of the ratio of the two

variances of the residuals [44]:

$$G_{\ell \to q} = \ln \frac{\mathrm{Var}(\varepsilon_q[n])}{\mathrm{Var}(\varepsilon_{\ell \to q}[n])}. \tag{4.3}$$

Note that $\mathrm{Var}(\varepsilon_{\ell \to q}[n]) \approx \mathrm{Var}(\varepsilon_q[n])$ when $\vec{x}_\ell[n]$ does not provide any useful information with respect to $x_q[n]$, whereas $\mathrm{Var}(\varepsilon_{\ell \to q}[n]) < \mathrm{Var}(\varepsilon_q[n])$ if $\vec{x}_\ell[n]$ allows us to improve the prediction of $x_q[n]$. Hence, $0 \leq G_{\ell \to q} < \infty$, with larger values of $G_{\ell \to q}$ indicating a stronger evidence of causality from ℓ to q. Using these pairwise values, we can build a *pairwise G-causality strength matrix*, $\vec{G}$, such that its (ℓ, q)-th entry is given by[1]

$$\vec{G}_{\ell,q} = \begin{cases} G_{\ell \to q}, & \ell \neq q; \\ 0, & \ell = q. \end{cases} \tag{4.4}$$

Finally, it is important to remark that we should add a causality link from ℓ to q only when the decrease in the residual's noise variance from (4.1) to (4.2) is statistically significant. In order to construct this causality graph, we define the *pairwise G-causality connection matrix*, $\vec{C}$, whose (ℓ, q)-th element is

$$\vec{C}_{\ell,q} = \begin{cases} 1, & \chi(G_{\ell \to q}) \leq \gamma; \\ 0, & \chi(G_{\ell \to q}) > \gamma, \end{cases} \tag{4.5}$$

where $\chi(G_{\ell \to q})$ denotes some appropriate statistic and γ is the threshold value (i.e., significance level) used to determine whether the value of $G_{\ell \to q}$ is statistically significant. In order to retrieve the potential causality link between two nodes, we resort to p-values, and thus we denote $\gamma = \gamma_p$ [45].[2] The typical values of p in biomedical engineering which will be used here are $p = 0.05$, $p = 0.01$ or $p = 0.001$.

[1] Note that $\mathrm{Var}(\varepsilon_{q \to q}[n]) = \mathrm{Var}(\varepsilon_q[n])$, since $\hat{x}_q[n] = \hat{x}_{q \to q}[n]$, and thus the definition in (4.4) is consistent with (4.3), since $G_{q \to q}[n] = \ln 1 = 0$.

[2] Let us note that some alternative and more complicated approaches than p-values have been proposed in the literature [79]. However, p-values are simple to understand and set by the users, their use is widespread in biomedical applications (as well as in other scientific areas), and they are enough for our purposes. Indeed, we have tested several values of p in the simulations (see Section 4.4), noticing that the value of p has little influence on the results, as long as it is small enough (i.e., $p \leq 0.05$).

Finally, for the sake of simplicity we will use the following short-hand notation for $\vec{C}_{\ell,q}$ in (4.5):

$$\vec{C}_{\ell,q} = [\![\chi(G_{\ell\to q}) \leq \gamma_p]\!], \tag{4.6}$$

where $[\![\mathcal{LC}]\!] = 1$ if the logical condition $\mathcal{LC}$ is true and $[\![\mathcal{LC}]\!] = 0$ otherwise (i.e., if $\mathcal{LC}$ is false), whereas γ_p is the threshold value obtained from the corresponding user-defined p-value.

4.2.2 Conditional Causality

Unfortunately, pairwise GC is unable to discriminate between *direct causation* (e.g. $x_1[n] \to x_3[n]$) and *indirect causation* (e.g. $x_1[n] \to x_2[n] \to x_3[n]$). In both cases, the pairwise G-causality approach would lead to $\vec{C}_{1,3} = 1$, implying that $x_1[n]$ has caused $x_3[n]$. However, when building the *causality network* we are only interested in direct causes, since all the spurious links created by indirect causes may obscure the flow of information among signals. In order to avoid these undesired links returned by pairwise causality, *conditional G-causality* was introduced in [44]. In short, conditional GC attempts to determine whether $x_\ell[n]$ has caused $x_q[n]$ given another set of intermediate signals.

In order to provide a precise mathematical definition of conditional GC, let us define the set containing the indexes of the conditioning variables as $\mathcal{I}$. Following a similar procedure as before, we define the *conditional self-predictor*

$$\hat{x}_{q|\mathcal{I}}[n] = \boldsymbol{\alpha}_{qq}^\top \vec{x}_q[n] + \sum_{r\in\mathcal{I}} \boldsymbol{\alpha}_{rq}^\top \vec{x}_r[n], \tag{4.7}$$

where $\boldsymbol{\alpha}_{rq} = [\alpha_{rq}[1],\ \ldots,\ \alpha_{rq}[M]]^\top$ and $\vec{x}_r[n] = [x_r[n-1],\ \ldots,\ x_r[n-M]]^\top$ for all $r \in \mathcal{I}$, and the *conditional cross-predictor* from the ℓ-th signal (with $\ell \notin \mathcal{I}$) to the q-th output

$$\begin{aligned}\hat{x}_{\ell\to q|\mathcal{I}}[n] =& \boldsymbol{\alpha}_{qq}^\top \vec{x}_q[n] + \sum_{r\in\mathcal{I}} \boldsymbol{\alpha}_{rq}^\top \vec{x}_r[n] + \boldsymbol{\alpha}_{\ell q}^\top \vec{x}_\ell[n] \\ =& \hat{x}_{q|\mathcal{I}}[n] + \boldsymbol{\alpha}_{\ell q}^\top \vec{x}_\ell[n].\end{aligned} \tag{4.8}$$

Now, by defining the residual errors from the conditional predictors as $\varepsilon_{q|\mathcal{I}}[n] = x_q[n] - \hat{x}_{q|\mathcal{I}}[n]$ and $\varepsilon_{\ell\to q|\mathcal{I}}[n] = x_q[n] - \hat{x}_{\ell\to q|\mathcal{I}}[n]$, the conditional G-causality

strength can be defined, in a similar way to (4.3), as

$$G_{\ell\to q|\mathcal{I}} = \ln \frac{\mathrm{Var}(\varepsilon_{q|\mathcal{I}}[n])}{\mathrm{Var}(\varepsilon_{\ell\to q|\mathcal{I}}[n])}. \tag{4.9}$$

Again, $0 \leq G_{\ell\to q|\mathcal{I}} < \infty$, with larger values of $G_{\ell\to q|\mathcal{I}}$ indicating a stronger evidence of causality from ℓ to q given the set of signals in $\mathcal{I}$; and we define two conditional connection/strength GC matrices, $\vec{G}_{\mathcal{I}}$ and $\vec{C}_{\mathcal{I}}$, whose (ℓ, q)-th elements are, respectively, $\vec{G}_{\ell,q|\mathcal{I}} = G_{\ell\to q|\mathcal{I}}$ and $\vec{C}_{\ell,q|\mathcal{I}} = [\![\chi(G_{\ell\to q|\mathcal{I}}) \leq \gamma_p]\!]$.

Note that the pairwise GC connection/strength matrices are unique, whereas many conditional GC connection/strength matrices can be constructed. The most usual situation is setting $\mathcal{I} = \mathcal{S}_{\neg\ell} = \{1,\ \ldots,\ \ell-1,\ \ell+1,\ \ldots,\ Q\} = \{1,\ \ldots,\ Q\} \setminus \{\ell\}$ and constructing the *full conditional* GC connection/strength matrices as $\vec{G}_{\ell,q|\mathcal{S}_{\neg\ell}} = G_{\ell\to q|\mathcal{S}_{\neg\ell}}$ and $\vec{C}_{\ell,q|\mathcal{S}_{\neg\ell}} = [\![\chi(G_{\ell\to q|\mathcal{S}_{\neg\ell}}) \leq \gamma_p]\!]$, respectively. However, conditional causality can also be used to build hierarchical models by conditioning on specific sets of nodes in a structured way, as described in Section 4.3.

4.3 Hierarchical Granger Causality for Intracavitary Electrograms

On the one hand, pairwise GC may provide misleading results, as discussed in Section 4.2.1. On the other hand, the "brute-force approach" to conditional causality (i.e., applying conditional causality on the whole data set all at once) may obscure some of the existing relationships. Let us consider again the three-node causal network $x_1[n] \to x_2[n] \to x_3[n]$. Now, by applying the full-conditional GC approach we would typically obtain a single dependence relation: $G_{1\to 2|3} = 1$. The other desired link, $x_2 \to x_3$, would typically not be included, since $G_{2\to 3|1} = 0$ unless a very short lag (M) is used to ensure that only signals from neighbor nodes are taken into account (i.e., that the contribution of $x_1[n-1], \ldots, x_1[n-M]$ to the prediction of $x_3[n]$ is negligible).

Under these circumstances, we propose two hierarchical methods that are able to exploit the advantages of both approaches while minimizing their drawbacks.

Both algorithms start by searching for the node with the "strongest" G-causality links with the remaining nodes and selecting it as the root node.[3] Then, the children of the root node are processed, adding new causality links if the corresponding causality test is passed. This process is repeated iteratively until there are no more nodes to process and a *poly-tree* has been constructed. The assumed premises are the following:

1. No feedback links can exist from lower nodes to higher nodes in the hierarchy. This restriction is a consequence of the *refractory period* of the AP: a period of time following the excited phase when additional stimuli evoke no substantial response [61].[4]

2. Causal interactions typically occur between neighbor nodes. This behavior is due to the continuous propagation of the waveform through the cardiac tissue.

In the sequel, we first describe the common initial step (i.e., the selection of the root node) and then we detail the two hierarchical causality algorithms proposed: GS-CaRe and LS-CaRe.

[3]Note that the proposed framework essentially tries to identify the propagation direction of the action potential (AP). In order to do so, we propose a hierarchical approach based on Granger causality (although other causality measures could also be used) to measure the direction of the transfer of information throughout the available electrodes. In this setting, the root node becomes the entry point of the waveform to the set of electrodes, and thus it is essential to determine the desired propagation direction.

[4]Note that this assumption holds regardless of the type of catheter used, as long as the measurements taken by this catheter are all concentrated in a certain area of the atria (i.e., it may not hold for basket catheters that try to cover the whole atrium). The only exception for the circular catheter used in the experiments (see Section 4.4) concerns the initial and final points in the hierarchy when we have circular dependencies like the ones shown in Figures 4.3(p), (n) and (o). In this case our algorithm is unable to discover this last connection, and thus would always have at least one missing link.

4.3.1 Initialization: Selecting the Root Node

The initialization stage, which is common for both the GS-CaRe and the LS-CaRe algorithms, seeks to find the optimal root node for the causal graph. This is done by computing the pairwise GC among all nodes and selecting the one with the "strongest" causal connections to other nodes. More precisely, the steps performed to select the root node are the following:

1. Compute $G_{q\to\ell}$ and $G_{\ell\to q}$ (for $\ell, q = 1,\ \ldots,\ Q-1$), and set the corresponding entries in $\vec{G}$ and $\vec{C}$.

2. Calculate the GC strength of the q-th node ($q = 1,\ \ldots,\ Q-1$) as the sum of the strength of its causal links to the remaining nodes:

$$g_q = \sum_{\ell=1}^{Q} \vec{G}_{q,\ell} = \sum_{\ell=1}^{Q} G_{q\to\ell}. \tag{4.10}$$

   Calculate also the number of links for each node as

$$K_q = \sum_{\ell=1}^{Q} \vec{C}_{q,\ell} = \sum_{\ell=1}^{Q} [\![\chi(G_{q\to\ell}) \leq \gamma_p]\!]. \tag{4.11}$$

3. Determine the node with the largest number of outgoing causal links (i.e., links from that source node to some other sink node), selecting it as the root node:[5]

$$i_1 = \arg\max 1 \leq q \leq Q\ K_q, \tag{4.12}$$

   with g_q being used only to discriminate among nodes with identical values of K_q.

4.3.2 Global Search Hierarchical Algorithm (GS-CaRe)

The GS-CaRe algorithm was initially proposed in [73] and later on refined in [74]. Figure 4.1 shows the flow diagram of the GS-CaRe algorithm. After the selection

[5] In [73], the root node was obtained by maximizing g_q instead of K_q, but we have observed that this can lead to an erroneous selection of the root node when a single very strong causal connection (i.e., a single very large value of $\vec{G}$) dominates over the rest.

of the root node, as described in Section 4.3.1, GS-CaRe sets the root node as the current node and processes this current node (e.g. node i) recursively as shown in Figure 4.1:

- Finds the candidate children of the current node, $\mathcal{C}_i = \text{cand}\{i\} = \{\ell : \vec{C}_{i,\ell} = 1\}$, using pairwise GC.[6]
- Sorts the candidate children according to their pairwise GC strength, in such a way that $G_{i\to\mathcal{C}_i(1)} \geq G_{i\to\mathcal{C}_i(2)} \geq G_{i\to\mathcal{C}_i(3)} \geq \cdots$
- Finds the true children sequentially using conditional GC, starting with the "strongest" candidate and conditioning on all the previously accepted true children.

If the current node has some true children, the strongest one is selected as the current node, removed from the true children list and the aforementioned process is repeated again. It the current node does not have any true children (either because they have already been processed or because the end of the causality chain has been reached), then the parent of the current node is set as the current node and the process is repeated again. The algorithm ends when the current node is again the root node and does not have true children to process anymore. At the end of this process, GS-CaRe returns the strength/connection GC matrices, $\vec{G}$ and $\vec{C}$, which define a poly-tree with its children and parents.

4.3.3 Local Search Hierarchical Algorithm (LS-CaRe)

Figure 4.2 shows the flow diagram of the LS-CaRe algorithm. LS-CaRe processes the nodes directly according to their causal strength (starting from the root node, which is the "strongest" one), considering only causal links among neighbors up to a maximum user-defined distance, $d_{\max}$. First of all, let us define the distance among nodes as

$$d(\ell, q) = \min\{((\ell - q))_Q, ((q - \ell))_Q\}, \tag{4.13}$$

[6]Note that the search for candidate children is only performed on the currently unprocessed nodes. See [73] or [74] for further details.

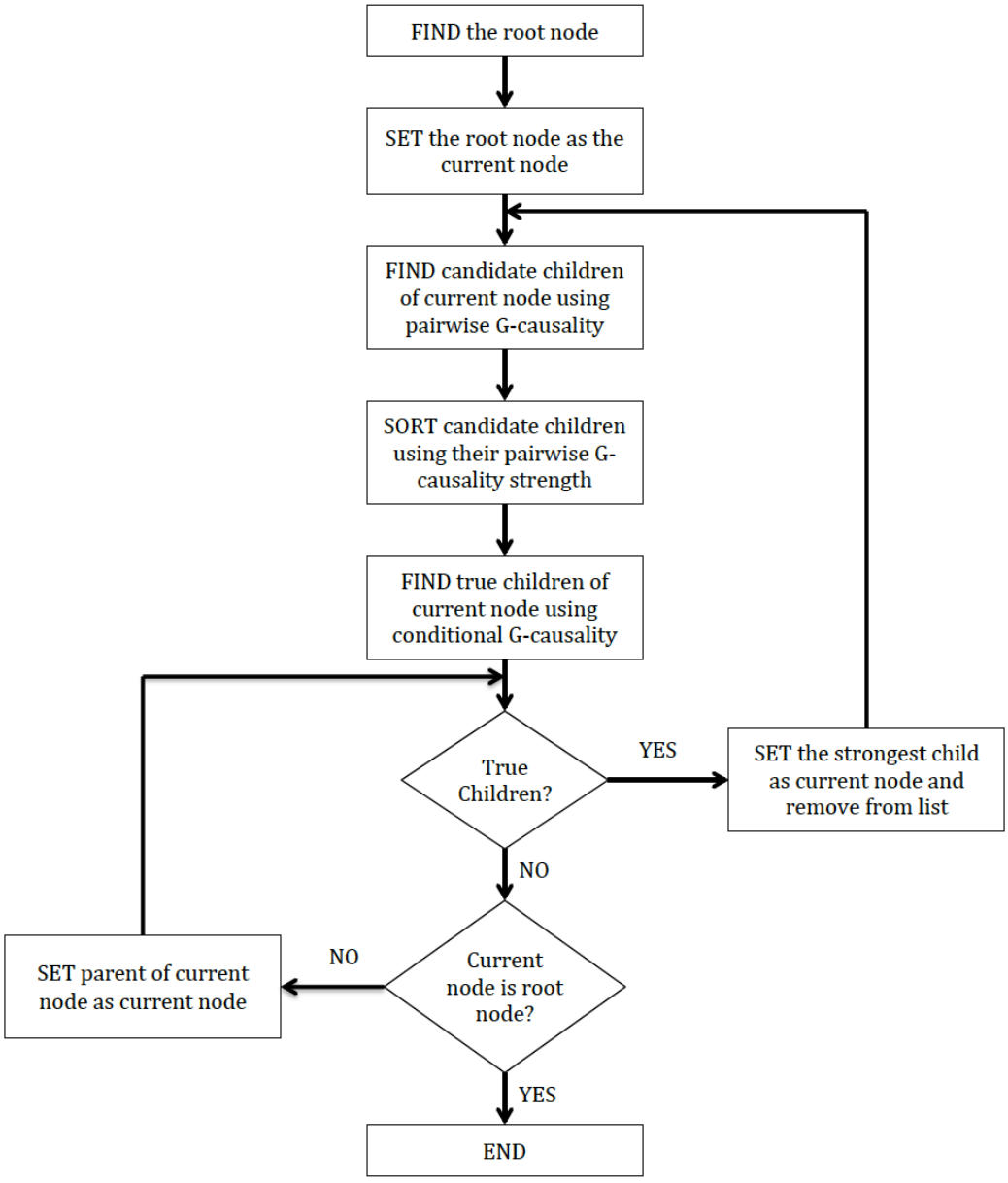

Figure 4.1: Flow diagram of the GS-CaRe algorithm.

for any $\ell, q \in \{1, 2, \ldots, Q\}$ and with $((\cdot))_Q$ denoting the modulo operation, i.e., for any three integer numbers m, k and Q, $m = ((k))_Q \Leftrightarrow k = rQ + m$, where r and m are the only integers such that $-\infty < r < \infty$ and $0 \leq m \leq Q - 1$. Then, using the K_q computed in Section 4.3.1, construct an ordered set of nodes,

$\mathcal{I} = \{i_1, i_2, \ldots, i_Q\}$ with i_1 being the root node, such that $K_\ell \geq K_q$ for all $\ell < q$.[7] Initialize the set of neighbors of each node by including only the own nodes (i.e., $\mathcal{N}_q^{(0)} = \{q\}$ for $q = 1, \ldots, Q$). Set $q = 1$ and $d = 1$. Now, the LS-CaRe algorithm proceeds in the following way:

1. Update the set of neighbors by including those neighbors at distance d from i_q, i.e., set $\mathcal{N}_q^{(d)} = \mathcal{N}_q^{(d)} \cup \mathcal{L}_q^{(d)}$ with

$$\mathcal{L}_q^{(d)} = \{\ell : d(i_q, \ell) = d,\ \ell = 1, \ldots, Q\}. \tag{4.14}$$

   Hence, $\mathcal{N}_q^{(d)}$ includes now all those nodes whose distance to node i_q is lower or equal than d.

2. For any node $\ell \in \mathcal{L}_q^{(d)}$, add an edge from i_q to ℓ if $C_{i_q \to \ell} = 1$ and the following two conditions are fulfilled:

   (a) There is no connection from any of the neighbors in $\mathcal{N}_q^{(d-1)}$ to/from i_q. Mathematically, defining

$$\mathcal{E}_q^{(d)} = \sum_{\ell \in \mathcal{N}_q^{(d-1)}} \left(C_{\ell \to i_q} + C_{i_q \to \ell}\right), \tag{4.15}$$

   an edge can only be added if $\mathcal{E}_q^{(d)} = 0$. This condition implies that edges should not be added to nodes far away if connections to closer nodes already exist.

   (b) The ℓ-th node is not already connected, i.e., $\sum_{j=1}^{Q} C_{j \to \ell} = 0$ or $\sum_{j=1}^{Q} C_{\ell \to j} = 0$.

3. If $q < Q$, then set $q = q + 1$ and return to step 1. Otherwise, set $q = 1$ and check d. If $d < d_{\max}$, set $d = d + 1$ and return to step 1.

At the end of this process, GS-CaRe returns again the strength/connection GC matrices, $\vec{G}$ and $\vec{C}$, for the whole set of nodes.

[7] As indicated in Section 4.3.1, when $K_\ell = K_q$ for two nodes ℓ and q, we use g_ℓ and g_q to break the tie.

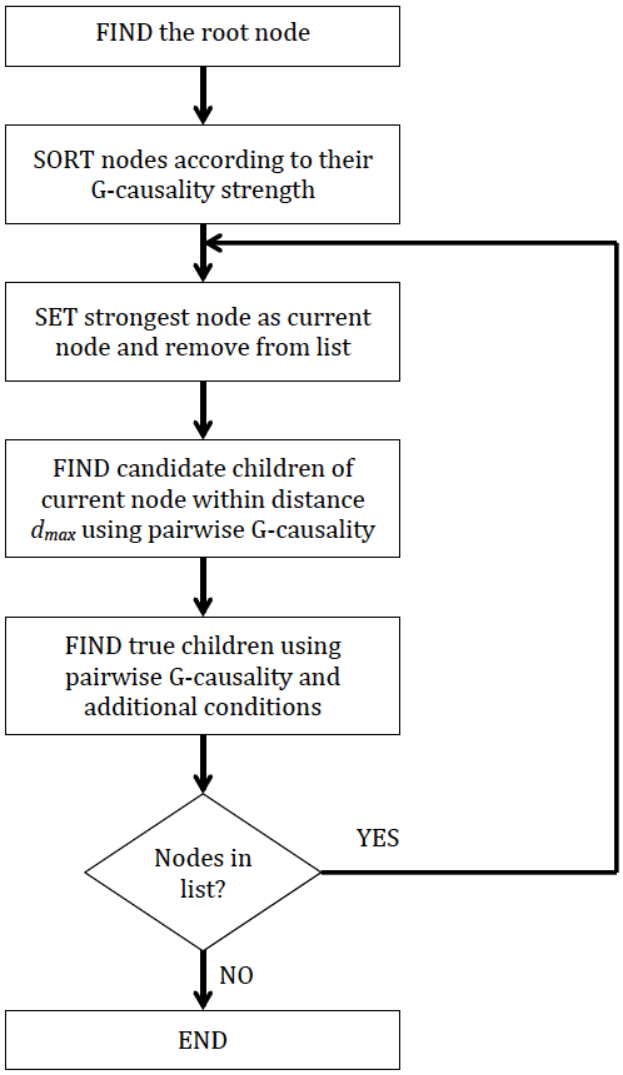

Figure 4.2: Flow diagram of the LS-CaRe algorithm.

4.4 Numerical Experiments

In this section, we first define the performance measures that will be used in Section 4.4.1. Then, we describe the numerical experiments performed using synthetic data in Sections 4.4.2 and 4.4.3. Finally, the validation using annotated real data is provided in Section 4.4.4. In order to implement the four algorithms tested in this section (GS-CaRe, LS-CaRe, the pairwise approach and the full-conditional method), we have used the Granger causal connectivity (GCCA) toolbox [118].

4.4.1 Methods and Performance Measures

In order to gauge the performance of the two novel hierarchical algorithms (LS-CaRe and GS-CaRe), we compare them against the following methods:

- **Pair:** pairwise causality discovery approach, which simply performs a pairwise causality check among all nodes.
- **Full:** full-conditional causality discovery technique, which performs a causality check among pairs of nodes conditioned on all the other nodes.
- **Alcaine et al.:** the approach proposed in [3], which defines a local propagation direction measure based on conditional causality relations among four adjacent nodes.

For this comparison we use several standard statistical performance measures. Let us denote the true causal connection from the ℓ-th to the q-th EGM (with $\ell \neq q$) as $\vec{C}_{\ell,q}$,[8] and the estimated one as $\widehat{\vec{C}}_{\ell,q}$. Noting that our main goal is discovering the causal links among the different EGMs, we can have the following situations:

- **True positive (TP):** The correct detection of an existing causal link, i.e., $\vec{C}_{\ell,q} = \widehat{\vec{C}}_{\ell,q} = 1$.
- **False negative (FN):** The failure to detect an existing causal link, i.e., $\vec{C}_{\ell,q} = 1$ and $\widehat{\vec{C}}_{\ell,q} = 0$.
- **True negative (TN):** The correct absence of a non-existing causal link, i.e., $\vec{C}_{\ell,q} = \widehat{\vec{C}}_{\ell,q} = 0$.
- **False positive (FP):** The detection of a causal link when no causal link truly exists, i.e., $\vec{C}_{\ell,q} = 0$ and $\widehat{\vec{C}}_{\ell,q} = 1$.

Let us denote the total number of positive cases (i.e., *true* causal links) as P, the total number of negative cases (i.e., non-existing or *false* causal links) as F, and

[8] Remember that $\vec{C}_{\ell,q} = 1$ corresponds to the presence of a causal link and $\vec{C}_{\ell,q} = 0$ corresponds to the absence of that causal link.

the total number of possible connections as $T = Q(Q-1)$. Now, we can define the following performance measures:[9]

- **Sensitivity:** Also known as True Positive Rate (TPR). Measures the proportion of causal links that are correctly identified out of the total number of causal links:
$$\mathrm{TPR} = \frac{\mathrm{TP}}{\mathrm{P}} = \frac{\mathrm{TP}}{\mathrm{TP}+\mathrm{FN}}. \tag{4.16}$$
- **Specificity:** Also known as True Negative Rate (TNR). Measures the proportion of non-existing causal links that are correctly identified:
$$\mathrm{TNR} = \frac{\mathrm{TN}}{\mathrm{F}} = \frac{\mathrm{TN}}{\mathrm{TN}+\mathrm{FP}}. \tag{4.17}$$
- **Accuracy:** Measures the proportion of true causal detections (both for existing and non-existing links) among the total number of possible connections:
$$\mathrm{Acc} = \frac{\mathrm{TP}+\mathrm{TN}}{\mathrm{T}} = \frac{\mathrm{TP}+\mathrm{TN}}{\mathrm{TP}+\mathrm{FP}+\mathrm{TN}+\mathrm{FN}}. \tag{4.18}$$
- **F-Score:** Also known as F_1 score. An alternative global measure of performance, obtained as the harmonic mean of sensitivity and precision (also known as Positive Predictive Value (PPV), and defined as $\mathrm{PPV} = \mathrm{TP}/(\mathrm{TP}+\mathrm{FP})$):
$$F_1 = \frac{\mathrm{PPV}\times\mathrm{TPR}}{\mathrm{PPV}+\mathrm{TPR}} = \frac{2\mathrm{TP}}{2\mathrm{TP}+\mathrm{FP}+\mathrm{FN}}. \tag{4.19}$$

Altogether, these complementary measures provide a complete characterization of the performance of the different algorithms. On the one hand, a high sensitivity implies a low rate of false negatives, indicating that the method is unlikely to miss existing causal links (i.e., all the true causal relations in the data are likely to be discovered). On the other hand, a high specificity is related to a low level of false positives, meaning that the algorithm is unlikely to introduce spurious causal links (i.e., all the causal links introduced are likely to correspond to true links). Finally, the accuracy and the F-Score provide a single global performance measure that takes into account both the false positives and the false negatives.

[9]Note that the range for all the performance measures is from 0 to 1, with 1 indicating the best possible result and 0 indicating the worst one.

4.4.2 Simple Synthetic Intracardiac Electrograms

In this section, we test the performance of the two algorithms proposed (LS-CaRe and GS-CaRe) on simple synthetic EGMs. In order to generate these signals, the network of modified stochastic FitzHugh-Nagumo (FH-N) oscillators described in [32, 75] has been used as *in silico* model. FH-N oscillator networks are a simple, well-known and widely used model for waveform propagation in excitable media [61]. In cardiology, the FH-N equations can be used to replicate the AP of the sinoatrial node, and the FH-N dynamics has also been applied in the study of cellular coupling or the mechanism of defibrillation [62]. Regarding the analysis of AF, this model does not generate realistic EGMs in the time domain, but it is able to reproduce the propagation patterns observed in real patients. Therefore, we believe that it is a useful model to perform an initial validation of the proposed methods.

In Appendix B we include the description of the FH-N model equations and the simulation setup. Using this model, we have generated a database composed of 17 sets of synthetic multi-variate EGMs that mimic AP wavefront propagation patterns observed in real signals. Rotors are generated by applying a forcing signal at one node right after the wavefront has passed through it. Then, we select 10 nodes from the 2D grid according to a circular layout resembling the topology of a 10-pole spiral catheter. With the virtual recording electrodes placed at these locations, the 9 synthetic bipolar EGMs used in the simulations are obtained. Figure 4.3 shows the different propagation patterns (see also the accompanying videos in the supplementary material in [75]), grouped into three categories:

- **Single**, corresponding to the AP wavefront propagation pattern observed when a single-loop rotor is present.
- **Flat**, associated to a flat propagation pattern (as observed when the catheter is placed far away from the focal source) plus a double-loop rotor (except in the first case).
- **Circular**, where a circular propagation pattern (corresponding to the catheter

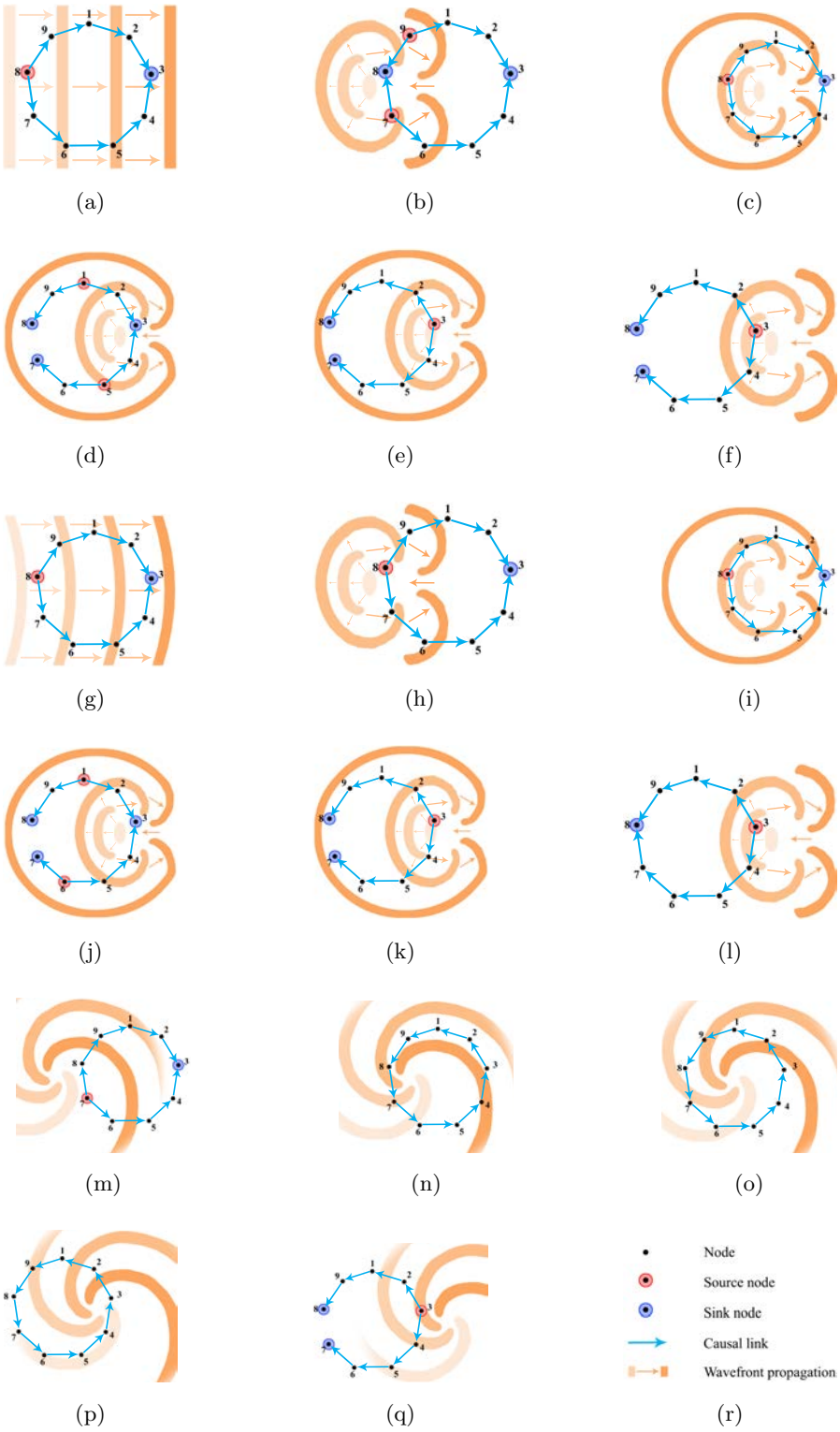

Figure 4.3: Different propagation patterns generated by the synthetic signal simulator. **(a)–(f):** Flat 1–6. **(g)–(l):** Circular 1–6. **(m)–(q):** Single 1–5. **(r):** Legend.

being placed close to the focal source) plus a double-loop rotor (once more, in all cases except for the first one) is observed.

The following information is shown in Figure 4.3:

- **Wavefront propagation:** Orange swirls of different intensities to show the local propagation pattern and direction of the electrical wavefront.
- **Nodes:** The locations of the nodes of the virtual recording device. Red and blue circles are used to denote source and sink nodes, respectively.
- The true causal links (blue lines and arrows) among the synthetic EGMs.

Figure 4.4 shows an example of the noiseless synthetic signals for three cases (single 1, flat 2 and circular 4), altogether with the intensity plots (using black squares for the ones and white squares for the zeros) of their true causality matrices. In the first experiment, we analyze the performance of the different methods (in terms of the F-score) as a function of the two parameters of the model: the p-value and the lag (M). Tables 4.2 and 4.3 show the results. On the one hand, in Table 4.2 it can be seen that the results are rather stable with respect to the p-value, with slight decreases in performance for all the methods at low signal to noise ratios (SNRs) and small increases at large SNRs. On the other hand, from Table 4.3 we notice that a similar situation occurs (except for the full-conditional approach) for M. Therefore, instead of selecting specific values of p and M for the subsequent simulations, we present the results averaged over all the considered significance levels ($p \in \{0.05, 0.01, 0.001, 0.0001\}$) and orders of the AR models ($M \in \{10, 15, 20, 25, 30\}$).

Figures 4.5(a)–(c) show the averaged sensitivity (TPR), specificity (TNR) and F-score for the different methods tested. Alcaine's approach attains the best performance in terms of TPR and F-score (followed closely by LS-CaRe in both cases), whereas LS-CaRe attains the best TNR (with Alcaine's method performing slightly worse). The pairwise approach achieves good TPR values, but its performance is very poor in terms of TNR. On the contrary, the full-conditional and GS-CaRe techniques obtain good TNR values, but very poor TPRs. The F-score for these

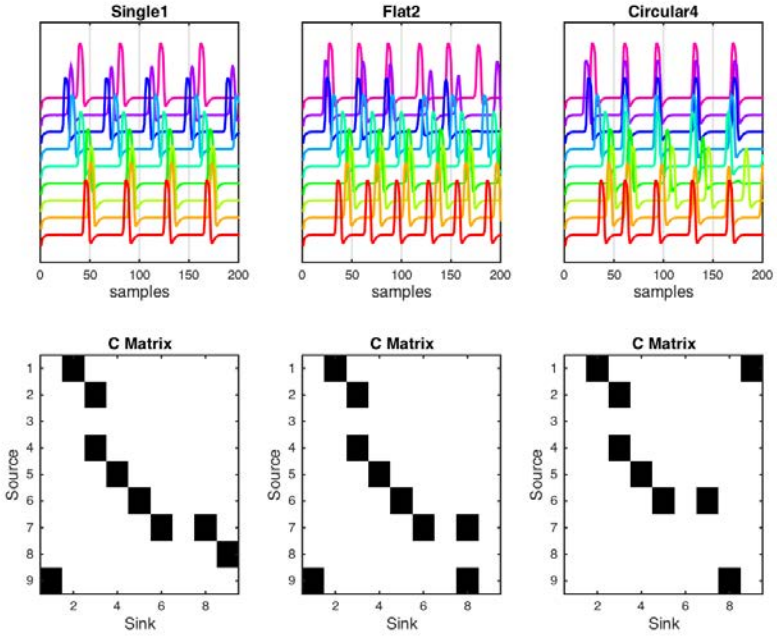

Figure 4.4: **Top.** Example of the nine synthetic signals (ordered from bottom to top as $1 \rightarrow 9$) generated for three different cases: Single 1, Flat 2, and Circular 4. **Bottom.** Binary intensity plots of the true causality matrices $\vec{C}$. A black square corresponds to $\vec{C}_{\ell,q} = 1$, whereas a white square means $\vec{C}_{\ell,q} = 0$.

Method	p**-value (SNR = 10 dB)**			
	0.05	0.01	0.001	0.0001
Full	0.3891	0.3768	0.3022	0.2373
Pair	0.4724	0.4908	0.4773	0.4522
GS-CaRe	0.3357	0.3391	0.3178	0.2866
LS-CaRe($d_{\max} = 1$)	0.8505	0.8237	0.7628	0.7004
LS-CaRe($d_{\max} = 2$)	0.8488	0.8268	0.7702	0.7137
LS-CaRe($d_{\max} = 3$)	**0.8525**	**0.8301**	**0.7842**	0.7334
Alcaine et al. [3]	0.7742	0.7829	0.7745	**0.7767**
Method	p**-value (SNR = 40 dB)**			
	0.05	0.01	0.001	0.0001
Full	0.4184	0.4551	0.4726	0.4691
Pair	0.4340	0.4620	0.4838	0.4791
GS-CaRe	0.3075	0.3328	0.3290	0.3584
LS-CaRe($d_{\max} = 1$)	0.7820	0.8272	0.8386	0.8111
LS-CaRe($d_{\max} = 2$)	0.7808	0.8301	0.8355	0.8152
LS-CaRe($d_{\max} = 3$)	0.7822	0.8287	0.8424	0.8268
Alcaine et al. [3]	**0.8756**	**0.8805**	**0.8801**	**0.8805**

Table 4.2: F-Score for the different methods tested as a function of the p-value used for $M = 10$ and two values of SNR.

Method	M **(SNR = 10 dB)**				
	10	15	20	25	30
Full	0.3891	0.2567	0.0634	0.0126	0.0029
Pair	0.4724	0.3916	0.3308	0.3096	0.2973
GS-CaRe	0.3357	0.2978	0.2689	0.2584	0.2264
LS-CaRe($d_{\max} = 1$)	0.8505	0.8157	0.7755	0.7423	0.6879
LS-CaRe($d_{\max} = 2$)	0.8488	**0.8221**	0.8041	0.7714	0.7116
LS-CaRe($d_{\max} = 3$)	**0.8525**	0.8219	0.7943	0.7733	0.7161
Alcaine et al. [3]	0.7742	0.8108	**0.8402**	**0.8852**	**0.8944**
Method	M **(SNR = 40 dB)**				
	10	15	20	25	30
Full	0.4184	0.3935	0.1082	0.0206	0.0056
Pair	0.4340	0.3915	0.3295	0.3036	0.2829
GS-CaRe	0.3075	0.2958	0.2726	0.2443	0.2238
LS-CaRe($d_{\max} = 1$)	0.7820	0.8615	0.8168	0.7750	0.7013
LS-CaRe($d_{\max} = 2$)	0.7808	0.8649	0.8309	0.7957	0.7145
LS-CaRe($d_{\max} = 3$)	0.7822	**0.8669**	0.8193	0.7870	0.7227
Alcaine et al. [3]	**0.8756**	0.8534	**0.8916**	**0.8914**	**0.9089**

Table 4.3: F-Score for the different methods tested as a function of the lag (M) used for $p = 0.05$ and two values of SNR.

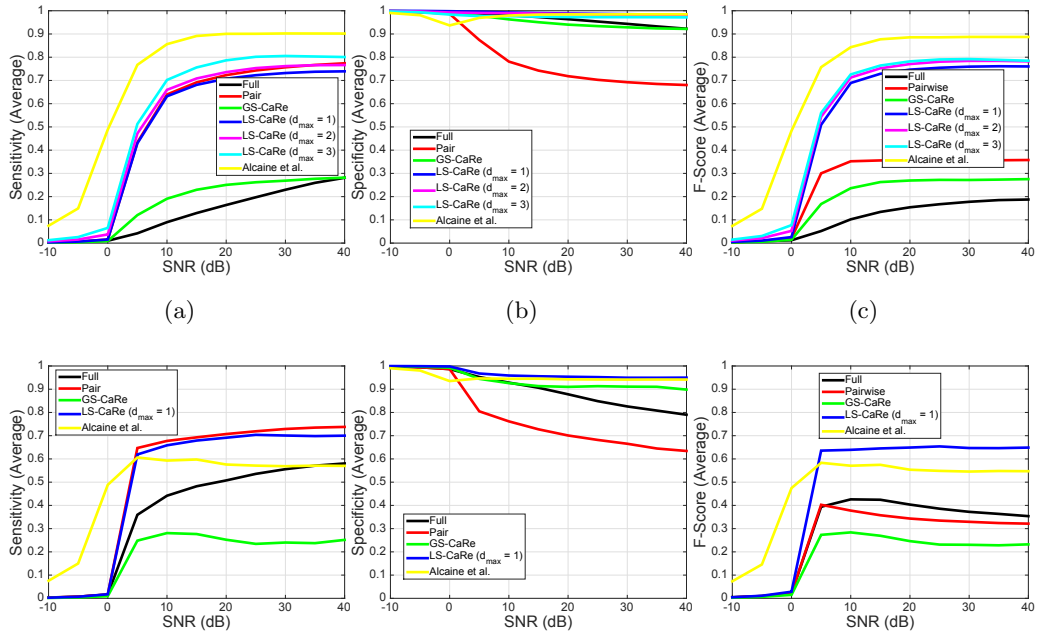

Figure 4.5: Averaged results, over the considered significance levels ($p \in \{0.05, 0.01, 0.001, 0.0001\}$) and orders of the AR models ($M \in \{10, 15, 20, 25, 30\}$), for the synthetic signals using different performance measures (sensitivity, specificity and F-score). **(a)**–**(c)** Using the simple model of Section 4.4.2. **(d)**–**(f)** Using the more realistic model of Section 4.4.3.

three cases (pairwise, full-conditional and GS-CaRe) is much lower than the F-score of Alcaine's method and LS-CaRe. Note the threshold effect in the sensitivity and F-score: below a certain SNR (around 0 dB) all methods fail. This effect is rather common in statistical inference problems (e.g. see Figure 1 in [93], Figure 2 in [76] or Figure 6 in [40]), and here is due to the incorrect estimation of the underlying AR models used for GC computation: no causal links are detected at all, and thus the sensitivity and F-score are zero, whereas the specificity is close to one.

Finally, Figure 4.6 shows examples of true causal connections and recovered causality maps (using SNR = 20 dB, $M = 10$, $p = 0.05$ and $d_{\max} = 1$ for LS-CaRe) for three cases: single 1, flat 2, and circular 4. All the methods add many spurious links, except for LS-CaRe and Alcaine's approach, which recover causality maps similar to the true ones.

4.4.3 Realistic Synthetic Electrograms

As a second case study, realistic electrograms were simulated using a complete 3D model of human atria [117]. Simulations were performed as in a previous study [115]: cellular electrophysiology was simulated using an AF-remodeled version of the Maleckar et al. model [77], whereas propagation of the action potential was computed by solving the monodomain equation with a finite element method-based software called ELVIRA [52]. The integration time-step used for the 3D atria simulations was 0.04 ms, so that the fast upstrokes of the action potentials could be properly generated, but the output voltages were only post-processed every 1 ms, facilitating comparison with real AF signals, typically acquired at 1 kHz (see Section 4.D). Three situations were simulated for 10 seconds each: sinus rhythm (periodic stimulation at the sinoatrial node every 500 ms), stable rotor at the right atrial appendage (not significant wavefront meandering during the whole simulation of AF), and chaotic activity at the right atrium (collisions of wavefronts, unstable rotors, and large wavefront meandering). In order to analyze the efficacy of the hierarchical algorithms, two grids of 16x16 virtual electrodes located at 2 mm distance from the atrial surface were used to compute unipolar

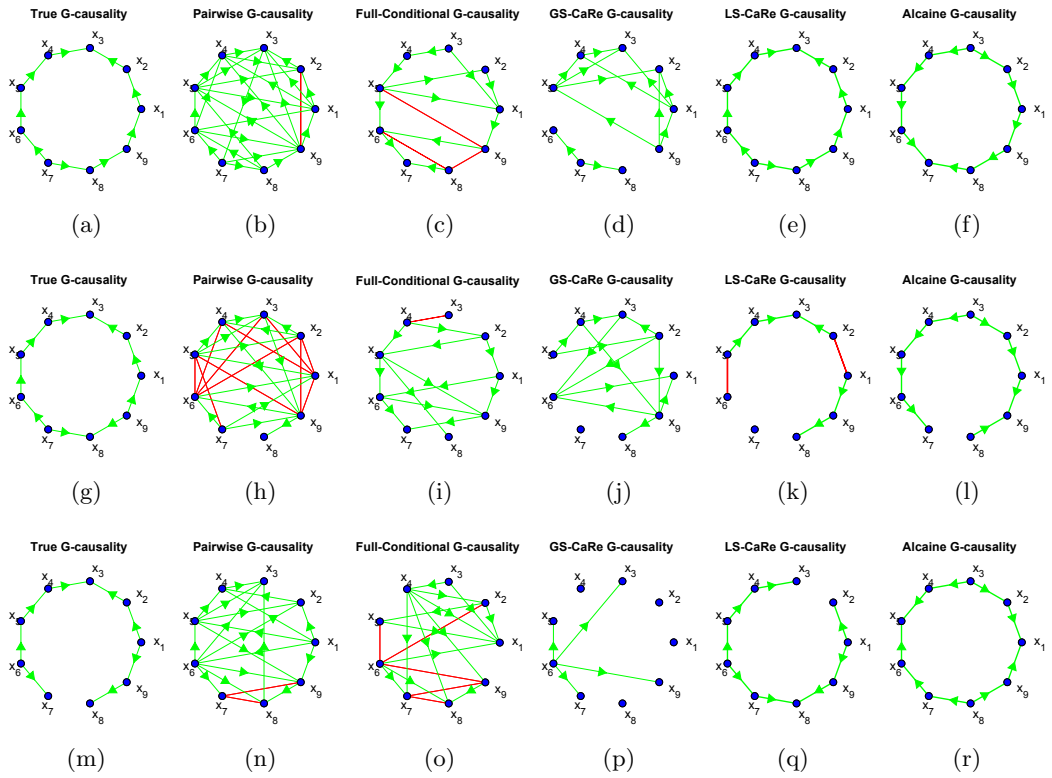

Figure 4.6: Synthetic signals: example of the true causality graphs [(a), (g) & (m)] and the graphs recovered using the pairwise approach [(b), (h) & (n)], the full-conditional technique [(c), (i) & (o)], GS-CaRe [(d), (j) & (p)], LS-CaRe [(e), (k) & (q)], and Alcaine et al. [3] [(f), (l) & (r)] for three different cases. **(a)**–**(f)** Single 1. **(g)**–**(l)** Flat 2. **(m)**–**(r)** Circular 4. Red lines with no arrowhead correspond to bidirectional causal links.

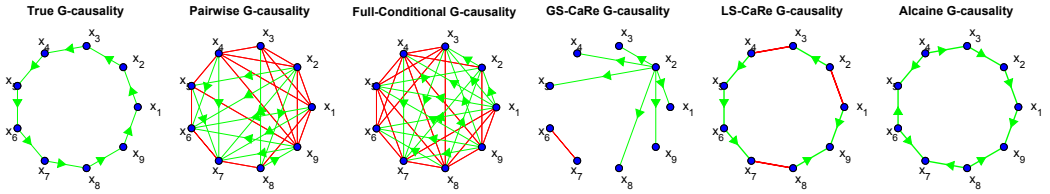

(a) (b) (c) (d) (e) (f)

Figure 4.7: Real AF signals: example of the true causality graph **(a)**, and the graphs recovered using the pairwise approach **(b)**, the full-conditional technique **(c)**, GS-CaRe **(d)**, LS-CaRe **(e)**, and Alcaine et al. [3] **(f)** for a real signal. Red lines with no arrowhead correspond to bidirectional causal links.

electrograms: one in the right atrial appendage, and the other in the center of the right atrium.

Figure 4.5(d)–(f) shows that the results for this more realistic model are similar to those of the simpler one: LS-CaRe and Alcaine's method still attain good values of TPR, TNR and F-score (although lower than in the previous example); the pairwise approach achieves good values of TPR, but poor values of TNR and F-score; and GS-CaRe and the full-conditional scheme obtain a good TNR, but not so good values of TPR and F-score. Indeed, the main difference with respect to the simpler model is that LS-CaRe obtains a better performance than Alcaine's method for the three performance measures.

4.4.4 Real Atrial Fibrillation Signals

Intracavitary EGMs were recorded in 5 patients with persistent AF prior to an ablation procedure in the electrophysiology laboratory at HGUGM. Using a 10 pole spiral catheter Lasso® (Biosense Webster, Diamond Bar, California, USA), 9 bipolar signals were obtained and bass-pand filtered within the 30-500 Hz band using the LABSYSTEM™ Pro EP Recording system (Boston Scientific, Natick, MA, USA). Data was digitized at 16-bit resolution with 1 kHz sampling frequency, and exported using custom software implemented in LabVIEW™ (National Instruments, Austin, TX, USA). Signals were visually inspected and annotated for

Signal	Pairwise	Full	GS-CaRe	LS-CaRe	Alcaine et al.[3]
1	0.323	0.245	0.173	0.512	**0.702**
2	0.400	0.390	0.277	0.703	**0.707**
3	0.344	0.257	0.247	0.379	**0.446**
4	0.394	0.410	0.321	**0.822**	0.801
5	0.257	0.189	0.212	0.396	**0.581**
6	0.426	0.291	0.411	**0.685**	0.553
7	0.323	0.228	0.260	**0.565**	0.500
8	0.282	0.203	0.158	0.498	**0.500**
9	0.347	0.271	0.139	**0.525**	0.349
10	0.474	0.515	0.367	**0.713**	0.701
Avg. ± Std.	0.357 ± 0.066	0.300 ± 0.105	0.257 ± 0.090	0.580 ± 0.146	**0.584 ± 0.141**

Table 4.4: F-Score for the different methods tested averaged over the five lags and the four significance levels considered.

Signal	Pairwise	Full	GS-CaRe	LS-CaRe	Alcaine et al.[3]
Sensitivity	$\mathbf{0.661 \pm 0.206}$	0.477 ± 0.198	0.244 ± 0.103	0.606 ± 0.177	0.611 ± 0.133
Specificity	0.772 ± 0.085	0.815 ± 0.075	0.935 ± 0.020	$\mathbf{0.951 \pm 0.016}$	0.947 ± 0.019
Accuracy	0.761 ± 0.062	0.782 ± 0.060	0.866 ± 0.021	$\mathbf{0.916 \pm 0.025}$	0.913 ± 0.029
F-Score	0.357 ± 0.066	0.300 ± 0.105	0.257 ± 0.090	0.580 ± 0.146	$\mathbf{0.584 \pm 0.141}$

Table 4.5: Averaged results for several performance metrics, the five lags and the four significance levels considered.

rotor presence by electrophysiologists from HGUGM. A total of 10 short EGM segments where the signal can be considered stationary were used as dataset for our algorithm, including 6 cases exhibiting normal AP wavefront propagation (wedge shaped) and 4 with circular propagation patterns (rotors). For all the cases, ground truth graphs displaying the electrode activation sequences from source to sink node(s) were constructed. An example of one true causality graph, altogether with the reconstructed causality graphs is shown in Figure 4.7. Note again the good performance of LS-CaRe and Alcaine's methods, especially compared to the large number of spurious links introduced by the pairwise, full-conditional and GS-CaRe approaches.

The results for the 10 real signals tested are displayed in Tables 4.4 (F-Score for each case) and 4.5 (sensitivity, specificity, accuracy and F-Score averaged over

the 10 cases). The following conclusions can be drawn from these two tables:

- The pairwise approach attains the highest sensitivity, with Alcaine's method and LS-CaRe obtaining slightly worse results. The full-conditional approach and GS-CaRe obtain much lower sensitivity values, due to the large number of true causal connections missed.

- In terms of specificity, LS-CaRe, GS-CaRe and Alcaine's methods behave much better than the other two (with LS-CaRe performing slightly better than Alcaine's). This is due to the fact that the other two approaches introduce many more false positives.

- In terms of global performance, LS-CaRe provides the best accuracy and Alcaine's method attains the highest F-score. The global performance of the other three methods is much worse, with the pairwise approach attaining the lowest accuracy and GS-CaRe the lowest F-score.

4.5 Conclusions

A generic hierarchical framework and two specific algorithms for causality retrieval in intracavitary EGMs, based on G-causality, have been described in this chapter. Both algorithms rely on the initial discovery of the root node, but the influence of this node on their performance is very different: GS-CaRe depends critically on a proper selection of this root node, since a global search is then started from it and an erroneous choice invariably leads to poor results, whereas LS-CaRe only needs this root node as the starting point for its local search and thus is much more robust with respect to an erroneous selection. This robustness, altogether with the reduced number of false alarms introduced by the local search, explains the much better performance of LS-CaRe, which shows a comparable performance to the method proposed in [3] by Alcaine et al. Indeed, both LS-CaRe and Alcaine's approach have the same goal: restricting the search for causal connections to neighbors. However, the procedures followed to achieve this goal are very different: defining a novel local propagation direction measure (Alcaine's) and per-

forming a structured hierarchical search (LS-CaRe). From a clinical point of view, the developed methods can be used by cardiologists for two purposes: (1) discriminating among different propagation patterns (e.g. flat or circular propagation vs. rotors); and (2) determining the direction of the received AP wavefront. In future work, we plan to incorporate other alternative measures of causality, like transfer entropy or the phase slope index, as well as Alcaine's novel local propagation direction measure, into the flexible framework described here.

5

Clinical Applications

5.1 Introduction

This chapter is devoted to the developed clinical tools and the analysis of the Atrial fibrillation (AF) signals acquired as a result of the implementation in the clinical practice of the signal processing methods introduced in the previous chapters. As we already outlined in Chapter 1, one of the objectives of this thesis is the assessment of rotational activity detection in live AF procedures. Therefore we need to employ an existing platform or develop our own system to achieve such goal. Unfortunately, the limited and restrictive features of the commercial solutions installed in electrophysiology (EP) laboratories, i.e., electroanatomical mapping (EAM) and signal recording systems, forced us to face the challenge of developing our own system from scratch. Normally, conventional EP systems do not allow to directly access the feed of EP signals (electrograms (EGMs) and elec-

trocardiograms (ECGs), and most of the times the only option is to export the data to a binary or text file and load it into an external system. The main disadvantage of this approach is the time spent in exporting and importing the data, which impedes to perform any task in real-time. This alternative remains suboptimal for our real-time result presentation purpose. For this reason we decided to develop our own signal processing system, taking advantage of the analog output signals offered by an operational amplifier installed in the EP laboratory at the Hospital General Universitario Gregorio Marañón (HGUGM), LABSYSTEM™ Pro EP Recording system (Boston Scientific, Natick, MA, USA).

In this system we implemented the complete rotational activity detection solution comprising: signal acquisition, signal processing and result presentation. Additionally the registers acquired during the AF procedures allowed us to further extend our study to both test the capabilities of our new system, and to perform a thorough analysis of the signals and their relationship to the possible mechanisms driving or sustaining AF. We make use of electroanatomical maps generated during the signal acquisition stage used to assess rotational activity.

5.2 Rotational Activation Detection System

The rotational activity detection system is based on an analog to digital converter (ADC), a processing unit and a monitor to display the results [1]. The system can be easily integrated with other equipment commonly used in EP laboratories, as shown in Figure 5.1. In the examples and previous chapters of this thesis, we consider a pentametric shape catheter that consists on five branches with 4 electrodes, 20 in total, but other models can be used, i.e., circular, spiral, or basket.

The amplifier at the laboratory provides unipolar intracavitary EGMs from a

[1] Appendix A further details the implementation and hardware specifications for the rotational activity detection system, i.e., specifications, connectivity and technical settings. The signals acquired with this system are used in Chapters 2, 3, and 4 to validate and test the methods and algorithms.

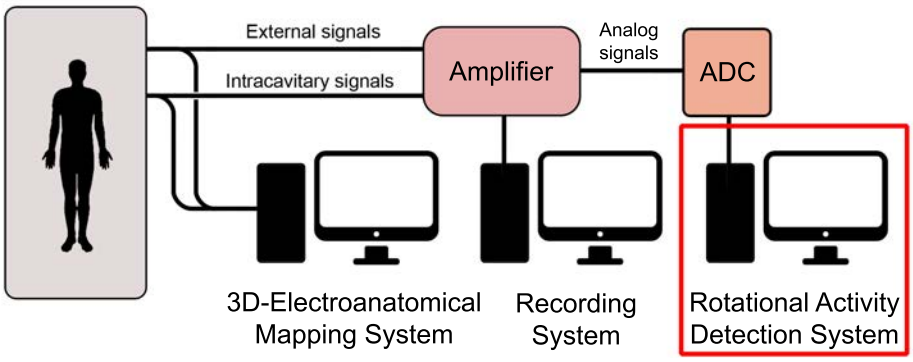

Figure 5.1: Electrophysiology equipments in AF ablation procedures. From left to right, we have a 3D EAM system for anatomic reconstruction and clinical guidance, a recording system that registers and keeps track of all intracavitary and external signals, and the rotational detection system highlighted in red which identifies the presence of rotors and displays results in real-time. We intentionally omit the fluoroscopy imaging system for the sake of simplicity.

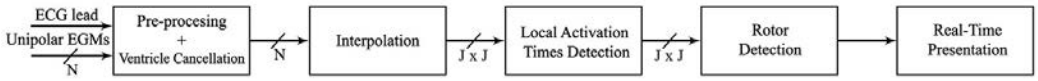

Figure 5.2: Signal processing unit diagram implementing the rotational activity detection system. It receives as inputs N unipolar EGMs and one ECG lead, processes the signals and presents results in real-time.

multi-electrode catheter, and a reference external ECG. Although bipolar signals are preferred in clinical practice because of the far-field cancellation feature, they lack to provide precise local electrical activation information, as the electrical activation time instant cannot be accurately identified [119]. For this reason unipolar configuration is preferred as the electrical activation timing is well defined by the point of maximum negative slope, and therefore activation maps can be built, on the expense of recording far-field ventricle activity, which can be later removed by using signal processing techniques. Other mapping solutions, i.e., RhythmView™ (Abbott, Topera Medical, San Diego, CA, USA), CARTOFINDER™ (Biosense Webster, Diamond Bar, California, USA), or AcQMap® (Acutus Medical, Carlsbad, CA, USA), also employ unipolar signals [88, 35, 47].

The sequence of operations to detect rotational activity from the acquired signals is shown in Figure 5.2. These steps comprehend the implementation of the methods presented in Chapter 2 and Chapter 3 into a functional clinical system. Following the steps detailed in Figure 5.2, we remove the baseline wandering present in unipolar signals and cancel the ventricle contribution to isolate the atrial activations. Then, we approximate the slope of the the unipolar deflections related to the activation times of the atrium. By applying signal spatial interpolation on a regular bidimensional grid, we achieve independence from the catheter topology employed for mapping the atrium. Finally, we identify atrial activation times and perform the rotational activity detection. Wavefront propagation intervals where the value of $\Gamma[n]$ (see Chapter 3 Section 3.2.3) exceeds the detection threshold are presented to the electrophysiologist in a monitor inside the operating room at reduced speed, as Figure 5.3 shows. Finally, the rotor location in the atrium can be annotated on any 3D EAM system as guiding reference during ablation.

5.3 Spatial Analysis of Rotational Activity in Atrial Fibrillation

The implementation of the rotational activity detection system allowed us to register EGM signals from patients with persistent AF at different sites in the left atrium. We built a database containing the intracavitary EGMs and external ECGs recorded during the ablation procedures at the hospital. To assess the ability of the system to detect rotational activity, we used registers from 28 different patients who underwent radiofrequency ablation for pulmonary vein isolation (PVI) at the HGUGM. The signals were recorded prior to the ablation procedure. Catheters were inserted through the femoral vein to the coronary sinus, and via transseptal puncture to the left atrium. A PentaRay® (Biosense Webster, Diamond Bar, California, USA)catheter with $2-6-2$ mm inter electrode spacing was employed to assist in the anatomical mapping, and to record the intracavitary signals at 1 KHz sampling frequency. Each recording consists of 16 channels, i.e., 15

Figure 5.3: Operating room monitors during the AF ablation procedure. Right to left, real-time ratational activity detection system, EP signal recording system, idle screen, fluoroscopy image, and 3D EAM navigation system. Upper monitor displays the vital signs of the patient.

intracardiac EGMs and one additional external ECG lead. We require the catheter to remain stable during the acquisition, branches to be spread for full-coverage as displayed in Figure 5.4, and the electrodes to be in contact with the atrial wall.

The total number of recorded files is 602 (21.5 ± 8.26 areas per patient). Additionally a 3D map of the left atrium created by the CARTO® 3 (Biosense Webster, Diamond Bar, California, USA)system is included in the database for each patient entry, an example of one of the maps can be found in Figure 5.5. All visited atrium locations where the catheter was placed during the anatomical mapping were annotated in the electroanatomical map.

With all this information we reviewed the EGM signals and the isochronal maps containing the reconstructed electrical activity of the atrium, and proceeded to label the sites in which rotational activity was found. The sites were labeled according to the complexity of the gyre, i.e., *no gyre*, *incomplete gyre*, *complete gyre*,

	Mean ± SD or %
Male Sex	81%
Age (years)	60.2 ± 6.8
Weight	88.8 ± 15.7
Size (cm)	168.2 ± 21.9
Body mass index (kg/m^2)	29.9 ± 4.8
AF to Perst-AF diagnosis (months)	18.6 ± 19.3
Diabetes Mellitus	18.5%
CHA2DS2VASC Score	1.52 ± 1.2
Hypertension	44%
Antiarrhythmic Treatment	44.4%
AVN Blocker Treatment	85.2%
LA diameter (mm)	44 ± 5.2
LVEF (%)	56.5 ± 9.2

Table 5.1: Population statistics of the 28 database registers used for the analysis.

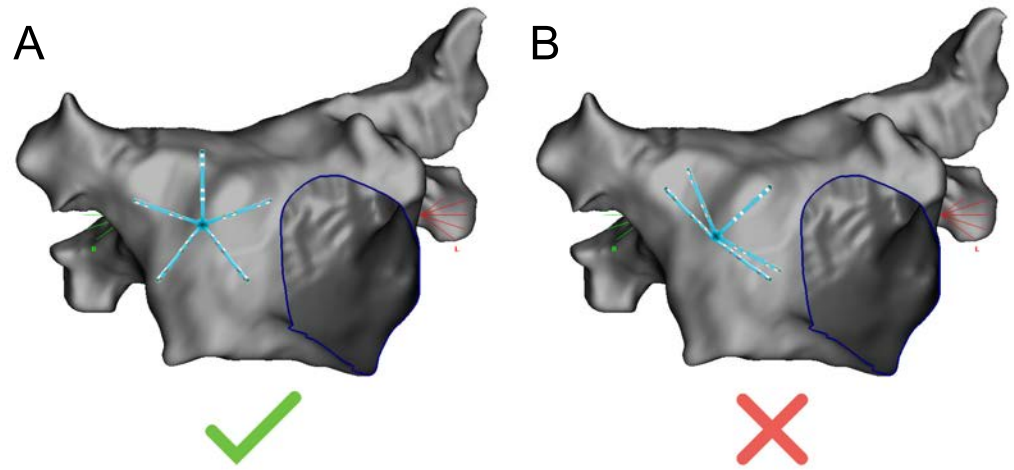

Figure 5.4: Catheter layout during acquisition. **A.** Adequate deployment with all the branches equally spread. **B.** Inadequate deployment with overlapping branches.

and *multiple gyre*. We include an illustrative example of the gyre classification in Figure 5.6. We define a *complete gyre* when the activation pattern exhibits a rotation and any of the electrodes in the first activated branch is activated again. A *multiple gyre* is labeled when the wavefront performs consecutive complete gyres. In the *incomplete gyre* the activation exhibits circular patterns but the first activated branch is not reactivated. The rest of the patterns and activations are included into the *no gyre* group.

Once the signals were reviewed and classified according to the gyre complexity by two independent annotators, we studied the spatial position in the atrium where they were acquired using the acquisition points in the electroanatomical 3D maps. For this task, we divided the left atrium into 12 different areas, and for each recording, we associated the location of the atrium wall region covered by the center of the acquisition catheter to one of these areas. In our 2D representation of the left atrium, we sliced and unfolded the atrial chamber as Figure 5.7 shows. As shown in Table 5.2, the areas are named as suggested by [80] with right and left subdivisions, and labeled 1 to 12 following no specific ordering. Pulmonary veins are represented by thick black rectangles, and their left-to-right connection with a bold line. Left atrial appendage is removed from the illustration and only

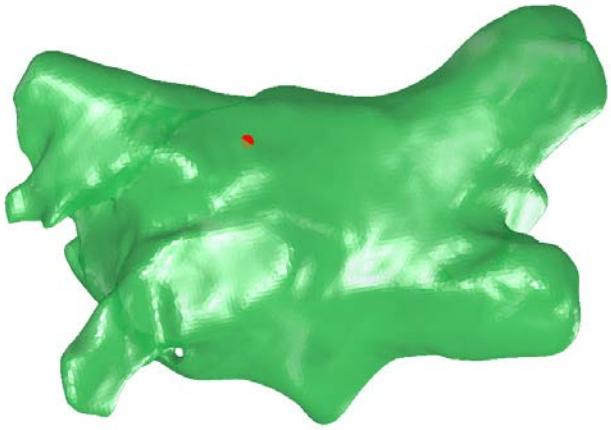

Figure 5.5: Projection of the left atrium from the reference 3D model used for annotation. The map contains one annotated point in red.

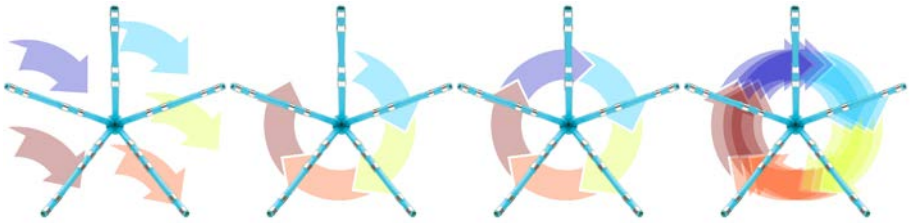

(a) (b) (c) (d)

Figure 5.6: Gyre complexity classification. (a) No gyre. (b) Incomplete gyre. (c) Complete gyre. (d) Multiple gyre.

its border which is connected to the atrium is included, represented by thick grey lines in areas (1) and (9).

This study has a twofold objective, the first one is to assess the existence of rotational activations and to analyze if rotational sites are related or not to specific atrial regions, what would help us to better understand the mechanisms behind AF maintenance.

The second objective of this study is to evaluate the mapping functionality of the acquisition stage, i.e., study if there are some regions in which the catheter signal acquisition experiments limitations in terms of correct deployment and stability. For this reason we checked the positions of the catheter branches at the

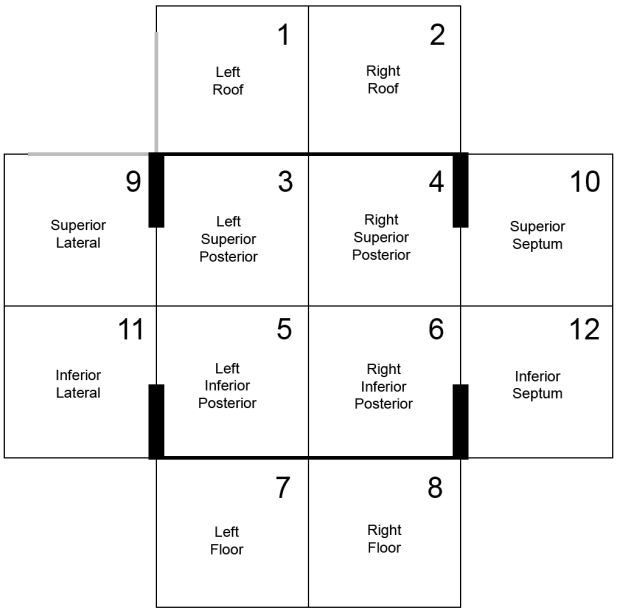

Figure 5.7: Layout of the atrial areas. Pulmonary veins are represented as black circles and their left-to-right junction is highlighted. Left atrial appendage is removed from the illustration, and only its border connected to the atrium is included, represented in thick gray lines.

#	Area	#	Area
1	Left roof wall	7	Left floor wall
2	Right roof wall	8	Right floor wall
3	Left superior posterior wall	9	Superior lateral wall
4	Right superior posterior wall	10	Inferior lateral wall
5	Left inferior posterior wall	11	Superior septum wall
6	Right inferior posterior wall	12	Inferior septum wall

Table 5.2: Names and labels for the left atrium divisions.

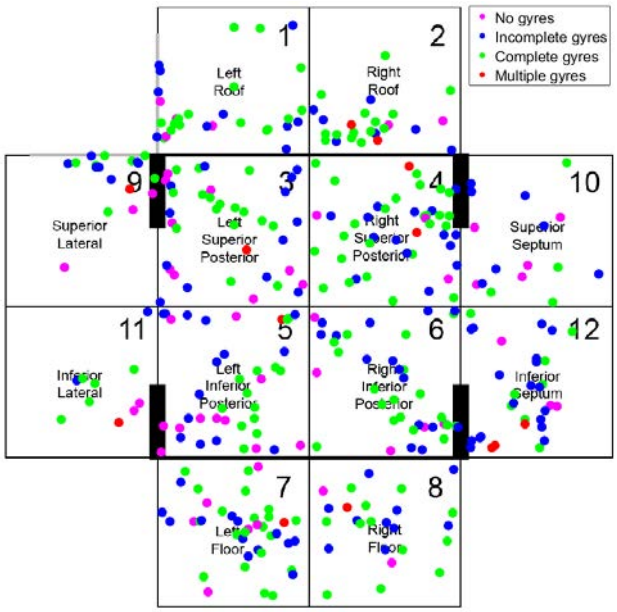

Figure 5.8: 2D spatial distribution of the rotational activity sites with adequate catheter deployment. Gyre complexity classification was used attaining: *no gyre*, *incomplete gyre*, *complete gyre*, and *multiple gyres*.

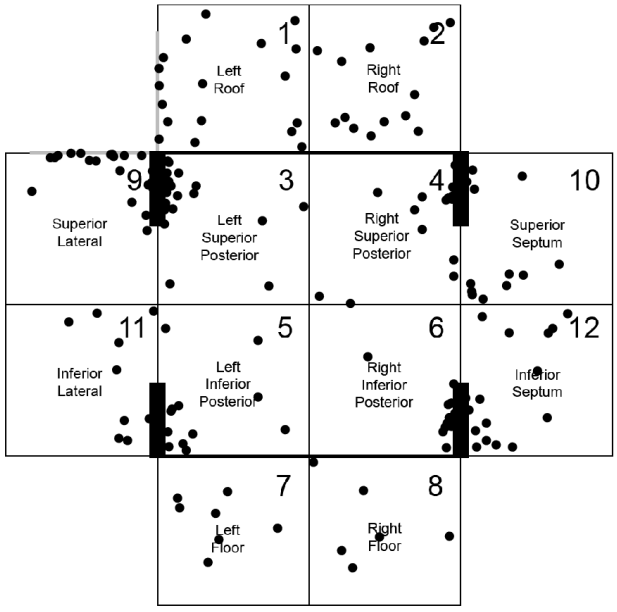

Figure 5.9: Sites where the catheter experimented inadequate deployment. Note the point density around the pulmonary veins showing the difficulty of mapping these areas.

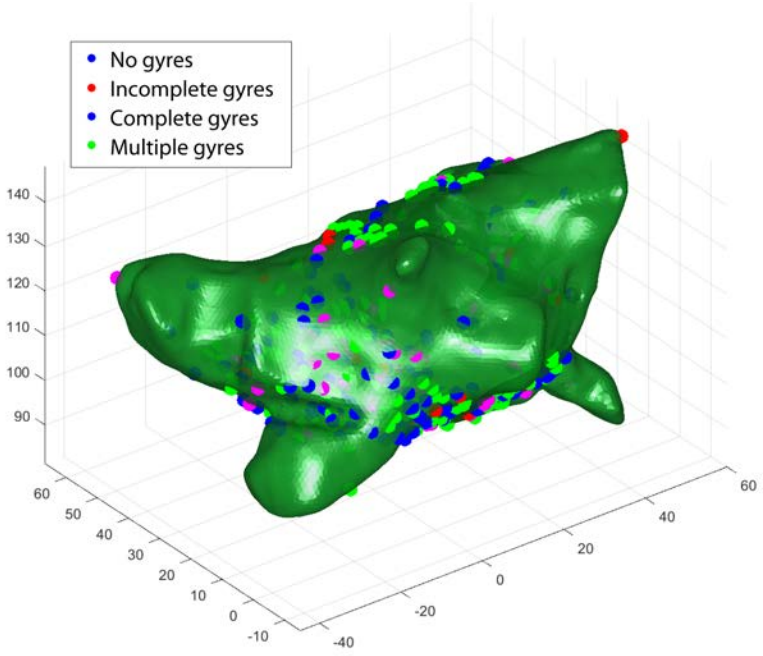

Figure 5.10: 3D spatial representation of the rotational acitivity sites, analogous to the 2D representation in Figure 5.8. Gyre complexity classification: *no gyre*, *incomplete gyre*, *complete gyre*, and *multiple gyres*.

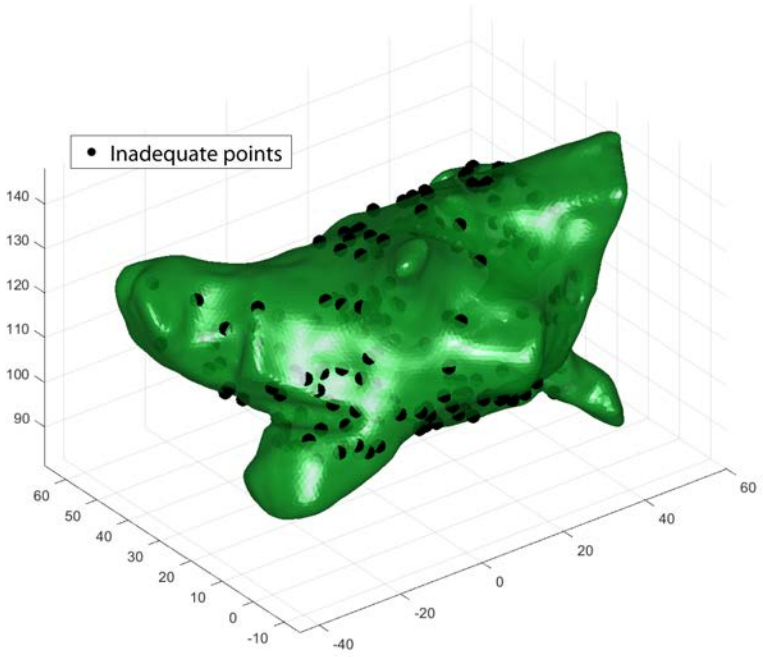

Figure 5.11: 3D spatial representation of the sites with inadequate catheter deployment, analogous to the 2D representation in Figure 5.9.

acquisition time with the help of the EAM system, and labeled those acquisitions with inadequate deployment, see example in Figure 5.4, and represented using the same 12-area division, as in Figure 5.7. The adequate points are displayed in Figure 5.8, and the inadequate catheter deployment positions in Figure 5.9. We also represented the points into the 3D left atrium regarding the same adequate and inadequate criteria for the points, Figures 5.10 and 5.11 respectively.

In the registers, the majority of the sites evaluated showed rotational conduction to some degree. As Figure 5.8 shows, the spatial representation of the rotational sites showed no association with any particular left atrium location. This provides evidence of the possibility of rotors not anchoring to specific atrial regions, but to appear at different sites in the atrium.

We found pulmonary veins to be more difficult to map as their morphology and the constant heart activity prevent the catheter to remain stable and fully spread if compared with other regions like the posterior wall or the atrial roof. This study also allowed us to improve the acquisition step prior to applying the activation detection algorithm. At the same time these acquisitions allowed the electrophysiologists involved in the study to get familiar with the protocol and the system requirements.

5.4 Substrate Characterization of Rotational Activation Sites

We consider that additional study on the spatial information of the rotational activation sites may increase our knowledge about the driving mechanisms behind AF. For this purpose we extended the spatial analysis of the areas found with rotational activity in the Section 5.3, and included the voltage information provided by the EAM systems. With this approach, we try to characterize the points related to rotational activation and analyze if there is a measurable feature, e.g. the electroanatomical voltage maps, that might help us to identify rotor harboring sites. This analysis offers an advantageous insight to those areas which present lim-

ited access to multi-electrode catheters, or on those sites where catheter stability cannot be ensured.

We included 28 consecutive persistent AF patients referred for first ablation, the same signal database as we used in Section 5.3. We employed the rotational activity detection system to process the signals in real-time and automatically assessed the presence of rotors. The acquisition and the high density EAM was performed using the PentaRay®catheter and CARTO® 3 system. The catheter was required to remain stable and fully spread during the acquisition of the signals. Recordings were acquired for at least 10 seconds per site and the catheter's position was annotated in the 3D map. The system detected rotational activity, generating a video for each site containing rotational atrial wavefronts using isochronal maps. Similarly to the previous section the same gyre complexity annotation was used again attaining *incomplete*, *complete*, *multiple* or *no gyres*. Rotational activity was defined for complete o multiple gyres. Finally, electroanatomical maps were exported offline to a text file so we could measure the bipolar voltages of the registered sites of the left atrium.

The electroanatomical voltage maps provide detailed information of the atrial tissues, with current technologies guaranteeing measurements with real electrode contact on the atrial wall. Additionally, they characterize the atrial anatomy achieving a spatial location accuracy of ± 1 mm. They also compensate the heart movement activity, generating trustful maps on which we can rely to perform further analysis. Apart from unipolar-bipolar voltage maps they also provide impedance values and even propagation maps of the electrical cardiac activity.

To make the most of the electroanatomical maps, we developed a novel software application to review and analyze these maps in detail. We developed a custom application specifically designed to read 3D electroanatomical maps and compute voltage measurements given a point in the atrial chamber. Our purpose is to create a software based platform for the electrophysiologists so they can handle the electroanatomical map reviewing in different devices, i.e., PC or laptop, as an alternative to the review application offered by the EAM systems. Our application

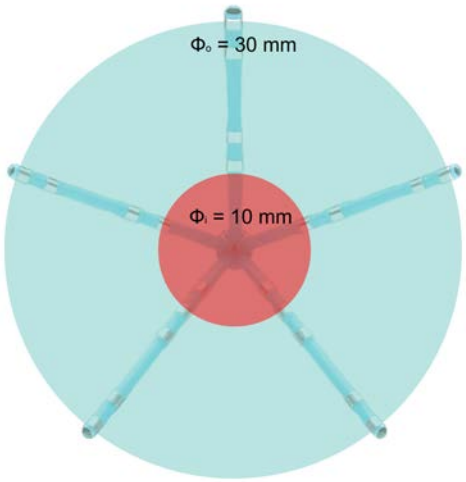

Figure 5.12: Concentric circles used to measure the bipolar voltage in the 3D electroanatomical maps. The inner circle is defined for a diameter $\phi_i = 10$ mm, and the outer circle for a diameter of $\phi_o = 30$ mm that comprises the total coverage of the PentaRay®catheter.

contains similar reviewing tools as the ones provided by the EAM systems, like the thresholded visualization of the unipolar-bipolar maps, or the interactive 3D view to freely check any atrial region. Furthermore, the customization of the software presents flexibility to be adapted to the specific needs of the study.

In the study, although the location accuracy achieved by the CARTO® 3 system is ±1 mm, we propose to use two concentric circular measurements to analyze the tissue voltage to compensate any displacement of the catheter during the acquisition. For each rotor site in the voltage map we define an inner circle of diameter $\phi_i = 10$ mm to analyze the tissue where the rotor spins/anchors, and an outer circle of diameter $\phi_o = 30$ mm, see Figure 5.12. These circles encompass the operational coverage of the PentaRay®catheter that was employed for mapping the atrium and signal acquisition in this study.

The application automatically calculates the mean voltage at the circles and presents it in the developed graphical user interface, as Figure 5.13 shows. For the measurements, we only take into account real voltage points. To exclude mapped areas exhibiting low voltage data density, a minimum number of 10 real voltage

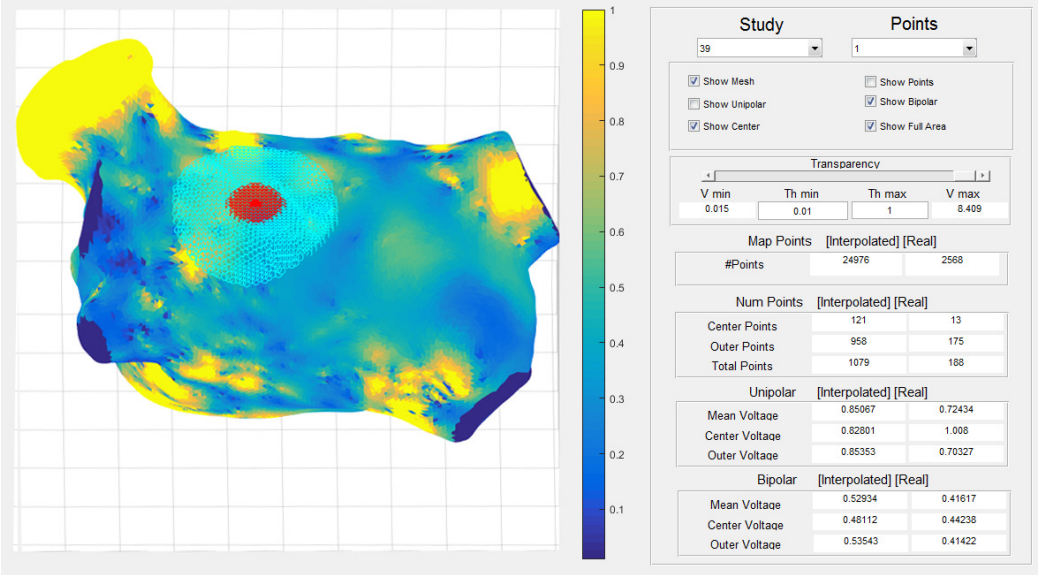

Figure 5.13: General view of the graphical user interface developed for the novel software tool implemented for electroanatomical map analysis. In the application any point in the 3D map can be interactively selected, and the voltage values from unipolar and bipolar maps are automatically computed and displayed.

values per site is set for the rotor points to be included in the analysis. This also removes points that are projected on the 3D map shell that were acquired too far from the atrial surface, this is outliers that may alter the results.

We evaluated a total of 603 registers (mean 21 sites/patient). We rejected 214 due to inadequate deployment or noisy signals. Rotational activity was found in 243 sites (the remaining 146 sites exhibited no rotations). For the voltage analysis we included 93 sites exhibiting complete or multiple gyres, and discarded 150 sites with no agreement between annotators or that contained fewer than 10 real voltage points in the 3D map.

The mean bipolar voltages for all labels were 0.65 ± 0.38 mV (mean±std) for the inner circle, and 0.61 ± 0.31 mV in the outer one. Table 5.3 summarizes the statistics of the bipolar voltage study.

The voltage distributions of the two concentric circles are displayed in Figure 5.14. The histograms and the content of Table 5.3 describe the voltage at the rotational activation sites. The voltage is centered around 0.65 mV, with the inner

Statistics	Inner Bipolar Voltage (mV)	Outer Bipolar Voltage (mV)
#Rotor sites	93	93
Mean	**0.6533**	**0.6192**
Median	0.5964	0.5262
Mode	0.8586	0.3420
Standard deviation	0.3841	0.3132
Range	2.6516	1.6967
Percentile 5	0.1633	0.2666
25	0.3905	0.3944
75	0.8385	0.7302
95	1.3519	1.2844

Table 5.3: Bipolar voltage statistics concerning the proposed inner and outer regions to measure the rotational activity points.

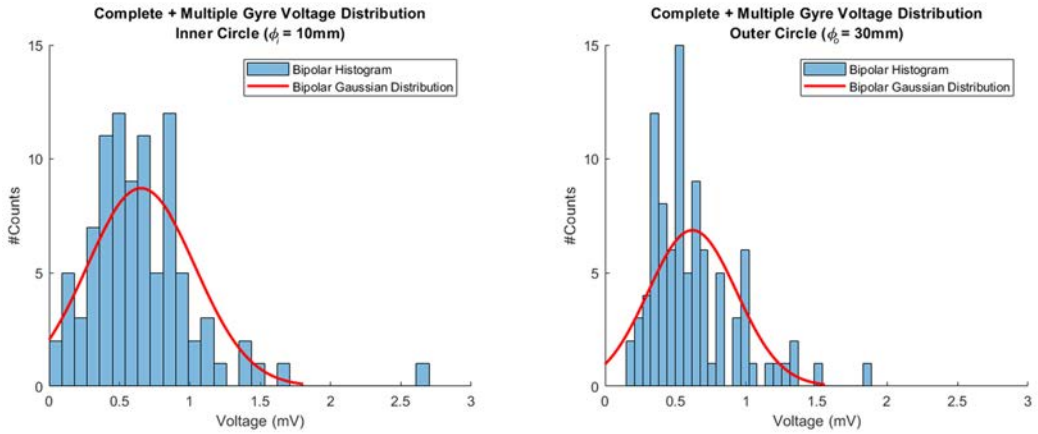

Figure 5.14: Bipolar voltage distribution of complete and multiple gyre sites for the inner and outer measurement circles.

circle measurement to present a higher voltage range, 2.65 mV, with respect to the outer voltage 1.70 mV. This result may be due to the higher number of points involved in the calculation of the average voltage, since a bigger circle diameter implies a bigger calculation area for the voltage measurement.

Finally we want to highlight that the analysis shows evidence of voltage values related to rotational activity beyond bipolar voltage range 0.1-0.5 mV, classically considered for scar definitions. Functional assessment may add incremental value to invasive treatment of AF.

6 Conclusions

6.1 Summary

In this chapter, we outline the contributions of this thesis and we contemplate future research lines.

The contribution of this thesis range from new methodological algorithms and methods to technical implementations in the clinical practice.

As for the methodological contributions, we have developed new signal processing methods to assess the presence of rotational activity (rotors) in Atrial fibrillation (AF) patients using multi-electrode catheter electrograms (EGMs). We have derived a new local activation time (LAT) detection method for identifying unipolar activations. Our method manages to overcome the far field contribution problem by canceling the ventricle EGM contribution with an average beat subtraction method. Sequentially our new filtering approach (which resembles a

discrete-time low pass differentiator) manages to extract the slope information of the signal while greatly reducing the noise present in the signal. With these methods we are able to identify LAT in signals acquired with multi-electrode catheters. Our methodology becomes an alternative to the classical LAT detection based on the first derivative of the signal $\frac{dV}{dt}$.

Additionally, we have developed a new rotational detection algorithm based on the optical flow dynamics of LAT isochronal maps built from multi-electrode catheter EGMs. By using spatial interpolation we have managed to translate the position of the electrodes in a catheter into a regular 2D grid. Thanks to this representation, our detection algorithm can be easily adapted a wide variety of multi-electrode catheters. Hence we do not restrict the method to specific catheter types as other commercial solutions do. Because of choosing to detect the rotational activations in the time domain, we have managed to reconstruct the atrial activity as it appears in the tissue in contact with the electrodes. This is an alternative to phase singularity (PS) detection methods that used the phase domain to estimate rotational activity sites in the atrium. What is more, phase maps was proved to not offer a good correlation with the temporal activations, making it prone to false detections.

As final methodological contribution we have developed new methods to estimate the directionality of the electrical wavefronts in the heart using multi-electrode catheters and causal graphs. We have developed new indices based on the causal strength between EGM signals using Granger's causality related measurements. Thanks to these indices we have managed to assess the directionality of the EGM wavefronts. We have compared our approach to other existing methods in the literature with promising results.

Altogether we have tested our methodology using *in silico* and real signals from AF patients. These signals have allowed us to improve our algorithms and to better understand the problem of AF when applied to real clinical scenarios.

Regarding the technical contributions of this thesis, we have managed to implement the new methods into a signal processing system. The system have been

proven useful to assess rotor presence in real-time in AF patients. Using the system and thanks to the spatial distribution study of the rotor sites, we have also managed to characterize the rotational activation sites in terms of voltage using the maps generated with electroanatomical mapping (EAM) systems. We have also checked the ability to deploy the catheter regarding the signal acquisition prior to the rotor detection. Thanks to all this work, we have developed a new clinical study based on the ablation of rotor sites detected with out system. Results on patient recurrence will confirm the real success of our contributions.

6.2 Future Work

The work introduced in this thesis opens potential research lines, both methodological (e.g. new signal processing methods) and application based. We briefly present some of the ideas for future research.

Multicatheter analysis. Our methods rely on the analysis of signals registered by a single catheter, so an interesting idea consists in the addition of other catheter signals to improve the outcome of existing methods and also to challenge new ones.

Rotor tracking. The problem of tracking wandering rotors is still an open problem, a potential improve in this line would benefit from Bayesian filtering techniques, e.g. particle filters, applied to this problem. Recent work on this idea have been done in [32, 33, 100], with promising preliminary results.

Development of new indexes to address ablation sites. Physiological limitations affects the correct deployment and access of the catheter to atrial areas. In this sense new ablation indices based on values like impendance level, voltage, or even frequency should be studied to be able to characterize limited accessible regions of the heart chambers.

Merge our system with current EAM systems. To overcome the electrode layout requirement and to increase the number of EGM channels that can be processed at the same time, one of the possibilities that we have in mind is to implement our methods in an existing EAM software. This way we would have

access to signals and positions in real-time, and update the interpolation layout accordingly.

Patient tailored *in silico* maps. The work derived from this thesis has opened a new research line focusing on creating patient specific 3D atrial models. With these models we aim to study the AF in simulation scenarios using the EGM signals and electroanatomical maps information [99, 101].

A

Real-time Rotational Activity Detection System Specifications and Implementation

A.1 Appendix 1 section

The acquisition and signal processing solution is connected to the 16-channel analog output of the LABSYSTEM™ Pro EP Recording system (Boston Scientific, Natick, MA, USA)amplifier; it incorporates an analog to digital converter (ADC) manufactured by National Instruments (NI) composed of:

- Shielded cable *NI SHC68-68-EPM*, designed to work with data acquisition (DAQ) devices, featuring individually shielded analog twisted pairs for reduced crosstalk with high-speed boards.

- Shielded input/output (I/O) connector block *SCB-68A*, providing rugged, very low-noise signal termination in combination with the shielded cable. The connector block contains mechanical enclosure with a magnetic removable lid, resettable fuse, and screw terminals for the input channels.

- DAQ device *NI PCIe-6323 X Series* of 32 analog inputs, sample rate $250kS/s$, 16 bits resolution, and voltage range $\pm 10V$. DAQ devices with PCI Express interface are optimised for high throughput and low latency. Product includes multithreaded NI-DAQmx driver software, allowing concurrent execution of several processes. The device is compatible with C/C++, Matlab, and Microsoft Visual Studio.

The ADC works at a sampling frequency of 1 KHz, the connector block connects the 16 analog channels from the electrophysiology (EP) amplifier to the acquisition board with a shielded cable, delivering the signals to the DAQ device, installed in the personal computer located in the adjacent room of the EP laboratory. The computer runs calculations with one Intel® Xeon® CPU 8-core 3.40 GHz processor, and 16GB RAM, on Windows 7 Professional 64 bits operating system. A graphical processing unit (GPU), Nvidia Tesla K20c with 2496 CUDA cores, is used for the intensive computing calculations.

The settings of the output analog channels are assigned in the LabSystem PRO™ software, selecting as inputs for the system 15 channels coming from the PentaRay® (Biosense Webster, Diamond Bar, California, USA)catheter, and an electrocardiogram (ECG) lead as external channel. Voltage range is set to $\pm 2mV$ for intracavitary electrogram (EGM) channels, and $\pm 5mv$ for the external lead. Signals are filtered using a 50 Hz Notch filter, band pass filtered $0.05 - 50Hz$ for the unipolar channels, and $0.05 - 100Hz$ for the ECG.

A.2 Real-Time Implementation

The rotational activation detection system (patent pending) is currently implemented in real-time using an ADC manufactured by National Instruments and

a PC.The dynamic range of the amplifier is $\pm 2mV$ for intracavitary EGMs, and $\pm 5mV$ for ECGs, with a voltage gain of 60 dB at the ADC input. Wilson central terminal acts as the indifferent electrode in unipolar configuration. Signals are filtered using a 50Hz Notch filter, band pass filtered 0.05-50 Hz for unipolar EGMs, and 0.05-100 Hz for ECG leads. The ADC connected to the amplifier works at a sampling frequency of 1 KHz.

The computer has one 8-core Intel® Xeon® CPU 3.40 GHz processor, 16GB RAM, on 64 bits Windows 7 Professional. A GPU, Nvidia Tesla K20c with 2496 CUDA cores, parallelizes the computation minimizing the time for delivering rotational activity detection.

The ventricle cancellation method requires to buffer signals long enough to capture several ventricle beats, we buffer the last B seconds of the signals to estimate each channel ventricular pattern, e.g., $B = 10$ seconds. Computations take less than 7 seconds for $B = 10$ seconds, and a screen inside the operating room presents the results immediately.

APPENDIX A. REAL-TIME ROTATIONAL ACTIVITY DETECTION SYSTEM SPECIFICATIONS AND IMPLEMENTATION

B

Cardiac Modelling

B.1 FitzHugh-Nagumo Model

We introduce the modified FitzHugh-Nagumo (FH-N) equations implemented to generate the synthetic data to test the causality indices and the performance of the different algorithms in Chapter 4. In our simulations, we construct a 2D grid composed of $J \times J$ nodes ($J = 32$), where each node corresponds to a dynamical system following the classic FH-N equations, discretized using Euler's method with an integration time step $T_d = 5 \times 10^{-3}$ s, plus an additive stochastic noise term, and a coupling term gathering the interaction with neighbor nodes. Altogether,

this yields the following system of difference equations:

$$U_{i,j}[n+1] = U_{i,j}[n] + \sigma^2\sqrt{T_d}B_{i,j}[n+1] + T_d\Bigg(p_3(U_{i,j}[n]) - V_{i,j}[n] + \frac{1}{D}\sum_{(\ell,r)\in\mathcal{N}_{i,j}} U_{\ell,r}[n] + m_{i,j}G[n+1]\Bigg), \tag{B.1a}$$

$$V_{i,j}[n+1] = V_{i,j}[n] + T_d\left(\beta_0 U_{i,j}[n] + \beta_1 V_{i,j}[n] + \beta_2\right), \tag{B.1b}$$

where

- $n = 0, 1, 2, ...$ are the discrete-time instants, corresponding to continuous-time instants $t = nT_d$;
- $\{U_{i,j}[n]\}_{n=0,1,...}$ is the signal sequence (representing the AP of a cell) at the (i,j)-th node for $1 \leq i, j \leq J$;
- $p_3(u) = \sum_{r=0}^{3} \alpha_r u^r$ is a polynomial of order 3 with known fixed coefficients α_r for $r \in \{0, 1, 2, 3\}$;
- $\{V_{i,j}[n]\}_{n=0,1,...}$ is the recovery sequence at the same node, which depends on the known parameters β_r for $r \in \{0, 1, 2\}$;
- the set $\mathcal{N}_{i,j} \subset \{1, ..., J\} \times \{1, ..., J\}$ contains the neighbors, within the grid, of the (i,j)-th node;
- the coupling coefficient, $D > 0$, is known and fixed;
- $G[n]$ is a known, non-negative and typically periodic forcing signal;
- the $\{m_{i,j}\}_{1\leq i,j\leq J} \in \{0, 1\}$ are (known and fixed) binary indicators that determine which nodes are excited by the forcing signal $F[n]$;
- and the $\{B_{i,j}[n]\}_{n=0,1,...}$ are i.i.d. Gaussian random variables with zero mean and unit variance.

The parameters used for the simulations were set empirically in order to reproduce waveform propagation patterns observed in real signals (see [32] for further details): $\alpha_0 = \alpha_2 = 0$, $\alpha_1 = -\frac{18}{5}$, $\alpha_3 = 1$, $\frac{1}{D} = 4.5 \times 10^{-3}$, $\beta_0 = 2.1$, $\beta_1 = -0.6$, $\beta_2 = 0.6$, and $\sigma^2 = \frac{1}{2}$. Regarding $F[n]$, it consists of a periodic sequence of pulses.

References

[1] Recommendations for measurement standards in quantitative electrocardiography. The CSE Working Party. *Eur. Heart J.*, 6(10):815–25, oct 1985.

[2] Henry D I Abarbanel, Reggie Brown, John J. Sidorowich, and Lev Sh. Tsimring. The analysis of observed chaotic data in physical systems. *Rev. Mod. Phys.*, 65(4):1331–1392, 1993.

[3] Alejandro Alcaine, Michela Mase, Alessandro Cristoforetti, Flavia Ravelli, Giandomenico Nollo, Pablo Laguna, Juan Pablo Martinez, and Luca Faes. A Multi-Variate Predictability Framework to Assess Invasive Cardiac Activity and Interactions During Atrial Fibrillation. *IEEE Trans. Biomed. Eng.*, 64(5):1157–1168, may 2017.

[4] M. Allessie and N. de Groot. Rotors during AF: drivers or bystanders? *Eur. Heart J.*, 35(2):63–65, jan 2014.

[5] M A Allessie, F I Bonke, and F J Schopman. Circus movement in rabbit atrial muscle as a mechanism of tachycardia. III. The "leading circle" concept: a new model of circus movement in cardiac tissue without the involvement of an anatomical obstacle. *Circ. Res.*, 41(1):9–18, jul 1977.

[6] M A Allessie, K Konings, C J Kirchhof, and M Wijffels. Electrophysiologic mechanisms of perpetuation of atrial fibrillation. *Am. J. Cardiol.*, 77(3):10A–23A, jan 1996.

[7] MA Allessie, WJEP Lammers, FIM Bonke, and J Hollen. Experimental Evaluation of Moe's Wavelet Hypothesis of Atrial Fibrillation. In DP Zipes and J Jalife, editors, *Card. Electrophysiol. Arrhythm.*, pages 265–275. Grune & Stratton, Orlando, 1985.

[8] Maurits Allessie and Natasja de Groot. CrossTalk opposing view: Rotors have not been demonstrated to be the drivers of atrial fibrillation. *J. Physiol.*, 592(15):3167–3170, aug 2014.

[9] Maurits A Allessie, Natasja M S de Groot, Richard P M Houben, Ulrich Schotten, Eric Boersma, Joep L Smeets, and Harry J Crijns. Electropathological Substrate of Long-Standing Persistent Atrial Fibrillation in Patients With Structural Heart Disease Longitudinal Dissociation. *Circ. Arrhythmia Electrophysiol.*, 3(6):606–615, 2010.

[10] G. Arce and R. Stevenson. On the synthesis of median filter systems. *IEEE Trans. Circuits Syst.*, 34(4):420–429, apr 1987.

[11] F. Atienza, J. Almendral, J. Moreno, R. Vaidyanathan, A. Talkachou, J. Kalifa, A. Arenal, J. P. Villacastin, E. G. Torrecilla, A. Sanchez, R. Ploutz-Snyder, J. Jalife, and O. Berenfeld. Activation of Inward Rectifier Potassium Channels Accelerates Atrial Fibrillation in Humans: Evidence for a Reentrant Mechanism. *Circulation*, 114(23):2434–2442, dec 2006.

[12] Felipe Atienza, Jesús Almendral, José Jalife, Sharon Zlochiver, Robert Ploutz-Snyder, Esteban G Torrecilla, Angel Arenal, Jérôme Kalifa, Francisco Fernández-Avilés, and Omer Berenfeld. Real-time Dominant Frequency Mapping and Ablation of Dominant Frequency Sites in Atrial Fibrillation with Left-to-Right Frequency Gradients Predicts Long-Term Maintenance of Sinus Rhythm. *Hear. Rhythm*, 6(1):33–40, 2009.

[13] Felipe Atienza, Jesús Almendral, José Miguel Ormaetxe, Ángel Moya, Jesús Daniel Martínez-Alday, Antonio Hernández-Madrid, Eduardo Castellanos, Fernando Arribas, Miguel Ángel Arias, Luis Tercedor, Rafael Peinado,

Maria Fe Arcocha, Mercedes Ortiz, Nieves Martínez-Alzamora, Ángel Arenal, Francisco Fernández-Avilés, and José Jalife. Comparison of Radiofrequency Catheter Ablation of Drivers and Circumferential Pulmonary Vein Isolation in Atrial Fibrillation: A Noninferiority Randomized Multicenter RADAR-AF Trial. *J. Am. Coll. Cardiol.*, 64(23):2455–2467, 2014.

[14] Ali Baher, Zhilin Qu, Ashkan Hayatdavoudi, Scott T. Lamp, Ming-Jim Yang, Fagen Xie, Stephen Turner, Alan Garfinkel, and James N. Weiss. Short-term cardiac memory and mother rotor fibrillation. *Am. J. Physiol. - Hear. Circ. Physiol.*, 292(1), 2007.

[15] K. Balasundaram, K. Umapathy, J. Jeyaratnam, A. Niri, S. Masse, T. Farid, K. Nair, J. Asta, R. J. Cusimano, E. Vigmond, and K. Nanthakumar. Tracking Rotors With Minimal Electrodes: Modulation Index-Based Strategy. *Circ. Arrhythmia Electrophysiol.*, 8(2):447–455, 2015.

[16] V Barbaro, R Bartolini, R Bernarducci, G Calcagnini, F Martelli, and S Morelli. An Algorithm for the Detection and Classification of Atrial Fibrillation from Intra-Atrial Electrograms. *Proc. VIII Mediterr. Med. Biol. Eng. Comput. (MEDICON '98)*, 1998.

[17] Peyman Benharash, Eric Buch, Paul Frank, Michael Share, Roderick Tung, Kalyanam Shivkumar, and Ravi Mandapati. Quantitative Analysis of Localized Sources Identified by Focal Impulse and Rotor Modulation Mapping in Atrial Fibrillation. *Circ. Arrhythmia Electrophysiol.*, 8(3):554–561, 2015.

[18] Omer Berenfeld, Marcel Wellner, José Jalife, and Arkady M. Pertsov. Shaping of a scroll wave filament by cardiac fibers. *Phys. Rev. E*, 63(6):061901, may 2001.

[19] M Biermann, M Shenasa, M Borggrefe, G Hindricks, W Haverkamp, and G Breithardt. The interpretation of cardiac electrograms. In M Shenasa, M Borggrefe, and G Breithardt, editors, *Card. Mapp.*, chapter The interp,

pages 11–34. Wiley-Blackwell Publishing, New Jersey, USA, 2nd editio edition, 2003.

[20] Manuel Blanco-Velasco, Binwei Weng, and Kenneth E. Barner. ECG signal denoising and baseline wander correction based on the empirical mode decomposition. *Comput. Biol. Med.*, 38(1):1–13, 2008.

[21] Mark Anthony Bray, Shien Fong Lin, Rubin R. Aliev, Bradley J. Roth, and John P. Wikswo. Experimental and theoretical analysis of phase singularity dynamics in cardiac tissue. *J. Cardiovasc. Electrophysiol.*, 12(6):716–722, 2001.

[22] Mark Anthony Bray and John P. Wikswo. Considerations in phase plane analysis for nonstationary reentrant cardiac behavior. *Phys. Rev. E - Stat. Nonlinear, Soft Matter Phys.*, 65(5):1–8, 2002.

[23] Mark Anthony Bray and John P. Wikswo. Use of topological charge to determine filament location and dynamics in a numerical model of scroll wave activity. *IEEE Trans. Biomed. Eng.*, 49(10):1086–1093, 2002.

[24] Steven L. Bressler and Anil K. Seth. Wiener–Granger Causality: A well established methodology. *Neuroimage*, 58(2):323–329, sep 2011.

[25] Eric Buch, Michael Share, Roderick Tung, Peyman Benharash, Parikshit Sharma, Jayanthi Koneru, Ravi Mandapati, Kenneth A Ellenbogen, and Kalyanam Shivkumar. Long-Term Clinical Outcomes of Focal Impulse and Rotor Modulation for Treatment of Atrial Fibrillation: A Multicenter Experience. *Hear. Rhythm*, 13(3):636–41, 2016.

[26] David Calvo, José Rubín, Diego Pérez, and César Morís. Ablation of Rotor Domains Effectively Modulates Dynamics of Human: Long-Standing Persistent Atrial Fibrillation. *Circ. Arrhythm. Electrophysiol.*, 10(12):e005740, dec 2017.

[27] C D Cantwell, C H Roney, F S Ng, J H Siggers, S J Sherwin, and N S Peters. Techniques for automated local activation time annotation and conduction velocity estimation in cardiac mapping. *Comput. Biol. Med.*, 65:229–42, oct 2015.

[28] Evaristo Castellanos, Pablo M Ruiz Hernandez, Gonzalo Ríos-Muñoz, Pablo Ávila, Tomás Datino, Felipe Atienza, Francisco Fernández-Avilés, and Ángel Arenal. Influencia del Ritmo en la Identificación de Islotes de Escara Auricular en Pacientes con FA Persistente sin Disfunción Ventricular Izquierda Detectada con Catéter de Mapeo Multielectrodo de 1mm. In *SEC 2016 - El Congr. las Enfermedades Cardiovasc.*, number 6002-38, 2016.

[29] T.-F. Chao, H.-M. Tsao, Y.-J. Lin, C.-F. Tsai, W.-S. Lin, S.-L. Chang, L.-W. Lo, Y.-F. Hu, T.-C. Tuan, K. Suenari, C.-H. Li, B. Hartono, H.-Y. Chang, K. Ambrose, T.-J. Wu, and S.-A. Chen. Clinical Outcome of Catheter Ablation in Patients With Nonparoxysmal Atrial Fibrillation: Results of 3-Year Follow-Up. *Circ. Arrhythmia Electrophysiol.*, 5(3):514–520, jun 2012.

[30] S A Chen, M H Hsieh, C T Tai, C F Tsai, V S Prakash, W C Yu, T L Hsu, Y A Ding, and M S Chang. Initiation of atrial fibrillation by ectopic beats originating from the pulmonary veins: electrophysiological characteristics, pharmacological responses, and effects of radiofrequency ablation. *Circulation*, 100(18):1879–86, nov 1999.

[31] Charles K. Chui. *An Introduction to Wavelets*. Academic Press Professional, Inc., San Diego, CA, USA, 1992.

[32] D Crisan, J Miguez, and G Rios. A simple scheme for the parallelization of particle filters and its application to the tracking of complex stochastic systems. *ArXiv e-prints*, 2014.

[33] Dan Crisan, Joaquín Míguez, and Gonzalo Ríos-Muñoz. On the performance of parallelisation schemes for particle filtering. *EURASIP J. Adv. Signal Process.*, 2018(1):31, dec 2018.

[34] Min Dai and Shi Liu Lian. Removal of baseline wander from dynamic electrocardiogram signals. *Proc. 2009 2nd Int. Congr. Image Signal Process. CISP'09*, pages 1–4, 2009.

[35] Emile G. Daoud, Ziad Zeidan, John D. Hummel, Raul Weiss, Mahmoud Houmsse, Ralph Augostini, and Steven J. Kalbfleisch. Identification of Repetitive Activation Patterns Using Novel Computational Analysis of Multielectrode Recordings During Atrial Fibrillation and Flutter in Humans. *JACC Clin. Electrophysiol.*, 3(3):207–216, mar 2017.

[36] P. de Chazal, C. Heneghan, E. Sheridan, R. Reilly, P. Nolan, and M. O'Malley. Automated Processing of the Single-Lead Electrocardiogram for the Detection of Obstructive Sleep Apnoea. *IEEE Trans. Biomed. Eng.*, 50(6):686–696, 2003.

[37] N. M. S. de Groot, R. P. M. Houben, J. L. Smeets, E. Boersma, U. Schotten, M. J. Schalij, H. Crijns, and M. A. Allessie. Electropathological Substrate of Longstanding Persistent Atrial Fibrillation in Patients With Structural Heart Disease: Epicardial Breakthrough. *Circulation*, 122(17):1674–1682, oct 2010.

[38] Jens Eckstein, Michael Kühne, Stefan Osswald, and Ulrich Schotten. Mapping of atrial fibrillation–basic research and clinical applications. *Swiss Med. Wkly. Off. J. Swiss Soc. Infect. Dis. Swiss Soc. Intern. Med. Swiss Soc. Pneumol.*, 139(35-36):496–504, 2009.

[39] Milad El Haddad, Richard Houben, Roland Stroobandt, Frederic Van Heuverswyn, Rene Tavernier, and Mattias Duytschaever. Algorithmic detection of the beginning and end of bipolar electrograms: Implications for novel methods to assess local activation time during atrial tachycardia. *Biomed. Signal Process. Control*, 8(6):981–991, 2013.

[40] Víctor Elvira, Luca Martino, David Luengo, and Mónica F Bugallo. Improv-

ing population Monte Carlo: Alternative weighting and resampling schemes. *Signal Processing*, 131:77–91, 2017.

[41] L. Faes and G. Nollo. Assessing Frequency Domain Causality in Cardiovascular Time Series with Instantaneous Interactions. *Methods Inf. Med.*, 49(5):453–457, sep 2010.

[42] L Faes, A Porta, and G Nollo. Testing Frequency-Domain Causality in Multivariate Time Series. *IEEE Trans. Biomed. Eng.*, 57(8):1897–1906, aug 2010.

[43] K Fleet and Y Weiss. Optical Flow Estimation. In Nikos Paragios, Yunmei Chen, and Olivier Faugeras, editors, *Handb. Math. Model. Comput. Vis.*, chapter 15, pages 237–257. Springer US, Boston, MA, 2006.

[44] John F Geweke. Measures of Conditional Linear Dependence and Feedback between Time Series. *J. Am. Stat. Assoc.*, 79(388):907–915, 1984.

[45] Jean D Gibbons and John W Pratt. P-values: Interpretation and Methodology. *Am. Stat.*, 29(1):20–25, 1975.

[46] A Goryachev and R Kapral. Spiral waves in chaotic systems. *Phys. Rev. Lett.*, 76(10):1619–1622, 1996.

[47] Andrew Grace, Atul Verma, and Stephan Willems. Dipole Density Mapping of Atrial Fibrillation. *Eur. Heart J.*, 38(1):5–9, jan 2017.

[48] C W J Granger. Investigating Causal Relations by Econometric Models and Cross-spectral Methods. *Econometrica*, 37(3):424–438, 1969.

[49] R a Gray, a M Pertsov, and J Jalife. Spatial and temporal organization during cardiac fibrillation. *Nature*, 392(6671):75–78, 1998.

[50] Michel Haïssaguerre, Pierre Jaïs, Dipen C. Shah, Atsushi Takahashi, Mélèze Hocini, Gilles Quiniou, Stéphane Garrigue, Alain Le Mouroux, Philippe Le Métayer, and Jacques Clémenty. Spontaneous Initiation of Atrial Fibrillation

by Ectopic Beats Originating in the Pulmonary Veins. *N. Engl. J. Med.*, 339(10):659–666, 1998.

[51] Taigang He, Gari Clifford, and Lionel Tarassenko. Application of independent component analysis in removing artefacts from the electrocardiogram. *Neural Comput. Appl.*, 15(2):105–116, 2006.

[52] Elvio A. Heidenreich, José M. Ferrero, Manuel Doblaré, and José F. Rodríguez. Adaptive Macro Finite Elements for the Numerical Solution of Monodomain Equations in Cardiac Electrophysiology. *Ann. Biomed. Eng.*, 38(7):2331–2345, jul 2010.

[53] Berthold K P Horn and Brian G. Schunck. Determining Optical Flow. *Artif. Intell.*, 17(1-3):185–203, 1981.

[54] R E Ideker, W M Smith, S M Blanchard, S L Reiser, E V Simpson, P D Wolf, and N D Danieley. The Assumptions of Isochronal Cardiac Mapping. *Pacing Clin. Electrophysiol.*, 12(3):456–478, 1989.

[55] J Jalife, O Berenfeld, A Skanes, and R Mandapati. Mechanisms of atrial fibrillation: mother rotors or multiple daughter wavelets, or both? *J. Cardiovasc. Electrophysiol.*, 9(8 Suppl):S2–12, aug 1998.

[56] José Jalife and Omer Berenfeld. Molecular mechanisms and global dynamics of fibrillation: an integrative approach to the underlying basis of vortex-like reentry. *J. Theor. Biol.*, 230(4):475–487, oct 2004.

[57] José Jalife, Omer Berenfeld, and Moussa Mansour. Mother Rotors and Fibrillatory Conduction: A Mechanism of Atrial Fibrillation. *Cardiovasc. Res.*, 54(2):204–216, 2002.

[58] J. W. E. Jarman, T. Wong, P. Kojodjojo, H. Spohr, J. E. Davies, M. Roughton, D. P. Francis, P. Kanagaratnam, V. Markides, D. W. Davies, and N. S. Peters. Spatiotemporal Behavior of High Dominant Frequency

During Paroxysmal and Persistent Atrial Fibrillation in the Human Left Atrium. *Circ. Arrhythmia Electrophysiol.*, 5(4):650–658, aug 2012.

[59] Julian W. E. Jarman, Tom Wong, Pipin Kojodjojo, Hilmar Spohr, Justin E.R. Davies, Michael Roughton, Darrel P. Francis, Prapa Kanagaratnam, Mark D. O'neill, Vias Markides, D. Wyn Davies, and Nicholas S. Peters. Organizational Index Mapping to Identify Focal Sources During Persistent Atrial Fibrillation. *J. Cardiovasc. Electrophysiol.*, 25(4):355–363, apr 2014.

[60] S. Kadambe, R. Murray, and G.F. Boudreaux-Bartels. Wavelet transform-based QRS complex detector. *IEEE Trans. Biomed. Eng.*, 46(7):838–848, jul 1999.

[61] J Keener and J Sneyd, editors. *Mathematical physiology I: cellular physiology*. Springer, New York, NY, 2009.

[62] J Keener and J Sneyd, editors. *Mathematical Physiology II: Systems Physiology*. Springer-Verlag New York, 2009.

[63] Paulus Kirchhof, Stefano Benussi, Dipak Kotecha, Anders Ahlsson, Dan Atar, Barbara Casadei, Manuel Castella, Hans-Christoph Diener, Hein Heidbuchel, Jeroen Hendriks, Gerhard Hindricks, Antonis S Manolis, Jonas Oldgren, Bogdan Alexandru Popescu, Ulrich Schotten, Bart Van Putte, Panagiotis Vardas, Stefan Agewall, John Camm, Gonzalo Baron Esquivias, Werner Budts, Scipione Carerj, Filip Casselman, Antonio Coca, Raffaele De Caterina, Spiridon Deftereos, Dobromir Dobrev, José M Ferro, Gerasimos Filippatos, Donna Fitzsimons, Bulent Gorenek, Maxine Guenoun, Stefan H Hohnloser, Philippe Kolh, Gregory Y H Lip, Athanasios Manolis, John McMurray, Piotr Ponikowski, Raphael Rosenhek, Frank Ruschitzka, Irina Savelieva, Sanjay Sharma, Piotr Suwalski, Juan Luis Tamargo, Clare J Taylor, Isabelle C Van Gelder, Adriaan A Voors, Stephan Windecker, Jose Luis Zamorano, and Katja Zeppenfeld. 2016 ESC Guidelines for the manage-

ment of atrial fibrillation developed in collaboration with EACTS. *Europace*, 18(11):1609–1678, 2016.

[64] Samantha Kleinberg and George Hripcsak. A review of causal inference for biomedical informatics. *J. Biomed. Inform.*, 44(6):1102–1112, dec 2011.

[65] Pawel Kuklik, Stef Zeemering, Bart Maesen, Jos Maessen, Harry J. Crijns, Sander Verheule, Anand N. Ganesan, and Ulrich Schotten. Reconstruction of Instantaneous Phase of Unipolar Atrial Contact Electrogram Using a Concept of Sinusoidal Recomposition and Hilbert Transform. *IEEE Trans. Biomed. Eng.*, 62(1):296–302, jan 2015.

[66] Pawel Kuklik, Stef Zeemering, Arne van Hunnik, Bart Maesen, Laurent Pison, Dennis Lau, Jos Maessen, Piotr Podziemski, Christian Meyer, Benjamin Schaffer, Harry Crijns, Stephan Willems, and Ulrich Schotten. Identification of Rotors during Human Atrial Fibrillation using Contact Mapping and Phase Singularity Detection: Technical Considerations. *IEEE Trans. Biomed. Eng.*, PP(99):1, 2016.

[67] Jacob Laughner, Shibaji Shome, Nicholas Child, Allan Shuros, Petr Neuzil, Jaswinder Gill, and Matthew Wright. Practical Considerations of Mapping Persistent Atrial Fibrillation With Whole-Chamber Basket Catheters. *JACC Clin. Electrophysiol.*, 2(1):55–65, 2016.

[68] Geoffrey Lee, Saurabh Kumar, Andrew Teh, Andrew Madry, Steven Spence, Marco Larobina, John Goldblatt, Robin Brown, Victoria Atkinson, Simon Moten, Joseph B. Morton, Prashanthan Sanders, Peter M. Kistler, and Jonathan M. Kalman. Epicardial Wave Mapping in Human Long-Lasting Persistent Atrial Fibrillation: Transient Rotational Circuits, Complex Wavefronts, and Disorganized Activity. *Eur. Heart J.*, 35(2):86–97, 2014.

[69] T Lewis. Report CXIX. Auricular Fibrillation: A Common Clinical Condition. *Br. Med. J.*, 2(2552):1528, nov 1909.

[70] Hsin-Yi Lin, Sz-Ying Sz-Ying Liang, Yi-Lwun Ho, Yen-Hung Lin, and Hsi-Pin Ma. Discrete-wavelet-transform-based noise reduction and R wave detection for ECG signals. In *2013 IEEE 15th Int. Conf. e-Health Networking, Appl. Serv. (Healthcom 2013)*, pages 355–360. IEEE, oct 2013.

[71] W.-S. Lin, Ching-Tai Tai, Ming-Hsiung Hsieh, Chin-Feng Tsai, Yung-Kuo Lin, Hsuan-Ming Tsao, Jin-Long Huang, Wen-Chung Yu, Shih-Ping Yang, Yu-An Ding, Mau-Song Chang, and Shih-Ann Chen. Catheter Ablation of Paroxysmal Atrial Fibrillation Initiated by Non-Pulmonary Vein Ectopy. *Circulation*, 107(25):3176–3183, jul 2003.

[72] B Lown, R Amarasingham, and J Neuman. New method for terminating cardiac arrhythmias. Use of synchronized capacitor discharge. *JAMA*, 182:548–55, nov 1962.

[73] David Luengo, Gonzalo Ríos-Muñoz, and Victor Elvira. Causality analysis of atrial fibrillation electrograms. In *2015 Comput. Cardiol. Conf.*, pages 585–588. IEEE, sep 2015.

[74] David Luengo, Gonzalo Rios-Munoz, Victor Elvira, and Antonio Artes-Rodriguez. A hierarchical algorithm for causality discovery among atrial fibrillation electrograms. In *2016 IEEE Int. Conf. Acoust. Speech Signal Process.*, pages 774–778. IEEE, mar 2016.

[75] David Luengo, Gonzalo Ricardo Rios Munoz, Victor Elvira, Carlos Sanchez, and Antonio Artes-Rodriguez. Hierarchical Algorithms for Causality Retrieval in Atrial Fibrillation Intracavitary Electrograms. *IEEE J. Biomed. Heal. Informatics*, pages 1–1, 2018.

[76] David Luengo, Ignacio Santamaría, and Luis Vielva. A general solution to blind inverse problems for sparse input signals. *Neurocomputing*, 69(1):198–215, 2005.

[77] M. M. Maleckar, J. L. Greenstein, W. R. Giles, and N. A. Trayanova. K+ current changes account for the rate dependence of the action potential in

the human atrial myocyte. *AJP Hear. Circ. Physiol.*, 297(4):H1398–H1410, oct 2009.

[78] Claire Martin, Shohreh Honarbakhsh, Ailsa McLean, Pier Lambiase, and Richard Schilling. 33 Use of novel global ultrasound imaging and continuous dipole density mapping to guide ablation in macro-reentrant tachycardias. *Heart*, 103(Suppl 5):A26 LP – A27, jun 2017.

[79] Michael E. J. Masson. A tutorial on a practical Bayesian alternative to null-hypothesis significance testing. *Behav. Res. Methods*, 43(3):679–690, sep 2011.

[80] Wallace A. McAlpine. *Heart and Coronary Arteries*. Springer Berlin Heidelberg, 1975.

[81] N. D. Mermin. The topological theory of defects in ordered media. *Rev. Mod. Phys.*, 51(3):591–648, jul 1979.

[82] George Ralph Mines. On dynamic equilibrium in the heart. *J. Physiol.*, 46(4-5):349–383, jul 1913.

[83] G K Moe and J A Abildskov. Atrial fibrillation as a self-sustaining arrhythmia independent of focal discharge. *Am. Heart J.*, 58(1):59–70, jul 1959.

[84] Gordon K Moe, Werner C Rheinboldt, and J.A Abildskov. A computer model of atrial fibrillation. *Am. Heart J.*, 67(2):200–220, feb 1964.

[85] Sanjiv M. Narayan, Tina Baykaner, Paul Clopton, Amir Schricker, Gautam G. Lalani, David E. Krummen, Kalyanam Shivkumar, and John M. Miller. Ablation of Rotor and Focal Sources Reduces Late Recurrence of Atrial Fibrillation Compared With Trigger Ablation Alone. *J. Am. Coll. Cardiol.*, 63(17):1761–1768, may 2014.

[86] Sanjiv M. Narayan and José Jalife. CrossTalk proposal: Rotors have been demonstrated to drive human atrial fibrillation. *J. Physiol.*, 592(15):3163–3166, aug 2014.

[87] Sanjiv M Narayan, Dhruv Kazi, David E Krummen, and Wouter-Jan Rappel. Repolarization and activation restitution near human pulmonary veins and atrial fibrillation initiation: a mechanism for the initiation of atrial fibrillation by premature beats. *J. Am. Coll. Cardiol.*, 52(15):1222–30, oct 2008.

[88] Sanjiv M. Narayan, David E. Krummen, Michael W. Enyeart, and Wouter Jan Rappel. Computational Mapping Identifies Localized Mechanisms for Ablation of Atrial Fibrillation. *PLoS One*, 7(9):1–8, 2012.

[89] S Nattel. Experimental evidence for proarrhythmic mechanisms of antiarrhythmic drugs. *Cardiovasc. Res.*, 37(3):567–577, mar 1998.

[90] Stanley Nattel. New ideas about atrial fibrillation 50 years on. *Nature*, 415(6868):219–226, jan 2002.

[91] KENNETH N. OGLE. The Perception of the Visual World. James J. Gibson; Leonard Carmichael, Ed. Boston: Houghton Mifflin, 1950. 235 pp. $4.00. *Science (80-.).*, 113(2940), 1951.

[92] S. V. Pandit and J. Jalife. Rotors and the Dynamics of Cardiac Fibrillation. *Circ. Res.*, 112(5):849–862, 2013.

[93] C Pantaleon, D Luengo, and I Santamaria. Piecewise-linear maps. *IEEE Signal Process. Lett.*, 7(8):235–237, 2000.

[94] Ali Pashaei, Jason Bayer, Valentin Meillet, Rémi Dubois, and Edward Vigmond. Computation and Projection of Spiral Wave Trajectories During Atrial Fibrillation. *Card. Electrophysiol. Clin.*, 7(1):37–47, 2015.

[95] A. Porta, T. Bassani, V. Bari, and S. Guzzetti. Granger causality in cardiovascular variability series: Comparison between model-based and model-free approaches. In *2012 Annu. Int. Conf. IEEE Eng. Med. Biol. Soc.*, volume 2012, pages 3684–3687. IEEE, aug 2012.

[96] Rui Providência, Pier D. Lambiase, Neil Srinivasan, Girish Ganesh Babu, Konstantinos Bronis, Syed Ahsan, Fakhar Z. Khan, Anthony W. Chow, Edward Rowland, Martin Lowe, and Oliver R. Segal. Is There Still a Role for Complex Fractionated Atrial Electrogram Ablation in Addition to Pulmonary Vein Isolation in Patients With Paroxysmal and Persistent Atrial Fibrillation? *Circ. Arrhythmia Electrophysiol.*, 8(5):1017–1029, oct 2015.

[97] U. Richter, L. Faes, F. Ravelli, and L. Sornmo. Propagation Pattern Analysis During Atrial Fibrillation Based on Sparse Modeling. *IEEE Trans. Biomed. Eng.*, 59(5):1319–1328, may 2012.

[98] Ulrike Richter, Luca Faes, Alessandro Cristoforetti, Michela Masè, Flavia Ravelli, Martin Stridh, and Leif Sörnmo. A novel approach to propagation pattern analysis in intracardiac atrial fibrillation signals. *Ann. Biomed. Eng.*, 39(1):310–23, jan 2011.

[99] G Ríos-Muñoz, A Artés-Rodríguez, A Arenal, and C Sánchez. Left Atrium Patient-Specific Modelling from Electroanatomical Maps. In *Virtual Physiol. Hum. Silico Med.*, pages 1–4, Zaragoza, sep 2018.

[100] G R Ríos-Muñoz, A Artés-Rodríguez, and J Míguez. Particle Filter Tracking of Complex Stochastic Systems Applied to In Silico Wavefront Propagation. In *2018 Comput. Cardiol.*, pages 1–4, Maastricht, sep 2018.

[101] G R Ríos-Muñoz, S Rocher, A Artés-Rodríguez, A Arenal, J Saiz, and C Sánchez. Patient Tailored In Silico 3D Simulations and Models from Electroanatomical Maps of the Left Atrium. In *2018 Comput. Cardiol.*, pages 1–4, Maastricht, sep 2018.

[102] Gonzalo R. Ríos-Muñoz, Ángel Arenal, and Antonio Artés-Rodríguez. Real-Time Rotational Activity Detection in Atrial Fibrillation. *Front. Physiol.*, 9:208, mar 2018.

[103] Gonzalo R. Ríos-Muñoz, Antonio Artés-Rodríguez, Ángel Arenal, and Fran-

cisco Fernández-Avilés. Sistema y Método Para la Detección Automática de Patrones Electrofisiológicos Anómalos, 2017.

[104] Gonzalo R. Ríos-Muñoz, Pablo M Ruiz Hernandez, Evaristo Castellanos, Pablo Ávila, Gerard Loughlin, Francisco Fernández-Avilés, Antonio Artés-Rodríguez, and Ángel Arenal. Presence, Complexity and Voltage Characterization of Rotational Activity in Persistent Atrial Fibrillation Patients. In *Atr. Signals*, Valencia, 2017.

[105] Gonzalo R. Ríos-Muñoz, Pablo M Ruiz Hernandez, Evaristo Castellanos, Pablo Ávila, Gerard Loughlin, Francisco Fernández-Avilés, Antonio Artés-Rodríguez, and Ángel Arenal. Substrate Characterization of Rotational Activity Sites in Persistent Atrial Fibrillation Patients. In *CNIC Atr. Fibrillation Symp. From Mech. to Popul. Sci.*, Madrid, 2017.

[106] M Rodrigo, A Liberos, M S Guillem, J Millet, and A M Climent. Causality relation map: A novel methodology for the identification of hierarchical fibrillatory processes. In *2011 Comput. Cardiol.*, pages 173–176, sep 2011.

[107] Miguel Rodrigo, Andreu M. Climent, Alejandro Liberos, David Calvo, Francisco Fernández-Avilés, Omer Berenfeld, Felipe Atienza, and Maria S. Guillem. Identification of Dominant Excitation Patterns and Sources of Atrial Fibrillation by Causality Analysis. *Ann. Biomed. Eng.*, 44(8):2364–2376, feb 2016.

[108] Miguel Rodrigo, Andreu M. Climent, Alejandro Liberos, Francisco Fernández-Avilés, Omer Berenfeld, Felipe Atienza, and Maria S. Guillem. Technical Considerations on Phase Mapping for Identification of Atrial Reentrant Activity in Direct- and Inverse-Computed Electrograms. *Circ. Arrhythmia Electrophysiol.*, 10(9):e005008, sep 2017.

[109] Miguel Rodrigo, Maria S Guillem, Alejandro Liberos, José Millet, Omer Berenfeld, and Andreu M Climent. Identification of Fibrillatory Sources

by Measuring Causal Relationships. *Comput. Cardiol. (2010).*, 39:705–708, 2012.

[110] C H Roney, C D Cantwell, J H Siggers, F S Ng, and N S Peters. A novel method for rotor tracking using bipolar electrogram phase. In *Comput. Cardiol. 2014*, pages 233–236, sep 2014.

[111] Caroline H. Roney, Chris D. Cantwell, Jason D. Bayer, Norman A. Qureshi, Phang Boon Lim, Jennifer H. Tweedy, Prapa Kanagaratnam, Nicholas S. Peters, Edward J. Vigmond, and Fu Siong Ng. Spatial Resolution Requirements for Accurate Identification of Drivers of Atrial Fibrillation. *Circ. Arrhythmia Electrophysiol.*, 10(5):e004899, may 2017.

[112] K M Ropella, A V Sahakian, J M Baerman, and S Swiryn. Effects of Procainamide on Intra-Atrial Electrograms During Atrial Fibrillation: Implications for Detection Algorithms. *Circulation*, 77(5):1047–1054, 1988.

[113] Pablo M Ruiz Hernandez, Gonzalo Ríos-Muñoz, Evaristo Castellanos, Pablo Ávila, Esteban G Torrecilla, Gerard A Loughlin, Tomas Datino, Felipe Atienza, Francisco Fernandez-Aviles, Antonio Artés-Rodríguez, and Ángel Arenal. Presence and Distribution of Rotational Conduction Points and Its Association With Scar in Patients With Persistent Atrial Fibrillation. In *Hear. Rhythm*, volume 14, pages S235—–S236. Elsevier, 2017.

[114] Pablo M Ruiz Hernandez, Gonzalo R. Ríos-Muñoz, Evaristo Castellanos, Pablo Ávila, Felipe Atienza, Antonio Artés-Rodríguez, Francisco Fernández-Avilés, and Ángel Arenal. Caracterización del sustrato de los sitios de activación rotacional en Fibrilación Auricular Persistente: Análisis en función del ritmo. In *RITMO18*, Sevilla, 2018.

[115] Carlos Sánchez, Alfonso Bueno-Orovio, Esther Pueyo, and Blanca Rodríguez. Atrial Fibrillation Dynamics and Ionic Block Effects in Six Heterogeneous Human 3D Virtual Atria with Distinct Repolarization Dynamics. *Front. Bioeng. Biotechnol.*, 5:29, may 2017.

[116] D. Scherf, F.J. Romano, and R. Terranova. Experimental studies on auricular flutter and auricular fibrillation. *Am. Heart J.*, 36(2):241–251, aug 1948.

[117] Gunnar Seemann, Christine Höper, Frank B Sachse, Olaf Dössel, Arun V Holden, and Henggui Zhang. Heterogeneous three-dimensional anatomical and electrophysiological model of human atria. *Philos. Trans. R. Soc. London A Math. Phys. Eng. Sci.*, 364(1843), 2006.

[118] Anil K. Seth. A MATLAB toolbox for Granger causal connectivity analysis. *J. Neurosci. Methods*, 186(2):262–273, feb 2010.

[119] M Shenasa, G Hindricks, M Borggrefe, and G Breithardt, editors. *Cardiac Mapping*. USA: Wiley, New York, NY, 2009.

[120] D. Shepard. A Two-Dimensional Interpolation Function for Irregularly-Spaced Data. *Proc. 1968 ACM Natl. Conf.*, pages 517–524, 1968.

[121] Akiko Shiroshita-Takeshita, Bianca J. J. M. Brundel, and Stanley Nattel. Atrial Fibrillation: Basic Mechanisms, Remodeling and Triggers. *J. Interv. Card. Electrophysiol.*, 13(3):181–193, sep 2005.

[122] J Slocum, E Byrom, L McCarthy, A Sahakian, and S Swiryn. Computer Detection of Atrioventricular Dissociation From Surface Electrocardiograms During Wide QRS Complex Tachycardias. *Circulation*, 72:1028–1036, 1985.

[123] M S Spach, R C Barr, G A Serwer, J M Kootsey, and E A Johnson. Extracellular potentials related to intracellular action potentials in the dog Purkinje system. *Circ. Res.*, 30(5):505–19, may 1972.

[124] P Stoica and Y Selen. Model-order selection: a review of information criterion rules. *IEEE Signal Process. Mag.*, 21(4):36–47, 2004.

[125] Ernesto F. Treo, Daniel O. Cervantes, and Edward J. Ciaccio. Automated detection and mapping of electrical activation when electrogram morphology is complex. *Biomed. Signal Process. Control*, 8(1):41–49, 2013.

[126] C F Tsai, C T Tai, M H Hsieh, W S Lin, W C Yu, K C Ueng, Y A Ding, M S Chang, and S A Chen. Initiation of atrial fibrillation by ectopic beats originating from the superior vena cava: electrophysiological characteristics and results of radiofrequency ablation. *Circulation*, 102(1):67–74, jul 2000.

[127] K. Umapathy, K. Nair, S. Masse, S. Krishnan, J. Rogers, M. P. Nash, and K. Nanthakumar. Phase Mapping of Cardiac Fibrillation. *Circ. Arrhythmia Electrophysiol.*, 3(1):105–114, 2010.

[128] Laura Anna Unger, Markus Rottmann, Gunnar Seemann, and Olaf Dössel. Detecting phase singularities and rotor center trajectories based on the Hilbert transform of intraatrial electrograms in an atrial voxel model. *Curr. Dir. Biomed. Eng.*, 1(1):38–41, 2015.

[129] K L Venkatachalam, Joel E Herbrandson, and Samuel J Asirvatham. Signals and Signal Processing for the Electrophysiologist: Part I: Electrogram Acquisition. *Circ. Arrhythmia Electrophysiol.*, 4(6):965–73, 2011.

[130] Ramya Vijayakumar, Sunil K. Vasireddi, Phillip S. Cuculich, Mitchell N. Faddis, and Yoram Rudy. Methodology Considerations in Phase Mapping of Human Cardiac Arrhythmias. *Circ. Arrhythmia Electrophysiol.*, 9(11), 2016.

[131] Reza Wakili, Niels Voigt, Stefan Kääb, Dobromir Dobrev, and Stanley Nattel. Recent advances in the molecular pathophysiology of atrial fibrillation. *J. Clin. Invest.*, 121(8):2955–2968, aug 2011.

[132] Arthur T. Winfree. *When time breaks down : the three-dimensional dynamics of electrochemical waves and cardiac arrhythmias*. Princeton, N.J. Princeton University Press, 1987.

[133] H Winterberg. Studien über herzflimmern. I. Über die wirkung des N. vagus und accelerans auf das Flimmern des Herzens. *Pflügers Arch Physiol*, (117):223–256, 1907.

[134] Seigo Yamashita, Ashok J Shah, Saagar Mahida, Jean-Marc Sellal, Benjamin Berte, Darren Hooks, Antonio Frontera, Nora Al Jefairi, Jean-Yves Wielandts, Han S Lim, Sana Amraoui, Arnaud Denis, Nicolas Derval, Frédéric Sacher, Hubert Cochet, Mélèze Hocini, Pierre Jaïs, and Michel Haïssaguerre. Body Surface Mapping to Guide Atrial Fibrillation Ablation. *Arrhythmia Electrophysiol. Rev.*, 4(3):172–6, dec 2015.

[135] Arthur M. Yue, Michael R. Franz, Paul R. Roberts, and John M. Morgan. Global Endocardial Electrical Restitution in Human Right and Left Ventricles Determined by Noncontact Mapping. *J. Am. Coll. Cardiol.*, 46(6):1067–1075, sep 2005.

[136] Qinghua Zhang, Alfredo Illanes Manriquez, Claire Médigue, Yves Papelier, and Michel Sorine. An Algorithm for Robust and Efficient Location of T-wave Ends in Electrocardiograms. *IEEE Trans. Biomed. Eng.*, 53(12 Pt 1):2544–52, 2006.

[137] Ekaterina Zhuchkova and Richard Clayton. Methods for identifying and tracking phase singularities in computational models of re-entrant fibrillation. *Funct. Imaging Model. Hear.*, pages 246–255, 2005.